THERMAL CONTROL DESIGN FOR A SPACE-BORNE ON-CHIP OPTICAL PHASED ARRAY

NICHOLAS SEBASTIAN ZONTA

A THESIS SUBMITTED TO
THE FACULTY OF GRADUATE STUDIES
IN PARTIAL FULFILLMENT OF THE REQUIREMENTS
FOR THE DEGREE OF
MASTER OF SCIENCE

GRADUATE PROGRAMME IN EARTH AND SPACE SCIENCE
YORK UNIVERSITY
TORONTO, ONTARIO

JUNE 2022

© NICHOLAS SEBASTIAN ZONTA, 2022

ABSTRACT

The thermal control and model-based analysis is an integral part of developing an optical photonics device such as the proposed Optical Phased Array (OPA). This research is to model and implement the thermal control hardware and algorithm to keep the OPA at a stable temperature during operation. Detailed COMSOL models of the OPA and supporting hardware demonstrated that a constant setpoint results in consistent and proportional low levels of thermal crosstalk. A thermal feedback controller and supporting hardware was designed and tested to improve the overshoot and settling time. The system for the OPA includes both a solid state thermo-electric cooler (TEC), and the custom PCB interface between them. The controller was tuned experimentally and simulation analysis. The results indicate that a combination of the heuristic Zeigler-Nichols classic method and simulated input dependent experimental transfer function method yields the fastest settling times at 18.5 and 27.5 seconds.

ACKNOWLEDGEMENTS

This work would not have been possible without the unyielding support of everyone involved. It has been an honor to be a part of the Optical Photonics Array project and I want to thank all parties involved including Honeywell, the National Research Council of Canada, MITACS, the Canadian Space Agency, and the several collaborating university teams including Carleton, Western, and the University of Toronto. As for the team at York University, I want to give my utmost thanks to everyone who had supported me through this venture including my advisors, my fellow lab mates, my friends, and loved ones. To those closest who have been my biggest cheerleaders, including my supervisor Dr. Regina Lee, my lab partner on the project (soon to be Dr.) Akash Chauhan, and our project lead Dr. Hugh Podmore, thank you for your unwavering support and patience with me. These have been an incredibly trying few years, but despite the hardships we have all endured, I am at peace knowing that the OPA project continues with our support to revolutionize the industry. I have been blessed to work alongside such intelligent and accomplished peers and wish that our paths might cross once again. Thank you all.

TABLE OF CONTENTS

ABSTRACT ii

ACKNOWLEDGEMENTS iii

LIST OF TABLES vii

LIST OF FIGURES viii

Chapter 1 Introduction 1

1.1 Silicon Photonics in Space 2

1.2 Optical Photonics Array 3

1.3 Research Objectives 6

1.3.1 Thermal Model Analysis 6

1.3.2 Thermal Electric Cooler (TEC) Hardware Design and Integration 7

1.3.3 Control Design Characterization and Testing 7

1.4 Design Limitations / Boundaries 8

1.5 Thesis Contribution 9

1.6 Thesis Outline 10

Chapter 2 Background 11

2.1 Principles of Heat Transfer Theory 11

2.1.1 Conduction 12

2.1.2 Thermal Contact Conductance 13

2.1.3 Homogeneous Materials 13

2.1.4 Convection 15

2.1.5 Radiation 15

2.1.6 Boundary Conditions 16

2.1.7 Joule Heating 18

2.1.8 The Thermoelectric Effect 18

2.2 Principles of Control Theory ... 20
2.2.1 Actuator-Plant Model ... 20
2.2.2 The Steinhart-Hart Equation ... 22
2.2.3 PID Control Design ... 23
Chapter 3 Thermal Modelling of OPA ... 25
3.1 Phase Shifter Design ... 25
3.2 COMSOL Multiphysics – 3D OPA Model ... 28
3.3 COMSOL Multiphysics – 2D OPA Cross-Section ... 32
3.4 Simulation Results ... 34
3.4.1 Steady-state Analysis ... 35
3.4.2 Time Dependent Studies ... 38
3.4.3 Thermal Crosstalk Analysis ... 41
Chapter 4 Interface, Characterization, and Validation ... 44
4.1 PCB Design ... 44
4.2 Test Setup ... 49
4.2.1 Thermistor Setup ... 54
4.2.2 Thermo-electric Cooler Module ... 56
4.2.3 Heatsink Setup ... 58
4.3 Open-Loop Control Tests, Experimental Setup, and Results ... 59
Chapter 5 Closed-Loop Feedback Thermal Control ... 65
5.1 Closed-Loop Control Tests, Experimental Setup, and Results ... 65
5.1.1 Experimental Long-form Stability Tests ... 67
5.1.2 Experimental PID Control Tests ... 69
5.2 Actuator-Plant Analysis ... 71
5.3 MATLAB-Simulink Control Model Simulation ... 75
5.4 Optimized PID Response Comparison ... 79

Chapter 6 Final Remarks 82
6.1 Contribution 82
6.2 Future Research and Design 83
6.3 Summary 85
References 86
Appendices 93
Appendix A: MATLAB Code: HomogeneousMaterialCalculator.m 93
Appendix B: MATLAB Code: ThermistorConverter2.m 94
Appendix C: MATLAB Code: ZeiglerNicholsAutoCalculator.m 95
Appendix D: MATLAB Code: InputDependentGain.m 96

LIST OF TABLES

Table 1: Homogeneous Material Definitions 14

Table 2: Hardware Component List 52

Table 3: Experimentally Determined PID Tuning Variant Gains. 69

Table 4: Optimal simulated PID values. 78

LIST OF FIGURES

Figure 1.1: Optical photonics array [16]. 4

Figure 1.2: OPA complete layout (left) compared to only the electrical and trench layers (right). Image credit: Chauhan. 5

Figure 2.1: Heat Conduction through a large plane wall of thickness Δx and area A. 12

Figure 2.2: Thermal Contact Conductance 13

Figure 2.3: P/N 1600-10K Thermistor: Typical Resistance vs. Temperature Graph [35] 23

Figure 3.1: Not-to-scale model close-up of a single phase shifter 26

Figure 3.2: Phase shifter cross-sectional diagram displaying boundary conditions & dimensions 27

Figure 3.3: Initial COMSOL Model – Three full featured OPA phase shifters in parallel. 29

Figure 3.4: COMSOL 3D OPA Model 30

Figure 3.5: COMSOL 3D OPA Model – FEM mesh. 31

Figure 3.6: COMSOL 2D OPA Model - Phase shifters to-scale 32

Figure 3.7: Total available active phase shifters for the experimental OPA. 33

Figure 3.8: Change in temperature through the OPA center layer with respect to ideal control setpoints. 36

Figure 3.9: COMSOL 2D OPA Model temperature distribution across center long edge of OPA with ideal thermal control. 38

Figure 3.10: COMSOL OPA temperature difference from 300K ambient given a step input at various setpoint boundaries for a single waveguide. 39

Figure 3.11: COMSOL 2D OPA Model Temperature response at 33% and 100% power with no thermal control. 40

Figure 3.12: COMSOL 2D OPA Temperature difference for inactive phase shifters adjacent to an active phase shifter. 41

Figure 3.13: COMSOL 2D OPA Crosstalk Adjacency at a 20-degree Celsius setpoint. 42

Figure 4.1: OPA Carrier PCB layout diagram. 45

Figure 4.2: Instrument integration flow chart. 47

Figure 4.3: OPA Carrier board (OPA chip not present)........ 47

Figure 4.4: OPA Honeywell laboratory test setup. 50

Figure 4.5: The on-ship OPA fully integrated an optically coupled. 50

Figure 4.6: Complete hardware layout for experimental thermal tests. 51

Figure 4.7: Complete thermal and optical hardware setup for experimental testing of York. 54

Figure 4.8: Voltage divider for thermistor (R_2) reading. 55

Figure 4.9: Electrical and thermal performance of TEC module according to datasheet [29]........ 57

Figure 4.10: Temperature response without heatsink versus with a heatsink present. 58

Figure 4.11: Initial thermal response step tests of 33/100 active phase shifters at 6.5V and 10V of power. 60

Figure 4.12: Incrementing active phase shifter groups. 61

Figure 4.13: Temperature response of increasing number of active phase shifters at 10V. 62

Figure 4.14: Phase shifter temperature relationships. 62

Figure 4.15: Direct comparison of temperature response between 2D COMSOL model and experimental measurements........ 64

Figure 5.1: MATLAB-Simulink thermal control code diagram. 66

Figure 5.2: Long term setpoint stability based on maximum phase shifter power output. 68

Figure 5.3: Staircase step tests for distinct groups of PID values. 70

Figure 5.4: Step Response for experimentally derived transfer functions. 71

Figure 5.5: Step response for experimental transfer functions (blue) and modified transfer functions (red). 73

Figure 5.6: Bode plot comparison of experimental transfer functions to modified transfer functions. 74

Figure 5.7: Nyquist plot comparison of experimental transfer functions to modified transfer functions. 74

Figure 5.8: Simulink thermal control loop for actuator-plant model comparison. 75

Figure 5.9: Input dependent gain actuator-plant model approach........ 76

Figure 5.10: Input dependent transfer function if statement block. 77

Figure 5.11: Response plots for optimized PID value simulations. 78

Figure 5.12: Experimental staircase step results based on the simulated controller gains. 79

Figure 5.13: A zoomed in version of the experimental comparison tests showing the first three 100s step inputs of 0V, 7V, and 1V respectively. 80

Figure 5.14: Scatter plot of observed settling times per voltage drop/jump. 81

Chapter 1
Introduction

Optical Phased Array (OPA), also referred to as Phased array optics, is a solid-state optical platform designed for the purpose of achieving accurate laser steering over several thousand kilometers. OPAs manipulate optical properties to transmit and steer coherent beam patterns for long range communications. In space applications, OPAs are proposed to achieve secure, long-distance bi-directional communication in the space environment for satellite-to-satellite optical communications [1], [2].

In collaboration with Honeywell/COM DEV, National Research Council (NRC), and several academic partners, we have investigated a novel on-chip OPA design using micro-photonics technology. The proposed silicon-photonics design and layouts that make up the OPA have been conceived with the help of multiple university teams including York University, University of Toronto, Carleton University, and Western University. The array of 100 powered elements is designed to effectively steer the emitted signals through wavelength modulation by temperature tuning. The thermal sensitivity of these elements is a function of their geometry; consequently, they are significantly influenced by thermal crosstalk. To counteract overheating and thermal crosstalk, active temperature control is required to achieve an operational level of precision.

The thermoelectric effect has been proven to provide control and thermal stability in various devices [3]–[5]. This thesis presents the simulation and testing of a thermo-electric cooler (TEC) to ensure effective operation of the OPA.

1.1 Silicon Photonics in Space

As our world shifts at an unprecedented rate towards a state of growing digital dependency, our demand for data (both in volume and speed) are rapidly outpacing existing RF-based network architecture. As a response to this need, optical communications were considered favorably for their potential to achieve long range and high resolution [1]. However, as these networks grow and their signals carry greater bit rates among multiple wavelengths, the need for a scalable optical or photonic technology becomes critical [2]. Optical beam steering is an emergent technology aimed at tackling that problem. It is the LIDAR equivalent to RF antennae, which instead operate in the visible, infrared, and near-infrared spectrums [3]. Current beam steering systems use mechanical systems, such as MEMS driven micro-mirrors and micro-lenses, or solid-state systems, such as polarization gratings and optical phased arrays (OPAs) [7], [9]–[11]. Mechanical systems suffer from their reliance on slow and bulky moving components, which represent weak points of mechanical stability in the face of environmental effects including vacuum, cryogenic temperatures, radiation, shock and vibrations, and acoustic loads [1], [12]. Mechanical actuators under vacuum are subject to shock and vibration damage as the removal of air resistance increases speed of component actuation, however actuators also may suffer from sticking effects or degradation on contact [1]. Both radiation and cryogenic temperatures result in the deformation and degradation of optical surfaces and coatings. Previous mechanical beam steering solutions lack the ability for rapid pointing and require high mechanical complexity and therefore cost [13]. Solid-state systems by comparison are more compact and allow for faster steering than their mechanical counterparts as a result of their lack of moving components [12], [14]. Multiple solid-state systems have been studied but all are limited in some manner through some combination of scattering, low throughput, and small steering angles or apertures [2], [3], [6], [8], [12], [14].

Despite this, solid-state systems are preferred due to increased system stability and robustness [12]. These features are critical for mission success given the volatility of the space environment. In addition, silicon-based solid-state systems benefit from their compatibility to complementary metal-oxide semiconductor (CMOS) fabrication processes. The CMOS process allows for large-scale fabrication of highly integrated silicon photonic circuits at exceptionally low costs [15].

1.2 Optical Photonics Array

The platform under development is an OPA solution for accurate beam steering in the space environment. The final OPA design, referred to internally as the Honeywell On-chip Optical Photonics Array (HOOPA), is a silicon-based microphotonics beam steering platform that is intended to operate in the space environment and is manufactured using CMOS fabrication technology. OPAs are an array of coherent optical emitters, whose relative phase is modified such that the signals emitted by the antennas interfere constructively, creating a far-field radiation pattern in which the angular position of the main lobe can be selected by setting the correct phases in the individual antenna elements as seen in Figure 1.1 [14], [16].

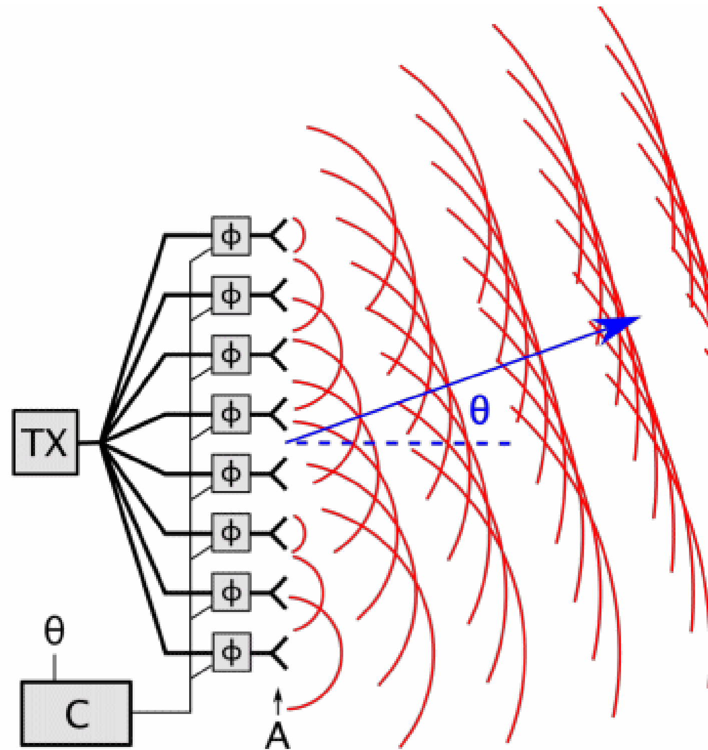

Figure 1.1: Optical photonics array [16].

Solid-state OPAs require optical modulation to steer the beam formation. Thermal modulation involve generating a thermal gradient around the desired phase shifter element, while also trying to minimize thermal crosstalk between adjacent elements [17]. There have been multiple approaches to combinations of 1D steering and optical modulation for solid-state or mechanical OPAs. Thermal actuation in conjunction with the thermo-optic effect demonstrated a magnitude of greater performance than the thermo-optic system alone, but requires the dual complexity of both types of systems [3]. Electrothermal actuation for microlenses demonstrated a effective 2D beam steering but involve the use of optically sensitive lenses [10]. The piezoelectric effect has been used to great effect in steering micromirrors in 1D, however this approach lacks optical modulation [11]. Solid-state 1D and 2D beam steering with switchable polarization gratings and waveplates have been demonstrated successfully but this method results in coarse steering,

where the system is locked to an array of fixed angles rather than free steering [12]. Electro-optical modulation has also been demonstrated where a driving voltage induces an effective variation in the refractive index of specified waveguides [18].

This iteration of the OPA design implements thermo-optical modulation where the method in which a change of phase is achieved using phase heaters. They are thin strips of deposited metal that run along the length of each waveguide element, whose temperature are determined by the input power and resulting impedance. The OPA design layout in Figure 1.2 shows these elements in parallel, as well as the multitude of test structures around the edges (left).

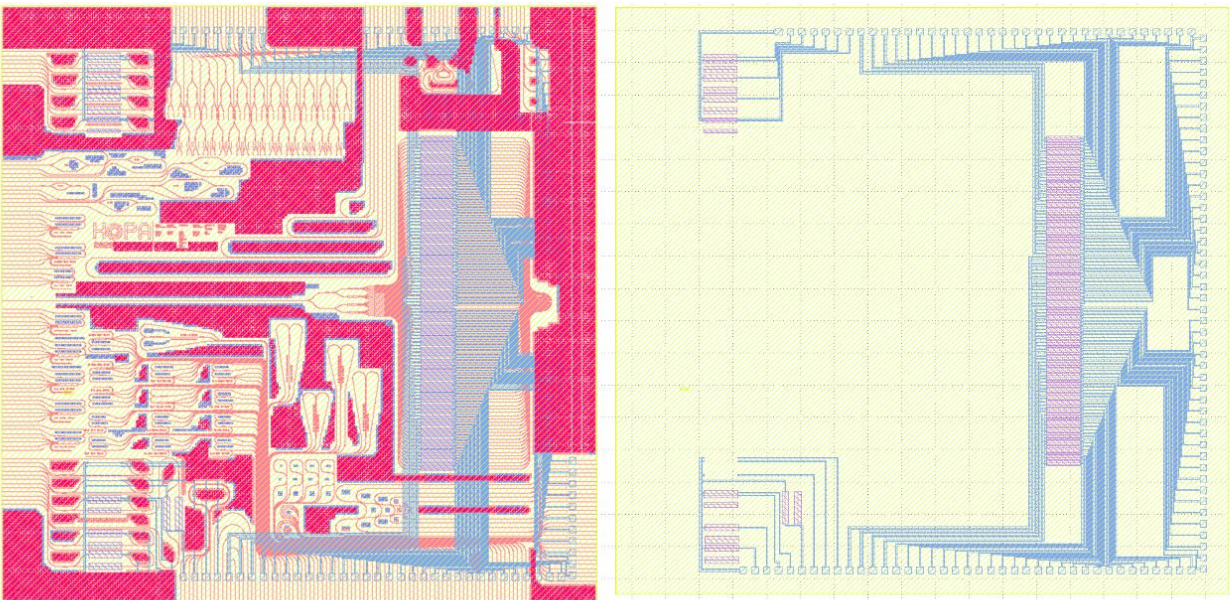

Figure 1.2: OPA complete layout (left) compared to only the electrical and trench layers (right). Image credit: Chauhan.

Upon removing all the other layers for the image on the right, we can see the electrical layer in blue and the trench layer in violet. The hundred parallel aligned trenches on the right make up the OPA. However, due to how these resistive heaters are integrated in the architecture, the heat dissipation causes high thermal gradients across thermally sensitive regions, which result in the

formation of hot spots. The fundamental sensitivity of silicon-based photonics demands incredibly strict thermal control to maintain desired performance benchmarks.

1.3 Research Objectives

The primary research objectives of this thesis are to (1) conduct a thermal analysis of the OPA using the Heat Transfer Module of COMSOL Multiphysics software, and (2) to design a thermal control subsystem based on both simulation and experimental results. This includes the complete overview of the thermal model used, the experimental hardware setup, and the controller design for optimum performance. Research tasks are structured into three sections: (1.1.1) thermal model analysis; (1.1.2) hardware level design and integration; and (1.1.3) control design characterization and testing.

1.3.1 Thermal Model Analysis

This goal involves the analysis of the active thermal profile of the OPA under expected modes of operation to determine the shape and power of the thermal compensation required to maintain uniform thermal stability. OPAs of these designs strive to manage the thermal gradient between their active components and their thermal-sensitive elements [19]. It is crucial to determine the effects of an active thermal profile; whether it be the identification of hotspots or quantifying the fraction of unavoidable thermal crosstalk, these factors contribute strongly to signal noise and accuracy. Analysis of the thermal profile will be simulated in the multi-dimensional format of COMSOL Multiphysics, where the Joule Heating simulation module is incredibly effective in translating the effect of electric resistance heating on surrounding material geometry.

The design of the OPA incorporates well-documented methods of passive thermal control with the use of air trenches and material selection. Simulated models were used to identify thermal performance under a strict set of benchmarks in lieu of a complex analysis of their analytical counterparts. These results define the performance requirements for the accompanying TEC module and the rate at which heat is being generated under full power operation.

1.3.2 Thermal Electric Cooler (TEC) Hardware Design and Integration

To evaluate and operate the optical control and thermal control for the on-chip OPA, a combination mounting and connector system was required. A printed circuit board (PCB) was necessary and acted as a middle ground to facilitate the following setup elements: the electrical connections required to drive the on-chip circuitry, the space necessary to mount and control the external thermal control system, the ability to couple the optical inputs right up to the very edge of the chip without obstructions, and enough open space to properly set up and utilize a series of cameras, microscopes, and lenses for observation and recording. The on-chip circuitry is connected to a series of external current driver devices, data acquisition modules, and Honeywell's existing external power amplification control circuits. The existing hardware at Honeywell was repurposed and designed to independently manage the stable controlled current for all one hundred phase shifters in the array. The purpose of the design is to allow each collaborating team to effectively test and operate the device-level components.

1.3.3 Control Design Characterization and Testing

From the results of the thermal model analysis, the proposed system-level thermal environment is quantified, and the independent efficacy of an external thermal control system can be defined. The implementation of a proportional-integral-differential (PID) controller will make use of a feedback

control loop running on MATLAB-Simulink. The TEC module will have its current input corrected by the translated voltage readings of thermistors, carefully placed at available junction points on the OPA. Additional thermal imaging by high resolution thermal cameras will accrue supplementary data to help validate measured temperatures from the other sensors. Observing the resultant surface temperatures during operation will establish the accuracy of the predetermined assumptions with respect to boundary conditions. The optimization of the control algorithms for faster stabilization and noise filtering depends on the time response of the TEC in addition to the time response of phase changes from the active OPA elements.

1.4 Design Limitations / Boundaries

The OPA project under Honeywell contains a variety of microphotonics structures, each of which have been the rigorous design research of the multiple partnered university teams. Considering the state of the ongoing research and design for this greater project, available resources and time constraints must be accounted for. The scope of this thesis work is subject to boundaries pertaining to both hardware and software. First, the thesis work includes only the hardware integration design and setup for the current (V1) iteration of the manufactured OPA chip in 2021. Second, the thesis work presents simulated thermal modelling from COMSOL Multiphysics, no other simulation software is included. Lastly, the thesis work has limited commercialized product involvement and aims to demonstrate that active thermal control can be achieved with commercial off-the-shelf (COTS) components in later iterations of the design. The scope and requirements for performance metrics to be achieved in the design have been assigned by Honeywell and include the following.

- Complete TEC temperature controllers are commercially available, as well as compact electronic modules for processing and control. Utilizing these products would defeat the versatility of the system proposed and will only be used for validation (if available).

- The system design is to be low cost and applicable for several iterations of similar systems and laboratory setups across the multiple participating university teams.
- Long term temperature stability: the OPA is intended to be capable of operating continuously for several hours or longer. Error correction is necessary to maintain control and accuracy over long periods of time where drifts or instabilities may arise.
- Automatic and Manual Setpoint Operation: The control system should allow for continuous operation for both modes. Automatic mode should maintain minimum user interaction, while manual mode should present the user a freely modifiable system.

1.5 Thesis Contribution

This thesis outlines both a simulated and a physical hardware approach to thermally control an OPA for both laboratory and space environments. While the focus centers around laboratory operation, the design work and optimization act as a groundwork for future OPA designs and packaging iterations intended for space applications. There are three main contributions made by this thesis to the OPA project.

i. Thermal crosstalk performance metrics of the OPA by observing the response from simulated 2D and 3D multiphysics model.
ii. Hardware integration platform using solid state temperature actuation from commercial off-the-shelf (COTS) components to allow the team unperturbed optical testing.
iii. MATLAB-Simulink simulated actuator-plant system for characterizing PID control for optimizing settling responses at required temperature setpoints.

1.6 Thesis Outline

This report presents the detailed process of the analytical and simulated thermal models, the test hardware design, and the resultant thermal controller optimization for the OPA chip. Chapter 1 provides a brief introduction of the motivation and objectives that this thesis tackles. Chapter 2 presents the background and precedent technological innovations as well as the fundamentals of the simulated mathematical models. Chapter 3 chronicles the COMSOL simulation modelling and results for the active case studies in both steady-state and time dependent formats. Chapter 4 contains the hardware design and interface, as well as the characterization and validation for the experimental test setups. In Chapter 5, the process for designing and optimizing the PID controller is laid out. Finally, Chapter 6 contains the conclusion of the analysis accompanied by recommendations for future work for upcoming design iterations of the OPA chip. Appendices and references bookend this report.

Chapter 2
Background

The growing demand for digital infrastructure for in-orbit applications has far exceeded the limits of old space hardware, thus the implementation of new infrastructure requires extensive testing and validation. Designing a temperature controller for a novel technology requires considerations for both the fundamental nature of the material construction and the environment in which it resides. Whether it be through analytical solution or simulation, understanding the response of temperature sensitive elements on the micro scale leads to a more refined implementation of control. This chapter discusses the impetus for transitioning to this technology, what defines its successful operation, what makes up the mathematical bounds of the thermal profile, and how effective control can be conducted.

2.1 Principles of Heat Transfer Theory

The thermal profile of the OPA chip can be described using the fundamental heat transfer equations [20]–[23]. There are three primary models of heat transfer, each of which is an observation of a specific energy transfer mechanism. These three models are Conduction, Convection, and Radiation. Of those three, convection is not generally applicable in the space environment, due to the nature of the surrounding vacuum. Each of these models are explored in detail with respect to their appropriate relevance to the case studies. From these models, their boundary and material properties are expanded upon. The thermoelectric effect in its constituent principles is also discussed.

2.1.1 Conduction

Conduction is predominantly defined as the transfer of energy from more energetic to less energetic particles across a substance because of their interactions. The rate at which conduction occurs is dependent on geometry, thickness, material, and temperature difference across a medium. The change in energy in watts is defined by $\dot{Q}$.

Fourier's law of heat conduction expresses this relationship most clearly in the fundamental case of steady-state conduction through a large plane wall of thickness $\Delta x = L$ where the temperature difference with respect to both ends of the wall is defined by $\Delta T = T_2 - T_1$ seen in both equation 2.1 and Figure 2.1 [24].

$$\dot{Q} = \frac{kA(T_1 - T_2)}{\Delta x} = -kA\frac{\Delta T}{\Delta x} = -kA\frac{dT}{dx} \quad (W) \tag{2.1}$$

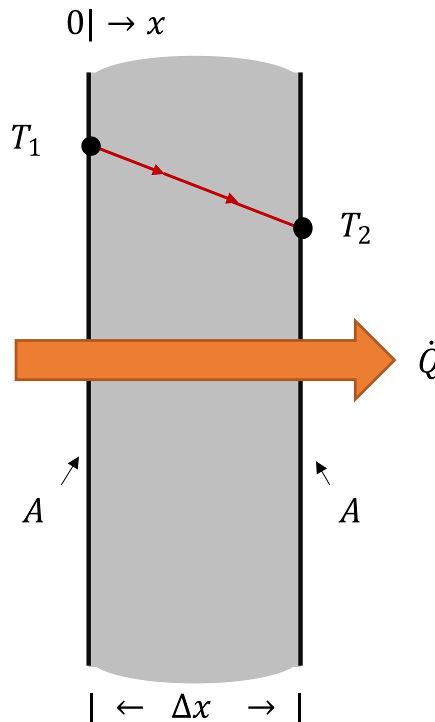

Figure 2.1: Heat Conduction through a large plane wall of thickness Δx and area A.

Thermal conductivity of the medium is defined by k in $\frac{W}{mK}$ as is the cross-sectional area of the surface by A in m^2. The rate of heat conduction through the plane is proportional to the temperature difference across the layer and inversely proportional to the layer thickness.

2.1.2 Thermal Contact Conductance

To define the heat conductance between bodies, we consider a two-body case A_1 and A_2 as shown in Figure 2.2. The heat flowing from the hotter body A_1 to the colder body A_2 can be described by equation 3.2:

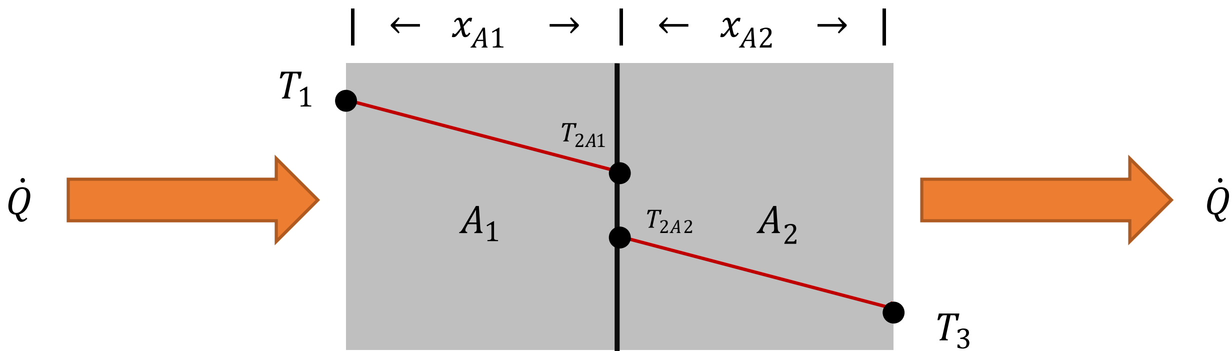

Figure 2.2: Thermal Contact Conductance

$$\dot{Q} = \frac{(T_1 - T_3)}{\frac{\Delta x_{A_1}}{k_{A_1}A} + \frac{1}{h_c A} + \frac{\Delta x_{A_2}}{k_{A_2}A}} \quad (W) \tag{2.2}$$

Where A is the contact area between the two bodies, T_1 and T_3 are the end temperatures, Δx_{A_1} and Δx_{A_2} are the thicknesses through which the heat has conducted, and h_c is the coefficient for thermal contact conductance.

2.1.3 Homogeneous Materials

The thermal conductivity value of most uniform materials is known and catalogued. However, there are several instances within the design of the OPA where multiple different materials are

used in complex geometries as a function of the deposited layers in the microfabrication process. The OPA contains various geometries of Aluminum, Silicon Nitride, Amorphous Silicon, and Silicon Dioxide Cladding, all of which reside on top of the Silicon wafer. As the thermal conductivity of each of these materials differs, an analytical solution is impractical. A homogeneous substitute material derived from the volume percentages of the initial materials constitute a set of viable material coefficients for calculations. The volume percentage breakdowns and resultant bulk material properties are described in Table 2.1. These values were calculated in MATLAB with the provided code in Appendix A

Table 1: Homogeneous Material Definitions

	Material 1 OPA Print Layer	Silicon Wafer	Material 2 Copper Plug Layer	Material 3 Complete Model
Material Distribution	88% SiO2 10% SiN, 2% Alum	100% Silicon	80.7% FR4 19.3% Cu	71.74% Material 2 28% Silicon Wafer 0.26% Material 1
Density (kg/m^3 @300K)	2694.2	2329	3262.6	3000
Thermal Conductivity (W/mK)	6.4244	130	77.4421	97.0137
Heat Capacity (J/kgK)	704	700	1179.1	1046.8
Electrical Conductivity (S/m)	754800 (S/m)	1e-12	1.1576e7	8.3347e6
Relative Permittivity (-)	11.2860	11.7	3.8245	6.049
Young’s Modulus (Pa)	1.76e11	170e9	3.8984e10	7.6025e10
Poisson’s Ratio (-)	0.2760	0.28	0.1886	0.2144

2.1.4 Convection

Convection is the model of energy transfer between a solid surface and an adjacent liquid or gas that is in motion. Forced convection is the state where the fluid flow over a surface is driven by means of an external force such as wind, pumps, or fans. Natural (or free) convection is the state where the fluid flow over a surface is driven only by the buoyancy forces induced by density differences due to the temperature variation within the fluid and gravity. Despite this complexity, this relationship is modelled by Newton's Law of Cooling as defined by equation 2.3:

$$\dot{Q}_{conv} = h_{conv} A_s (T_s - T_\infty) \qquad (W) \tag{2.3}$$

Where A_s is the surface area experiencing convection, T_s is the surface temperature, T_∞ is the ambient temperature of the fluid, and h_{conv} is the convection heat transfer coefficient in $\frac{W}{m^2 K}$.

There are two distinct environmental scenarios for the operation of the OPA: one defined by the space environment, and one defined in a controlled in-atmosphere environment. For operation in the space environment, it will be assumed that there are no convective forces acting on the model, as the lack of any additional packaging aside from the bodies present implies exposure to the direct vacuum of space. The other case is meant to approximate operation on Earth. Due to the lack of additional packaging at this point in the design process for the OPA, this thesis will present simulated operation and experimental operation exposed only to ambient air natural convection environments.

2.1.5 Radiation

Unlike the modes of conduction and convection, the radiation of electromagnetic waves by means of electronic configuration change on the molecular or atomic level, does not require an intervening medium. All bodies emit energy by this process and the intensity of this radiation depends on the temperature of the body and the nature of its surface. It is both a volumetric and a

surface phenomenon, and as such can be ideally described using the Stefan-Boltzmann law in equation 2.4.

$$\dot{Q}_{rad_ideal} = \sigma A T^4 \qquad (W) \tag{2.4}$$

where $\sigma = 5.67 * 10^{-8}\ W/m^2K^4$ is the Stephan-Boltzmann constant, A is the total surface area of the body and T is its temperature. An ideal radiator is known as a blackbody. Realistically all materials emit a percentage of the total based on various surface properties. This emissivity value is defined by ε where $0 \leq \varepsilon \leq 1$ as seen in equation 2.5

$$\dot{Q}_{emit} = \varepsilon \sigma A T^4 \qquad (W) \tag{2.5}$$

Similarly, a non-ideal body's absorptivity α, of incident radiation is also a defined where $0 \leq \alpha \leq 1$ as Kirchoff's Law of radiation states that the emissivity and absorptivity of a surface at a given temperature and wavelength are equal.

In the case where an intervening medium is present around a body, such as air, radiative heat transfer occurs parallel to convection at the body surface. The total energy transferred by both these processes can be summarized by combining equations 2.3 and 2.5 with respect to the ambient environment in equation 2.6.

$$\dot{Q}_{total} = \dot{Q}_{conv} + \dot{Q}_{emit} = h_{conv} A_s (T_s - T_\infty) + \varepsilon \sigma A_s (T_s^4 - T_\infty^4) \qquad (W) \tag{2.6}$$

In the space environment, heat exchange with the environment is restricted to radiation, which in terms of the volume of heat dissipation is a poor substitute for convection [25].

2.1.6 Boundary Conditions

For materials of finite volume, the properties of heat transfer at the surface, may fall into several categories which are near or under ideally defined circumstances. The boundary conditions present in the analytical model and as defined in COMSOL Multiphysics are as follows.

The specified temperature boundary condition (1) defines a constant value temperature that the system reacts and responds to, stated by equation 2.7.

$$T_s = T(0, t) \quad \textbf{(2.7)}$$

The specified heat flux boundary condition as defined by equation 2.8 (2) denotes the heat transfer rate per unit surface area in W/m^2 on that surface, which is derived from previous equation 2.1 This boundary definition can be altered to represent an adiabatic, or insulated surface, where $\dot{q} = 0$ in equation 2.8. This boundary implies zero heat transfer through a surface and results in a relative mirroring effect with respect to the directional flow of energy through the bulk material.

$$\dot{q} = \frac{\dot{Q}}{A} = -k\frac{dT}{dx} \qquad (W/m^2) \quad \textbf{(2.8)}$$

A convective boundary condition, as derived in equation 2.3, can be represented by substituting the heat transfer rate per unit surface area of equation 2.8, as seen in equation 2.9 where the negative sign indicates directionality. In the work of this thesis, h_{conv} is represented by a constant or is equal to zero. It represents the natural convection of the air environment, or the vacuum of space, respectively.

$$-k\frac{dT}{dx} = h_{conv}(T_\infty - T_s) \qquad (W/m^2) \quad \textbf{(2.9)}$$

In the case where a material is cutoff in a model due to size or scope limits, but the thermal impact of that cutoff material is negligible, it is suitable to implement a thermal insulation boundary condition, as stated in equation 2.10. This boundary condition is used conservatively as an approximation for cutoff material since it generates an effect of thermal mirroring within the material present. The heat that would have dissipated through that surface originally is reflected

back into the domain. This is employed only when the material beyond the boundary has negligible heat sink characteristics.

$$\frac{dT}{dx} = 0 \tag{2.10}$$

2.1.7 Joule Heating

The conversion of electrical energy in a circuit into thermal energy because of the electrical resistance of a conductive material is known as Joule Heating. This process is the fundamental method for generating heat energy within the OPA. The relationship between material type and dimensions is based on the equation 2.11, where the dimensions of the resistive element in this case are those of the OPA heaters.

$$P = I^2R = I^2\left(\rho\frac{L}{tw}[1 + \alpha(T - T_{amb})]\right) \quad (W) \tag{2.11}$$

L, t, and w, are the length, thickness, and width of the resistive element respectively. The material resistivity at ambient temperature T_{amb} is represented by ρ and the thermal coefficient of resistivity by α. By comparing the difference in input power P to resultant temperature T at a fixed ambient temperature, a joule heating element can be sized to match a desired temperature difference.

2.1.8 The Thermoelectric Effect

Also recognized as the Peltier effect or the Peltier-Seebeck effect, this phenomenon is a combination of the observational relationships defined by the Seebeck effect and the Peltier effect. The Seebeck effect is observed when two ends of a conductor are each kept at a different temperature, which generates an emf voltage between the two junctions. The Seebeck coefficient

α_s, of a material represents how much emf voltage is generated by the temperature gradient as seen in equation 2.12 [4].

$$V_{emf} = \alpha_s \Delta T \qquad \textbf{(2.12)}$$

It is important to note that the Seebeck coefficient of a material is not constant with respect to wide ranges in temperature. However, given the range of temperatures under consideration in this thesis, this gradient is so small it can be considered negligible.

The inverse of the Seebeck effect is the Peltier effect, where passing a current through two junctions of dissimilar metals generates a temperature difference between them, where the heat present is either absorbed or rejected depending on the direction of the current [5]. The Peltier coefficient Π, is directly related to the Seebeck coefficient by temperature as follows:

$$\Pi = \alpha_s T \qquad \textbf{(2.13)}$$

The amount of heat generated per unit time with respect to current and the Peltier coefficients of both junction materials A and B are:

$$\frac{dQ}{dt} = (\Pi_{\mathrm{A}} - \Pi_B)I \qquad (W) \qquad \textbf{(2.13)}$$

The practical application of the thermoelectric effect in physical devices involves utilizing arrays of junction couples where the materials are selected based on their electrical and thermal conductivity. A unitless figure of merit $\mathbb{Z}$ defines the realistic performance of a material in a thermoelectric system as seen in equation 2.14.

$$\mathbb{Z} = \frac{\alpha^2 \sigma}{\kappa} \qquad \textbf{(2.14)}$$

Where σ is the electrical conductivity and k is the thermal conductivity. The performance and thus the figure of merit of a material is preferable when the electrical conductivity is maximized, and the thermal conductivity minimized.

2.2 Principles of Control Theory

The focus of this thesis research is the accuracy and uniformity of the system level thermal environment. Our goal is to further increase the performance of the chip-level elements and, by association, the far-field radiation pattern of the OPA. Previous analysis and experimentation have discovered various methods for passive or internal thermal control on the hardware level, including various depths of air trenches, the inclusion of copper shunts, graphene nanoheaters, and through-oxide thermal vias [26]–[28]. While a limited number of passive options have been employed, they cannot perform the level of thermal mitigation required without the aid of active (external) thermal control techniques such as air-cooled heat sink fins, and thermoelectric cooler (TEC) units. A TEC module was chosen as the selected external thermal control driver due to its efficacy in displacing heat in both atmosphere and vacuum environments. Solid state systems are preferable in the space environment as the lack of moving parts ensures less points of mechanical failure in the overall mission design. This section discusses the fundamental elements of feedback PID controllers used in this work, as well as the governing equation for active thermal sensing and response.

2.2.1 Actuator-Plant Model

To utilize a feedback control loop technique for power regulation of the TEC and therefore thermal control, the general relationship of a Peltier device must be defined and rearranged to represent one or a series of transfer functions. In the case of our simulated and experimental system the actuator and plant models are interconnected in a direct enough manner where one primary model is sufficient representation of the process. The general equation for the heat flow displaced from the cold side of the TEC to the hot side is seen in equation 2.15.

$$\dot{Q}_c = \alpha T_c I - \frac{1}{2} I^2 R - K_t (T_h - T_c) \tag{2.15}$$

Where T_c and T_h are the cold and hot side temperatures of the TEC, while K_t and R are the thermal conductance and resistance respectfully. Further definitions in equations 2.16, 2.17 and 2.18 can be established based on values taken from the TEC datasheet [29]. These constants are defined based on a fixed T_h value and include V_{max}, I_{max}, $\dot{Q}_{max}$ and ΔT_{max} which are voltage, current, heat flow, and change in temperature maximums respectfully.

$$\alpha = \frac{V_{max} I_{max} + 2\dot{Q}_{max}}{I_{max}(\Delta T_{max} + 2T_h)} \quad \textbf{(2.16)}$$

$$R = 2\frac{V_{max} I_{max} T_h - \dot{Q}_{max}\Delta T_{max}}{I_{max}^2(\Delta T_{max} + 2T_h)} \quad \textbf{(2.17)}$$

$$K_t = \frac{2\dot{Q}_{max} T_h - \Delta T_{max}(\dot{Q}_{max} + V_{max} I_{max})}{\Delta T_{max}(\Delta T_{max} + 2T_h)} \quad \textbf{(2.18)}$$

This relationship can be defined now as the change in temperature across the TEC as a function of input current as seen in equation 2.19, however this relies on a constant T_h value. An assumption that does not translate neatly to the real-world experiments.

$$\Delta T = T_h - T_c = \frac{\alpha T_h I - \frac{1}{2} I^2 R}{\alpha I + K_t} \quad \textbf{(2.19)}$$

There have been many approaches to resolving this discrepancy through detailed analytical solutions or RLC circuit representations, but each are directly dependent on hardware layouts and assumptions which are specific to the given system and cannot be applied to other systems [30]. One variation recognized that the relationship between PWM current input and ΔT could not result in a direct derivation but could be appropriately approximated with a power law function as per equation 2.20 [31].

$$\Delta T = a\left(\frac{I}{I_M}\right)^b \quad \textbf{(2.20)}$$

Where I_M is the maximum available power in our hardware environment and is not the same as I_{max}. This is then defined by a and b which are parameters derived from experimental results.

The model of the TEC can be sufficiently approximated therefore by the change in temperature between the two plates and therefore be treated as first order by assuming a lumped system or linearizing [32], [33]. This generalization also considers simplifying the non-linearity of the sink and the load [34]. This transfer function is therefore defined by equation 2.21.

$$G(s) = \frac{K_p}{\tau_s s + 1} \quad \textbf{(2.21)}$$

where K_p is the gain defined by equation 2.19 and τ_s is the time constant of the system, also determined experimentally.

2.2.2 The Steinhart-Hart Equation

The PID control method employs an active sensor to compare the current state of a system to its expected performance based on input parameters. In the case of the OPA, the PID control response being generated and measured is thermal, thus an appropriate temperature sensor is required. Thermocouples or larger integrated electronic package sensors would be too cumbersome to mount onto the OPA for our purposes. Thermistors are some of the smallest available commercial temperature sensors, with many available temperature sensing ranges. A thermistors' resistance varies proportionally to the temperature present. Positive Temperature Coefficient (PTC) thermistors correlate positively with temperature, while Negative Temperature Coefficient (NTC) thermistors correlate negatively. The relationship between resistance and temperature is defined by the Steinhart-Hart Equation in equation 2.22.

$$\frac{1}{T} = A + B * \ln(R) + C * \ln(R)^3 \quad \textbf{(2.22)}$$

where A, B, and C are the defining coefficients. The thermistor selected for the experimental tests for the OPA is a P/N 1600-10K NTC Thermistor, whose defining coefficients are $A = 1.12924E - 03, B = 2.34108E - 04, C = 0.87755E - 07$ [35]. The resistance to temperature relationship as defined by the datasheet is seen in Figure 2.3.

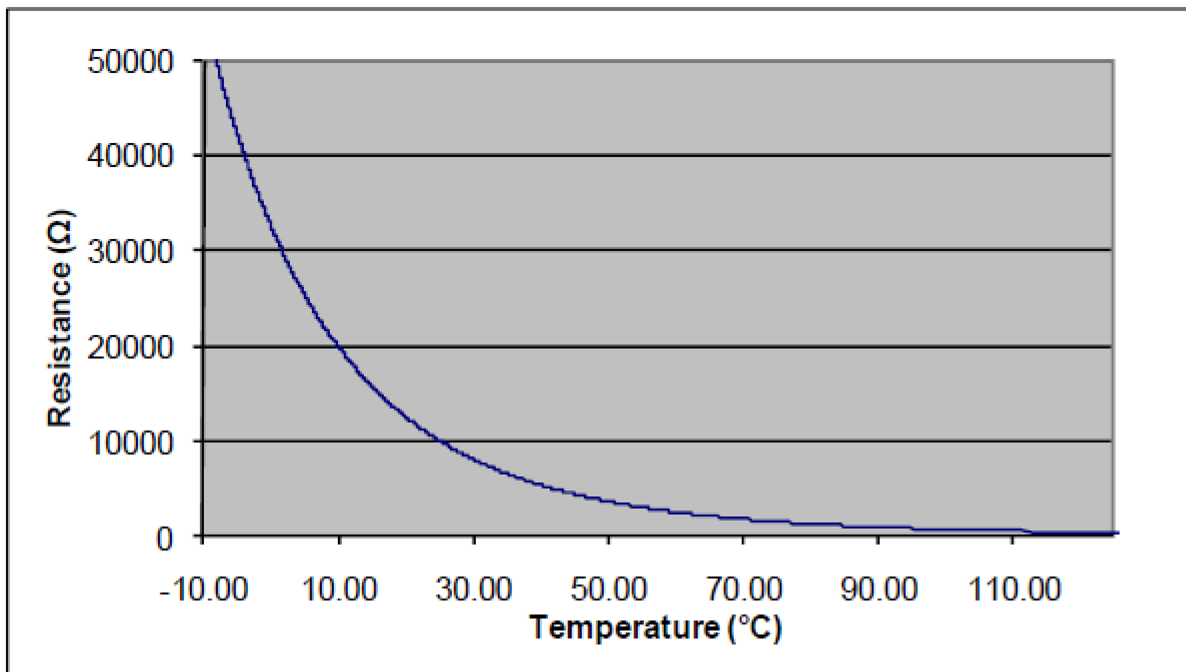

Figure 2.3: P/N 1600-10K Thermistor: Typical Resistance vs. Temperature Graph [35]

2.2.3 PID Control Design

With a combination actuator-plant model and a feedback sensor, our system can recognize the difference between the setpoint (reference temperature) and active temperature (measured temperature in real-time) but cannot reduce the difference between those values to zero without a controller. The offset from setpoint is considered the error of the system. For a control system to reduce the error to zero, it must be able to track the reference and active signals effectively and reject major or minor disturbances in the signal. The proportional integral and derivative (PID)

approach to controller design confers system stability and robustness. The PID equation in the time domain (2.23) and in the s domain (2.24) show how each of the proportional, integral, and derivative terms of the error are considered.

$$u(t) = k_P e(t) + k_I \int_{t_0}^{t} e(\tau) d\tau + k_D \dot{e}(t) \quad \textbf{(2.22)}$$

$$C(s) = k_P + \frac{k_I}{s} + k_D s \quad \textbf{(2.22)}$$

While MATLAB and Simulink have built-in applications and tools for tuning the PID gain values based on simulated results, it is prudent to compare their performance to additional methods of PID tuning. Heuristic PID tuning involves measuring the ultimate gain value and oscillation period directly from experimental results to derive the PID values. There are several heuristic methods available; however, those requiring exact lag measurements are not available for this application due to the decoupled nature of the OPA (optical phase) control and the thermal control. The lag, or deadtime, is defined in this case as the time it takes the feedback sensor to register a change made by the OPA power control. The Zeigler-Nichols method of tuning was the predominant approach, where multiple variants of the method were considered as they have proven effective in similar implementations [36], [37].

Chapter 3
Thermal Modelling of OPA

The models for the first iteration of the OPA design for thermo-optic signal manipulation were developed using COMSOL Multiphysics 5.5 with support from MATLAB for the post-processing of data. By implementing the Heat Transfer module in COMSOL, the discretized mesh of the 3D geometry allows for an ample analysis of the flow of heat. The simulation models were developed such that updates to material definitions, boundary conditions, and power variations could be investigated and compared under the same platform. These models have been designed from the ground up using the geometries of the manufactured designs and incorporating a conservative implementation of homogeneous material definitions. The fundamental heat dynamics formulas defined in Chapter 2 show the structure in which the definitions of the COMSOL models are translated into tangible values. All simulation models are computed for two distinct cases: 33% maximum power and 100% maximum power, as a function of the available experimental data described in Chapter 4.

3.1 Phase Shifter Design

As COMSOL Multiphysics utilizes a finite element method approach to solving its models, the ability to effectively represent a system is dependent on the model's complexity [38]. Generating a full 3D model of the entire OPA as seen previously in Figure 1.2, would result in billions of mesh elements that differ in size by up to five orders of magnitude. Thus, the scope of the models had to take on a more stringent focus of the thermally mitigating design solutions beginning with the passive structures.

There have been many previous approaches to layout designs in photonics that passively isolate thermally sensitive regions [26]–[28]. As a function of the layout complexity between features on the component level across different microphotonics applications, maximizing performance involves precision analysis on a case-by-case basis [39]. The well documented methods that have been employed to thermally isolate the OPA phase shifters from one another are the use of air trenches, and thermally favorable material allocation for optical elements and cladding. Since the OPA was realized using silicon photonics, the optical components are made of silicon nitride (SiN), while the cladding is silicon dioxide (SiO2). All layers of electrical traces and tapers are Aluminum. The thermal performance as a function of input power is simulated to resolve the maximum thermal crosstalk between active and inactive phase shifters. A not-to-scale model of a phase shifter was created to indicate the shape and positions of the entities present in each branch of the array structure. It is seen in Figure 3.1 where one phase shifter contains a single phase heater and a single waveguide.

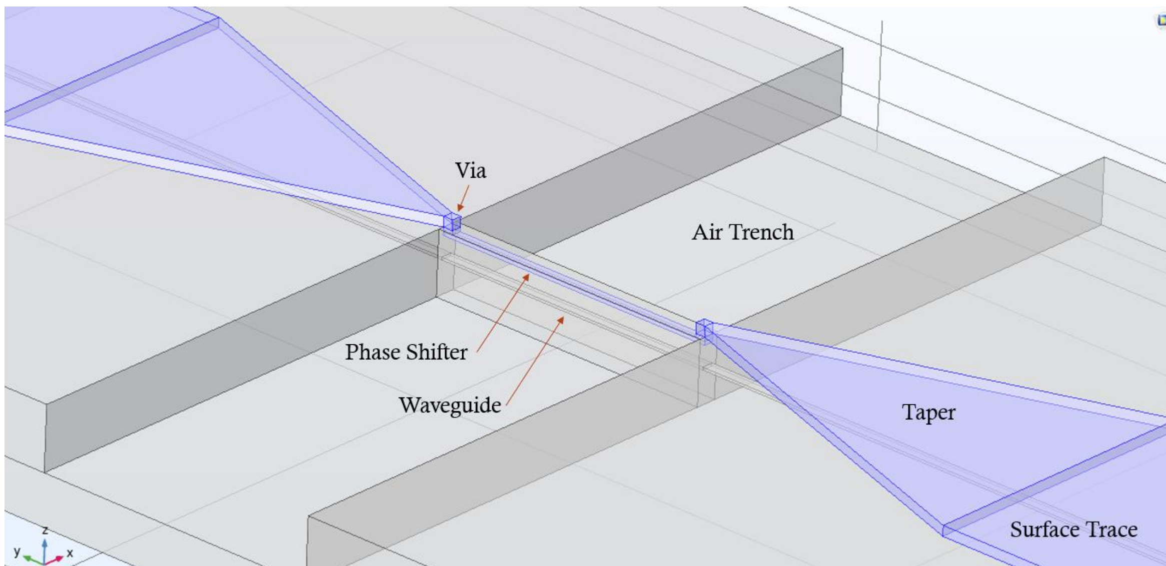

Figure 3.1: Not-to-scale model close-up of a single phase shifter

Figure 3.2, also not to scale, displays the cross-sectional layout of a pair of phase shifters where the designated heat source is the resistive heating done by a thin buried trace, and the constant temperature boundary is a stand-in for an ideal TEC which can generate a consistent uniform thermal gradient, as non-uniform pathways have been proven to be less efficient [40]. The radiative heat transfer (previously detailed in Chapter 2) is proportionally greater at temperatures far exceeding our upper limits. Within our limits and at our component scale, the radiative forces were deemed negligible by comparison to the convection boundaries and forces [41].

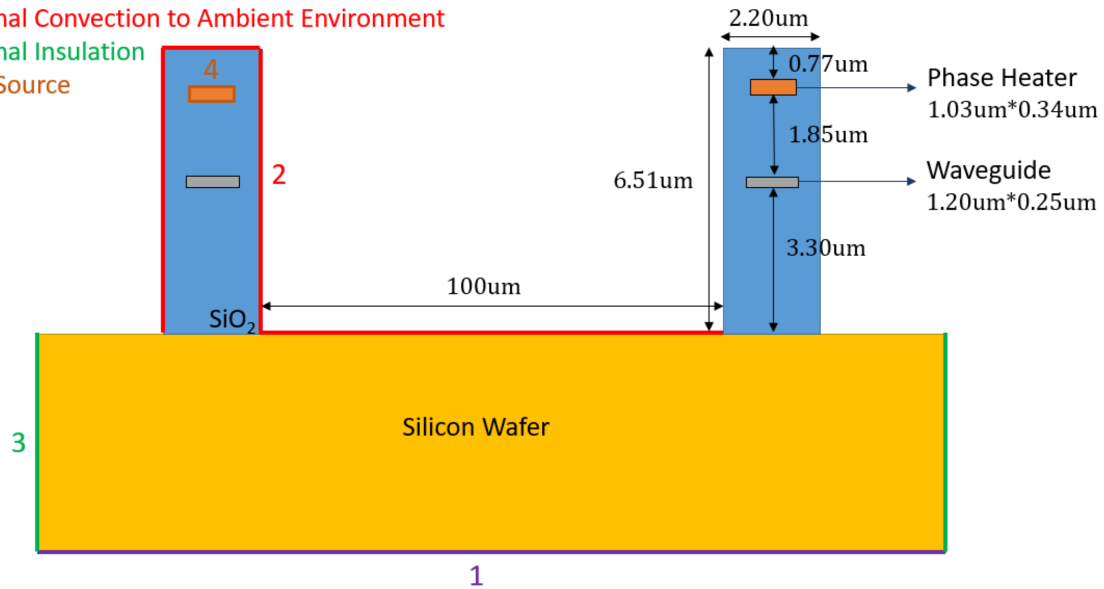

Figure 3.2: Phase shifter cross-sectional diagram displaying boundary conditions & dimensions

The dimensions used in the manufactured OPA and our simulated models are derived from previous optimization research conducted by a group of researchers at the University of Toronto, led by Prof. Helmy [42]. Previous research involved defining the size, shape, and spacing of the heater, the waveguide, and the trenches for each phase shifter component in the array. Optimization was focused on reducing thermal crosstalk and optical losses while maintaining efficient power draw.

The final OPA design incorporated tapered traces and vias on each end of the phase shifter to connect down through the SiO2 layer. Each phase shifter is separated on each side by 50um of space, resulting in 100um wide trenches between phase shifters. Each trench is 100um across and runs the entire length of each phase shifter. The full size of the silicon wafer after being diced in the manufacturing process is 17.2mm by 17.2mm with a thickness of 0.725mm.

3.2 COMSOL Multiphysics – 3D OPA Model

The full featured design for the CMOS printed chip, which the OPA is a part of, consists of hundreds of Silicon-Nitride waveguides, numerous optical input and output ports, dozens of prototype test structures, and a network of aluminum traces and heaters as seen in Figure 1.2. Two model versions of the OPA had been devised to reduce the disparity between the smallest and largest elements. The first was a fully featured 3D phase shifter including the ends of the surface traces for power and ground. The function of retaining all structural features of the OPA in this single phase shifter 3D model was to better model the heat transfer across the base of the trench as well as along the outer walls. This model was centered on one phase shifter shelf with equal halves of trench space on each side so the model could be tiled indefinitely to represent an accurately dimensioned array of any size. This ensured that all the fundamental dimensions, input values, and boundary conditions remained consistent across all sets of simulations. The detailed model also extended vertically down to the bottom of the to-scale silicon wafer. While Figure 3.1 shows the detailed model with inaccurate proportions for clarity, Figure 3.3 is the model of three phase shifters to-scale.

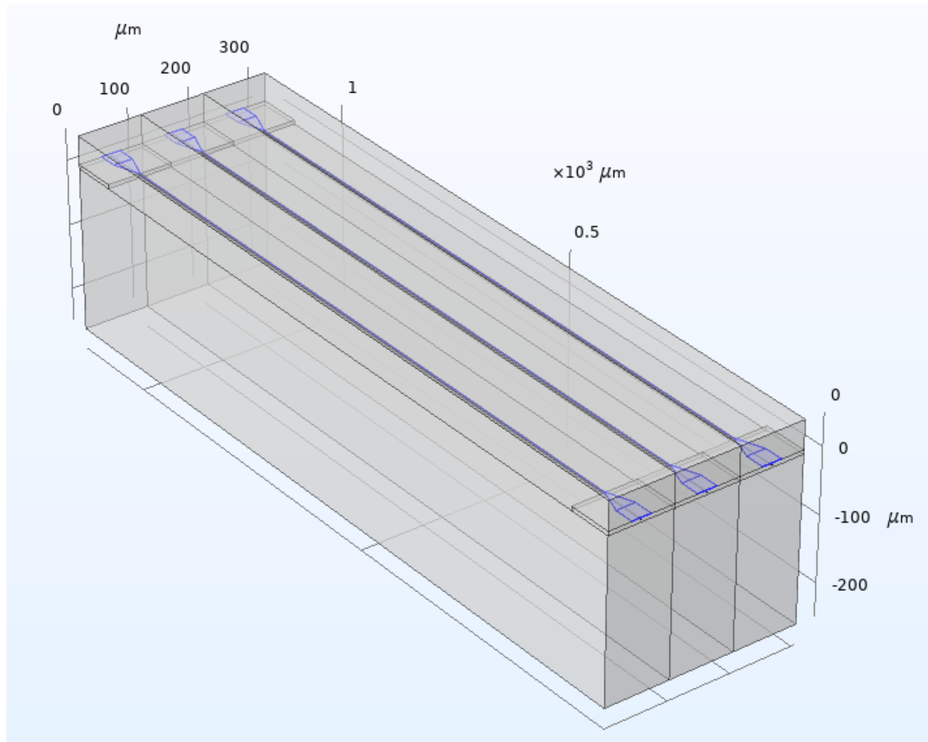

Figure 3.3: Initial COMSOL Model – Three full featured OPA phase shifters in parallel.

The fully featured approach to resolving the detailed model involved using COMSOL's Multiphysics module to couple both the Electrical Circuits and Heat Transfer modules. This was an effort to gain a broader understanding of the temperature gradient while not overloading the finite-element-method solver. Tiling the detailed model one hundred times to represent the entire array was feasible given the increased magnitude of complexity, however modelling the entire integration stage at this detail level exceeded our ability to resolve the simulation. The results of the fully featured model were used as partial validation to those of the second, lower detail, 3D model. The simpler model focuses on the macro thermal environment of the entire chip and its integration PCB stage. All the structures on the OPA were represented by a uniform heat flux boundary as defined by equations in Chapter 2. This geometric shortcut allowed the to-scale model to employ the appropriate use of substitute homogeneous material definitions as defined in Table 2.1 for simplified volumes better approximating the actual thermal behavior. The reduction in

complexity allowed us to simulate within a reasonable timeframe while also maintaining a relative level of structural accuracy.

The 3D OPA model as seen in Figure 3.4 is comprised of the to-scale silicon wafer and the full print layer surrounding the OPA, which is highlighted in blue. The large domain under it is the PCB integration stage required for the experimental testing phase. Its design is expanded upon in Chapter 4. This integration stage is included in the models as it represents a non-negligible material heatsink in the system.

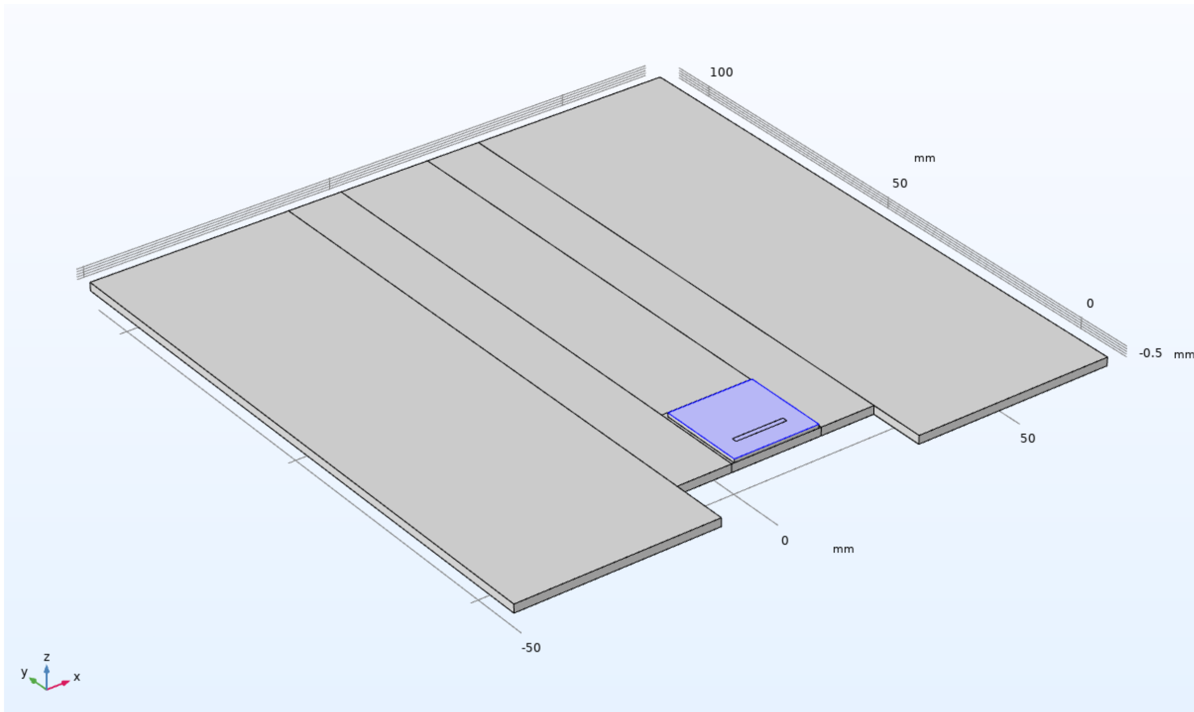

Figure 3.4: COMSOL 3D OPA Model

The 3D OPA does not contain the air trenches present in the OPA design, in lieu of employing a uniform power input boundary. This means that all simulation results for this model are of an OPA system devoid of the benefit of the primary thermal mitigation strategy. Which when compared to simulation results that do employ the air trenches, communicate the efficacy and necessity of the OPA design. To resolve the thermal environment within the model, an

appropriate mesh of nodes and vertices must be overlaid as a foundation for the finite-element solver, as seen in Figure 3.5.

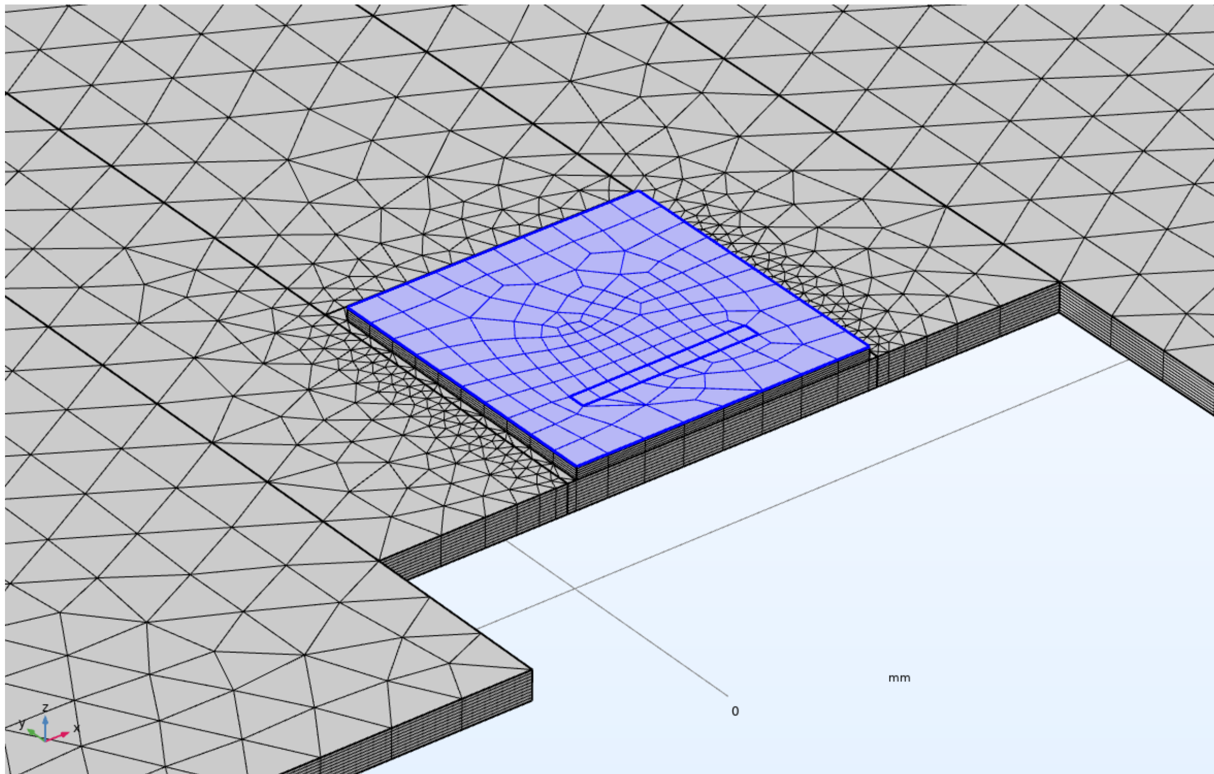

Figure 3.5: COMSOL 3D OPA Model – FEM mesh

The accuracy of the thermal environment in the 3D model can only be used as a comparison to a full featured design of the OPA. Said comparisons are recorded and prove the efficacy and necessity of the air trenches in the design but cannot accurately model the thermal crosstalk between phase shifters. The data sets being recorded from the simple model for both the 33% and 100% max power cases are comprised of the following:

- Steady-state temperature distribution of the vertical center of the OPA down through to the bottom of the PCB integration stage, against a range of temperatures at the ideal control boundary as seen in Figure 3.2.
- Temperature of the center waveguide position over time against a range of ideal control temperature boundaries.

- Temperature of the center waveguide and center floor positions over time against no control.

3.3 COMSOL Multiphysics – 2D OPA Cross-Section

A complete 3D model of the OPA was not computationally viable, and a modest 3D model of the entire system could not represent the accuracy of the thermal environment in the OPA. Where both previous models struggled, the solution was found in the middle. A 2D cross-sectional model provides the material and dimensional accuracy present in the detailed model, while also being as computationally effective as the simple model. The 2D OPA model as seen in Figure 3.6 is comprised of all 100 phase shifter elements to-scale and builds from the elements present in the previous models, including the silicon wafer and the integration PCB phase.

Figure 3.6: COMSOL 2D OPA Model - Phase shifters to-scale

The Out-of-Plane Thickness feature in COMSOL allows us to simulate the 2D slice of the OPA as if it were a complete 3D model without the same computational load. Each entity thus is defined with an Out-of-Plane thickness equivalent to its total depth. The only domain that is incapable of being represented by the Out-of-Plane thickness feature is the FR4 behind the region of copper plugs underneath the Silicon wafer. This incompatible 3D feature was remedied by increasing the Out-of-Plane thickness of that region beyond its original dimensions to account for the missing block of FR4.

Using the same Heat Transfer module present in the Simple OPA model, the 2D model functions as a direct comparison of the 3D OPA model, to prove and measure the efficacy of the passive air trenches under the same ideal or zero control cases.

Additionally, the 2D model can be used to simulate the effective thermal crosstalk across phase shifters, effectively comparing thermal distributions between any range of powered or unpowered heaters. The model was designed such that each phase heater can be independently toggled on or off at their maximum power input of 50mW. The experimental OPA is limited to powering a maximum of 33 out of its 100 phase shifters as seen in Figure 3.7, as the broken phase shifters were permanently inactive.

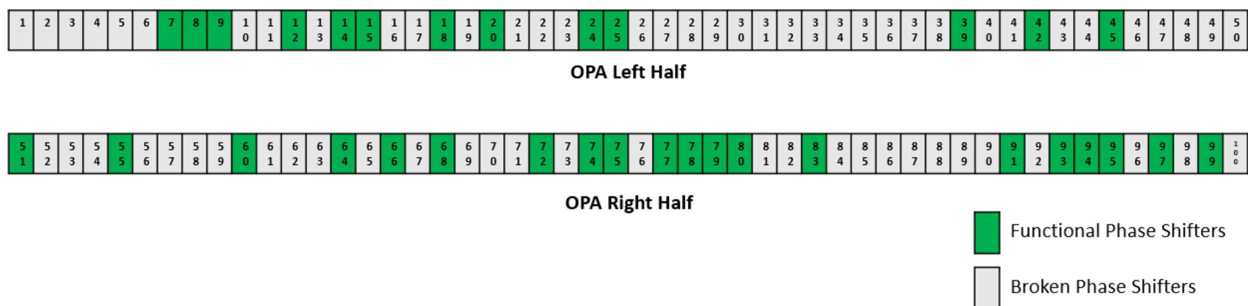

Figure 3.7: Total available active phase shifters for the experimental OPA.

Given the arrangement of active and inactive phase shifters in the 33% max power case, it is understood that the resultant thermal environment generated would not be perfectly symmetrical.

This in combination with the fact that the exact center of the OPA falls in between two phase shifters means that our center coordinates for comparison between the Simple OPA model and the experimental results must be shifted 51.1um to be centered on the next closest active phase shifter, phase shifter #51.

As a comparison to, and more exhaustively than the 3D OPA model, the data sets recorded from this model for both the 33% and 100% max power cases are comprised of the following:

- Steady-state temperature distribution of the vertical center (waveguide #51) of the OPA down through to the bottom of the PCB integration stage, against a range of temperatures at the ideal control boundary as seen in Figure 3.2.
- Steady-state temperature distribution across the horizontal plane of the OPA waveguide layer against a range of temperatures at the ideal control boundary.
- Steady-state temperatures of a set of several waveguides (inactive) as various increments of active adjacent phase shifters are toggled on (active), against a range of temperatures at the ideal control boundary.
- Temperature of the center waveguide (#51) position over time against a range of ideal control temperature boundaries.
- Temperature of the center waveguide (#51) and center floor positions over time against no control.

3.4 Simulation Results

The data exporting features of COMSOL Multiphysics allowed for all simulation data sets to be imported into MATLAB to be reorganized into suitable plots and to allow for further investigations of trends. This involved both direct comparison between the two major states of the OPA at 33% and 100% power and resolving lines of best fit with respect to the simulated setpoint levels for

further analysis in Chapter 4 and 5. Simulations included are that of steady-state analysis and time dependent studies. Additionally, the thermal crosstalk relationship is established as a function of active to inactive phase shifters.

3.4.1 Steady-state Analysis

The initial suite of simulations was performed under steady-state parameters, for the purpose of confirming both the assumptions made by the University of Toronto team and determining the benchmarks for maximum operational input [42]. Both the 3D and 2D model were run to solve the system physics to its steady-state point. The maximum power input for the models is 50mW for each phase shifter, for a total of 5W of power. While the 3D model has its total power input over the collective surface area of the OPA on the homogeneous layer, the 2D model has its power input defined for each independently controllable phase heater. The simple model has the 33% and 100% power cases defined as 1.66W and 5W of power input respectively. The 2D model has both cases respective of the number of active phase shifters as defined by Figure 3.7. All stationary simulations were run with respect to a defined temperature boundary on the underside of the integration PCB. This boundary represents an ideal control case, and each simulation case was investigated for multiple temperatures to compare the effect of setpoints to performance. Ambient temperature for all simulations was set at 300K and the chosen setpoint levels were in steps of 10 degrees Kelvin from ambient.

The first set of simulations was to understand the difference in temperature distribution through the vertical layer height of the OPA, Silicon wafer, and integration PCB. Figure 3.8 defines the change in temperature of the system from the bottom of the PCB up to the top of the OPA relative to the setpoint.

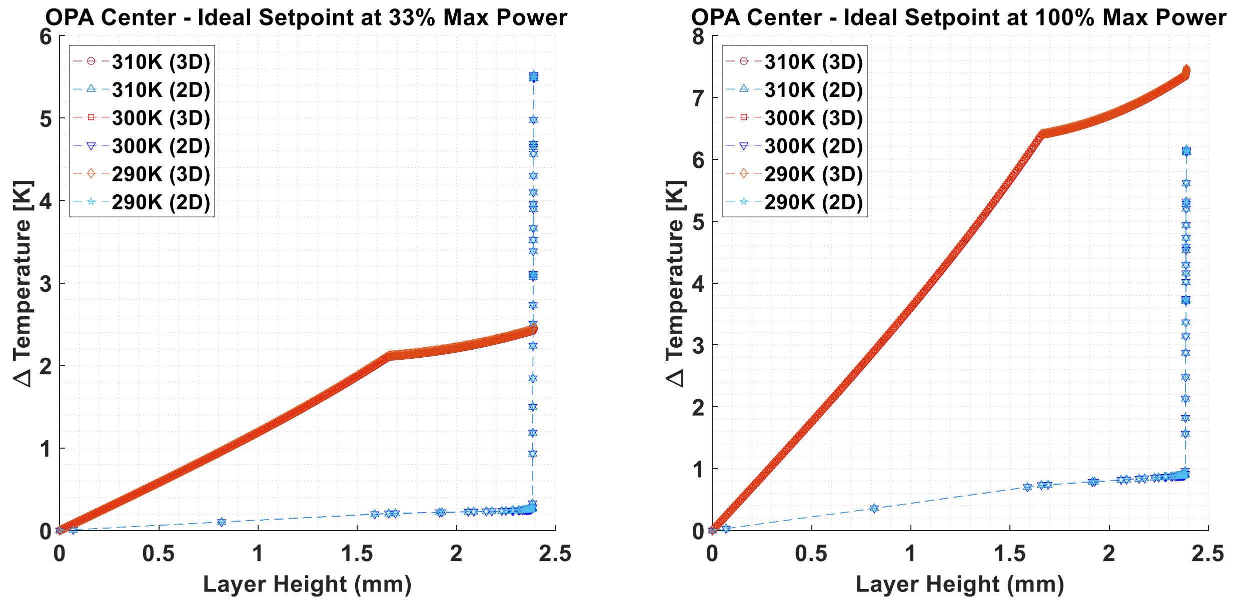

Figure 3.8: Change in temperature through the OPA center layer with respect to ideal control setpoints.

The most critical observation is the significant difference in temperatures through each of the three layers of the OPA. The 3D model lacks the passive thermal mitigation benefit of the air trenches present in the 2D model. The OPA layer is the top 6.51um of the model, and the 2D model makes clear that in both cases most of the heat generated is focused within this region where the phase shifters are present. The amount of energy present in the wafer and PCB layers in the 3D model indicates more available energy for thermal crosstalk between phase shifters. Additionally, the wide range of maximum temperature values at the peak of the OPA in the simple model shows that without air trenches, there is a great lack of thermal stability necessary for optimal phase shifter operation. Additionally, the data indicates that a higher setpoint will result in a smaller temperature deviation. However, this appears to happen regardless of the constant ambient air environment of 300K, which remains consistent across all simulations, indicating that the ambient temperature is far less impactful on the system than an ideal control temperature boundary.

For the 2D model results, it is important to note that in both cases, Waveguide 51 is considered active, and therefore the difference in maximum temperatures observed at different

points in the waveguide layer is an effect of thermal crosstalk that will be investigated in Chapter 3.4.3. The waveguide layer is the horizontal plane of which thermal crosstalk is observed, about 3.1um below the surface of the OPA, parallel to that of all the waveguide structures as dictated previously in Figure 3.2.

The next dataset output was exclusive to the 2D model as it relies on the accurately dimensioned phase shifters to be present. The 2D model can be used to simulate the effective thermal crosstalk across phase shifters, effectively comparing thermal distributions between any range of powered or unpowered heaters. The model was designed such that each phase heater can be independently toggled on or off at their maximum power input of 50mW. Figure 3.9 shows the distribution of the 33 available phase shifters on the first test OPA chip compared to an ideal 100 available phase shifters. By taking the temperature profile across the horizontal waveguide plane, a unique perspective can be presented on the thermal environment at the points in the OPA which matter for optical output performance.

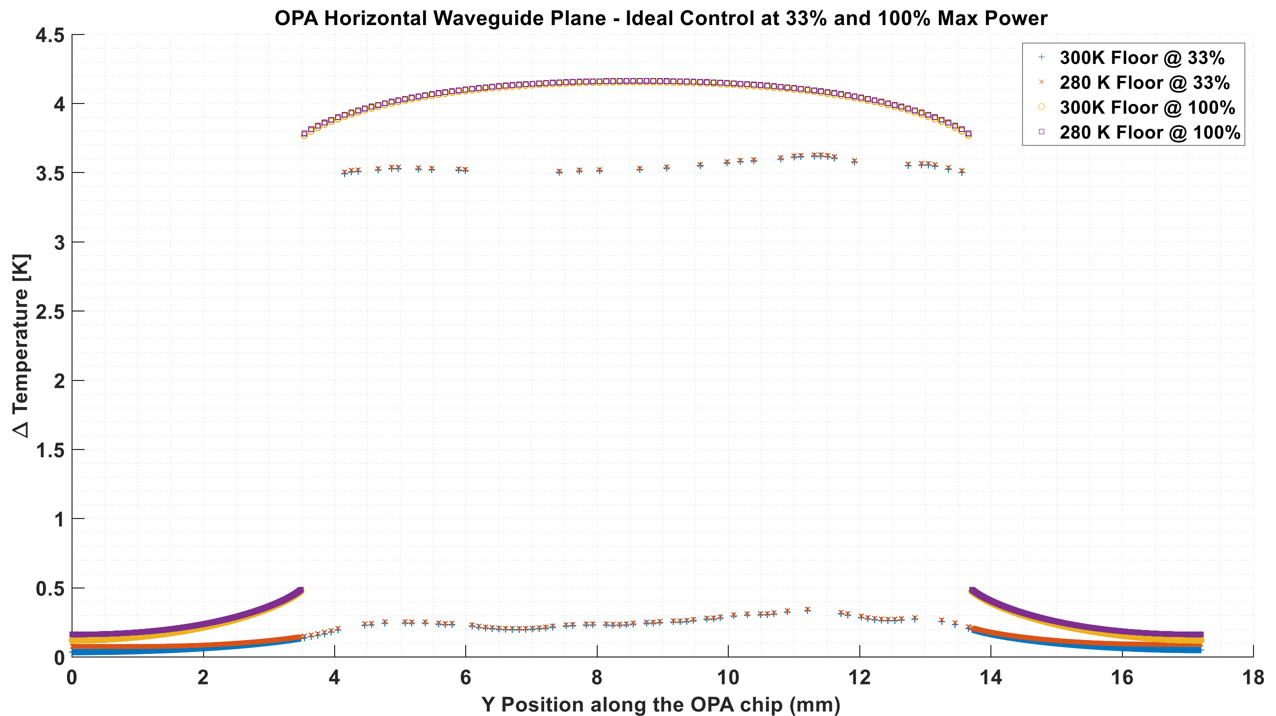

Figure 3.9: COMSOL 2D OPA Model temperature distribution across center long edge of OPA with ideal thermal control.

Once more it is clear that the difference in setpoint does not correspond to significantly reduced thermal crosstalk.

3.4.2 Time Dependent Studies

The time dependent studies on both models were an investigation into the temperature rise time of the OPA in both ideal control and no control scenarios. The ideal control scenarios involved step function power input to the OPA phase shifters while maintaining a uniform temperature boundary on the base of the integration PCB. By measuring the center of the OPA at the waveguide level, the actual phase change can be derived based on the active time and the temperature of the boundary layer. Figure 3.10 illustrates the change in temperature on the waveguide as step input power is applied to the center phase shifter.

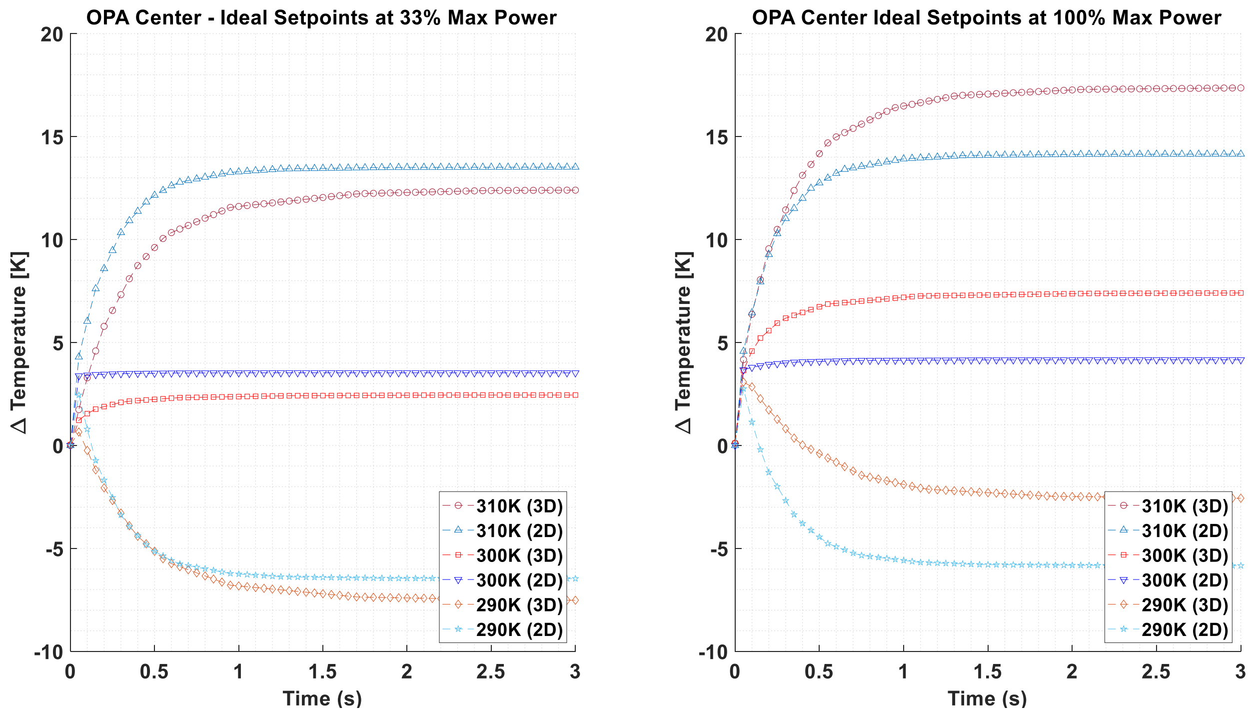

Figure 3.10: COMSOL OPA temperature difference from 300K ambient given a step input at various setpoint boundaries for a single waveguide.

Both power cases show similar rise times for the OPA respectively, with the 3D model settling after 2.75 seconds and the 2D model settling after 1.5 seconds. Additionally, with respect to their boundary temperatures, the temperature differences the waveguide settles at with respect to ambient is far greater on the 3D model, with a $\Delta T = 2.48$ at 33% power and a $\Delta T = 7.44$ at 100% power. The 2D model by comparison has a temperature difference of $\Delta T = 3.53$ at 33% power and a $\Delta T = 4.16$ at 100% power (also seen in Figure 3.9), implying again that the presence of the passive air trenches on the OPA corresponds to faster rise times and greater stability. With respect to the internal relationships between power and temperature, the 2D model is the platform of focus for continued simulations.

While the relationships between the waveguides and the setpoint boundary are informative with respect to the inner relationship of the OPA, that information informs the optical control design side more than that of the thermal control. The characterization of the thermal control design requires quantifying how much heat arriving at the setpoint boundary will need to be accounted for to maintain a constant setpoint. The 2D model was run at both power quantities for extended periods of time while the setpoint boundary was changed to a surface-to-ambient boundary. These results are seen in Figure 3.11.

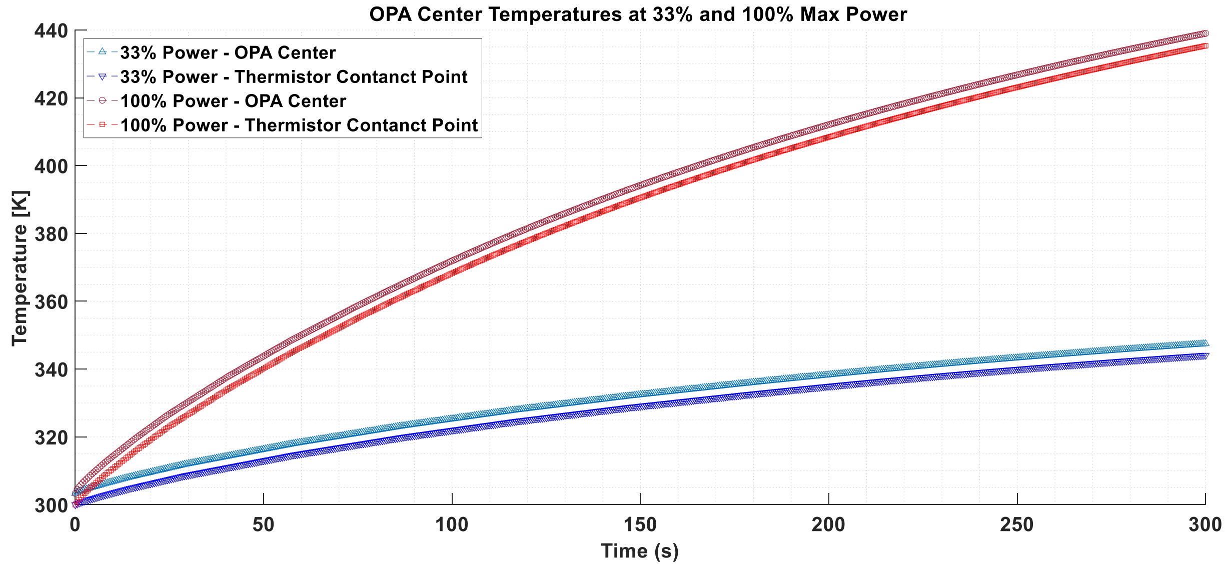

Figure 3.11: COMSOL 2D OPA Model Temperature response at 33% and 100% power with no thermal control.

The phase shifters were designed to induce a phase change of π at a temperature difference of just under 50 degrees. After three hundred seconds at 33% power the waveguide reaches a temperature difference of 44 degrees, indicating that low power operation is enough to induce the necessary phase changes for OPA operation. The exception to this feature is that as a requirement to the optical control, a robustness of phasing up to 2π was necessary. This would allow the OPA to exhibit a phase change range of -π to π rather than 0 to π. A 2π phase change range implies that a 100-degree temperature difference must be mitigated by the thermal control. The 100% power case after three hundred seconds exceeds the 100-degree margin, which corresponds to approximately 70% of the present maximum limits. The 2D model does not include the TEC or heatsink entities and therefore the conduction present regardless of the Seeback effect does affect the simulation results, causing the resultant values to be higher than their experimental counterparts which is investigated further in Chapter 4.

3.4.3 Thermal Crosstalk Analysis

Ultimately, the datasets for both the steady-state and time dependent simulations indicate that the passive structures are not enough to warrant operation without thermal control. Even the best case of ideal thermal control still results in a level of thermal crosstalk between phase shifters that will need to be accounted for in the operational steering control code through methods including but not limited to lookup tables. These values can be derived from the 2D model by measuring the change in temperature against ambient for each phase shifter individually as select phase shifters are toggled on and off. Figure 3.12 illustrates the difference in temperatures of a row of phase shifters adjacent to one that is active at the maximum 50mW of power.

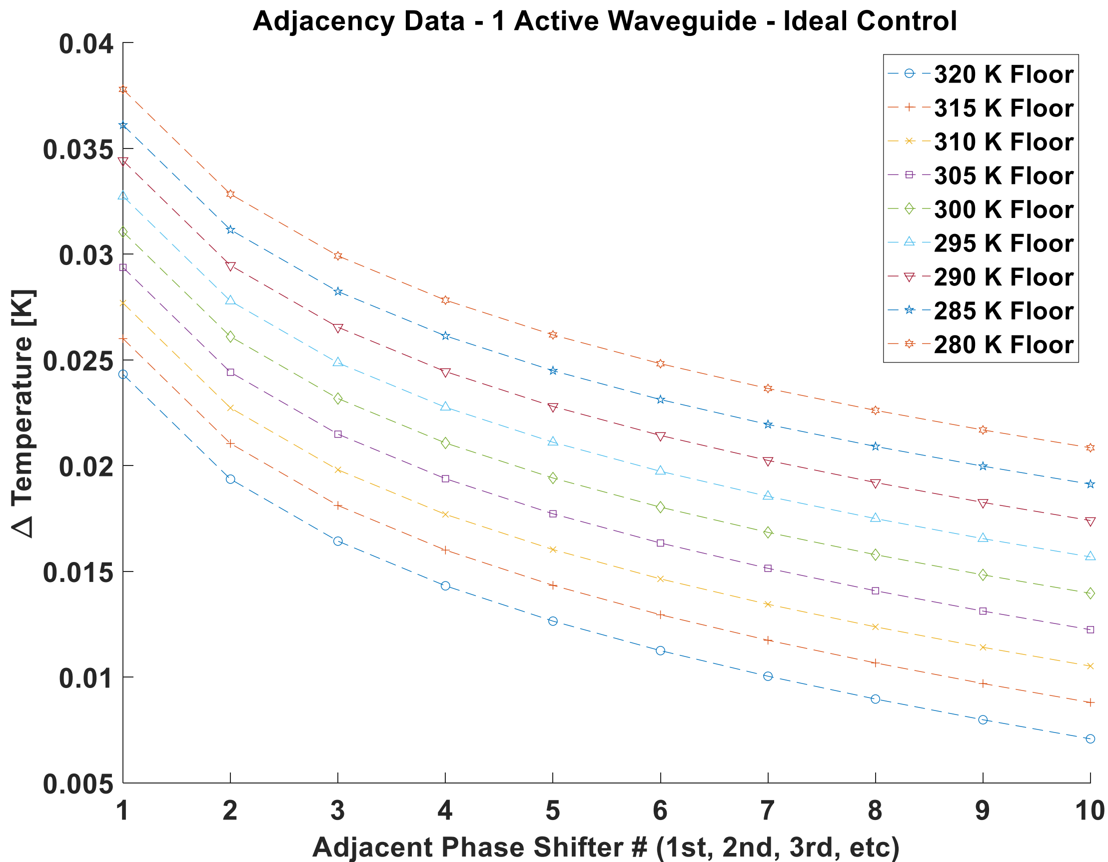

Figure 3.12: COMSOL 2D OPA Temperature difference for inactive phase shifters adjacent to an active phase shifter.

In this case, the setpoint boundary at the integration PCB does play a meaningful factor into the proportional amount of thermal crosstalk. The setpoint boundary chosen for use in all future testing is 20 degrees Celsius, or 293 K. Given this boundary, a curve of best fit is applied in Figure 3.13 and can be used to quantify overall thermal crosstalk for each phase shifter individually given the known active and inactive patterns.

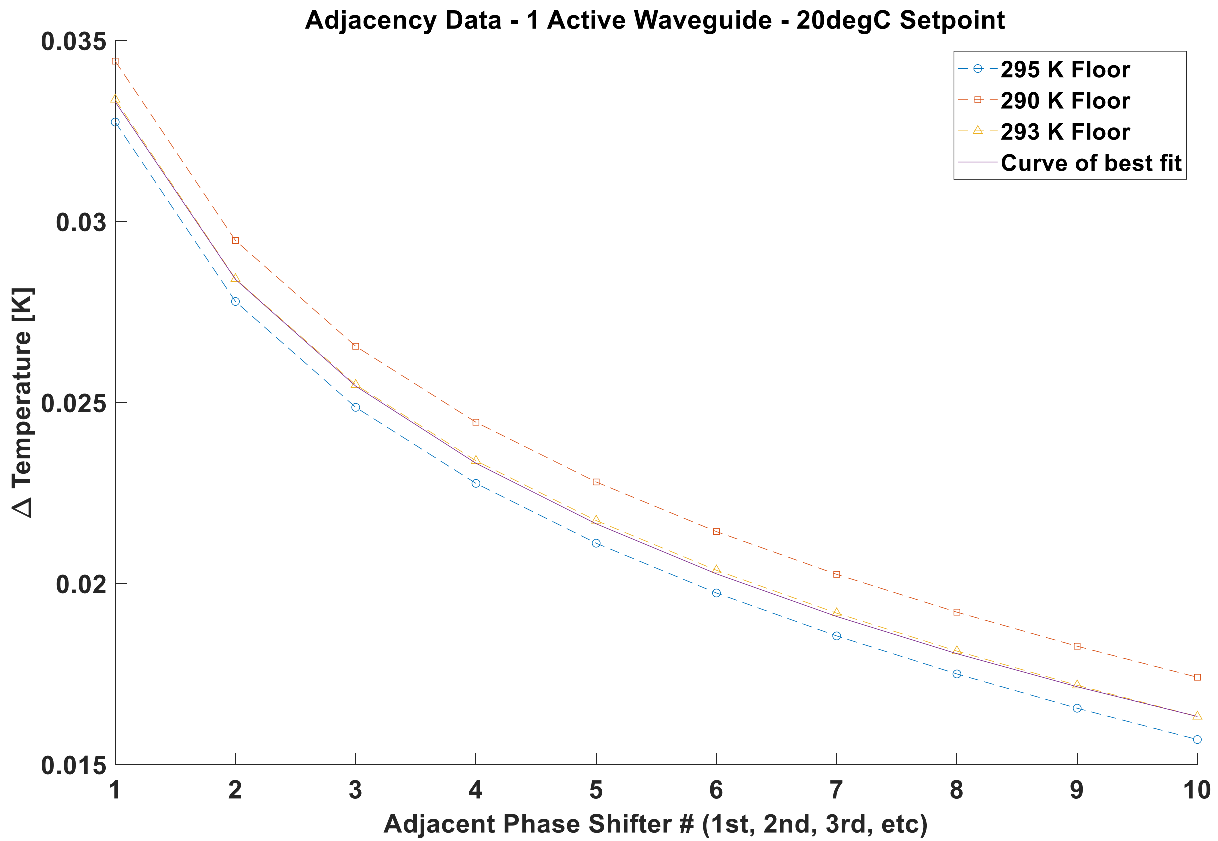

Figure 3.13: COMSOL 2D OPA Crosstalk Adjacency at a 20-degree Celsius setpoint.

The thermal crosstalk relationship can be defined for each phase shifter location as a function of how many and how far away each active phase shifter is. Equation 3.1 is a power function where x is the number of positions away from an active phase shifter, and $T_{Adj}(x)$ is the change in temperature.

$$T_{Adj}(x) = -0.14x^{0.051} + 0.17 \quad \textbf{(3.1)}$$

In the cases of multiple active phase shifters, the total thermal crosstalk is a summation of equation 3.1 for each active position. This relationship holds regardless of whether the position being measured is active or not as the thermal crosstalk is additive. Several suites of simulation data were taken to confirm the validity of the summation relationship. In the case of 50 active phase shifters all to one side, the simulated results of the additive thermal crosstalk were 0.43 degrees and the calculated value 0.54 degrees. The case of 99 active phase shifters (50 on one side, 49 on the other) results in an additive thermal crosstalk of 0.85 degrees simulated or 1.08 degrees calculated. The calculated value is 28% higher than the simulated results, implying that the system is not additive, and there is a crosstalk decay proportional to that same percentage that should be accounted for in future optimization calculations.

No further experiment data related to crosstalk between the individual phase shifter elements was collected given the hardware limitation. More details of the experimental setup are provided in Chapter 4.

Chapter 4
Interface, Characterization, and Validation

In order to test a chip-scale microphotonics device, an interface is required to match the input and output ports of the device to the general-purpose laboratory equipment. The hardware interface must account for the difference in size of said ports which are many orders of magnitude larger than that of the OPA. It must also act as a platform to be mounted, secured, and aligned to the testing instrumentation available in the laboratory environment. A printed circuit board (PCB) was designed to facilitate this interfacing work. This ensures that the OPA chip remains fixed and that both electrical and optical signals are simultaneously yet independently functional.

The characterization of the OPA chip is divided into two categories: characterization of open loop control and characterization of closed loop control. The characterization with control will be covered in Chapter 5. Each of these tests involves sweeping the active elements across the benchmarks set within their ranges of operating power to observe the step responses and stability of the systems. Resultant data plots from the thermistor sensors are overlayed and compared against the simulated data to determine experimental error, confirmation of initial design assumptions, and feedback for refining the accuracy and response times of the PID controller. The controller operating in tandem with the thermal data input as a part of the active system allows for immediate improvement of the response and magnitude of heat distribution.

4.1 PCB Design

The on-chip OPA, which is a research prototype and not a commercial product, lacks any conventional packaging. To run, control, and observe the OPA, a PCB stage was required to interface between the chip and the conventional electronics, optics, and sensors. The PCB design

was conducted in Altium Designer, for thorough control over custom trace and component dimensioning. The OPA Carrier PCB was designed and manufactured at the same time as the on-chip OPA proper. It accommodates all 148 bond pads for the OPA and routes all one hundred phase shifters to common grounds in groups of at most sixteen, as dictated by the existing external power amplification control circuit at Honeywell. Said circuitry also dictated the use of eight full size thirty-four pin vertical connectors to accommodate each phase shifter power-ground pair and the additional test structures on-chip. The bond pads for electrical connections between the chip and the board were dimensioned to manufacturer specifications to allow for Electroless Nickel Electroless Palladium Immersion Gold (ENEPIG) compatible wire bonding to bridge the vertical displacement between the two. The layout of the traces and ground plane groups are visible in Figure 4.1.

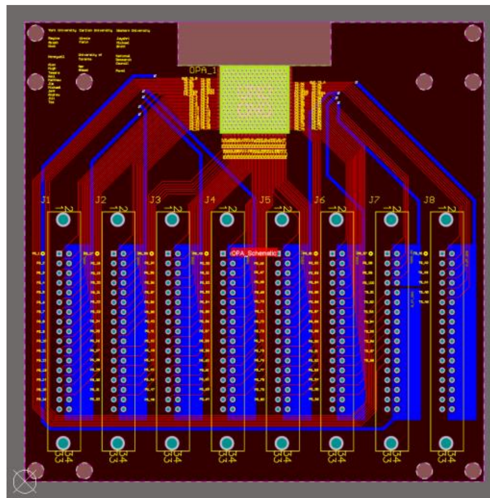

Figure 4.1: OPA Carrier PCB layout diagram.

Mounting holes for 8-32 bolts were designed in accordance with known 1/2” and 1” breadboard grids for mounting stability. The rectangular cut-out along the top side of the board was done to ensure the taper fiber array as the optical inputs could be aligned flush with the chip within just a few microns. This was to ensure strong optical coupling and zero obstructions. The

large central pad where the OPA is soldered is mirrored on the opposite side of the board, and both pads are connected by a series of plugged copper vias for increasing thermal conductivity [43], [44]. The arrangement of the vias was done in a hex array that maximizes the volume of copper and thermal conductivity [45]. The direct underside of the chip is where the TEC of similar dimensions is mounted, acting as a uniform thermal sink to actively stabilize the thermal performance of the OPA.

As a function of the polishing step in the manufacturing process of the square OPA chip, the chip's final dimensions could fall anywhere between 18.2 and 17.2 millimeters. The main pad sizing and bond pad spacing on the board were arranged to accommodate this range. The length of the square TEC by comparison is 19.4 millimeters, such that centering the device on the PCB pad would ensure a more uniform thermal distribution across the bottom of the OPA.

Given the necessity to run both the optical control and the thermal control simultaneously in the testing process, a clear hardware layout was necessary for debugging and nominal operation. Figure 4.2 shows how the instrumentation is integrated and how both the phase control loop and the thermal control loop can operate as well as be characterized independently of each other.

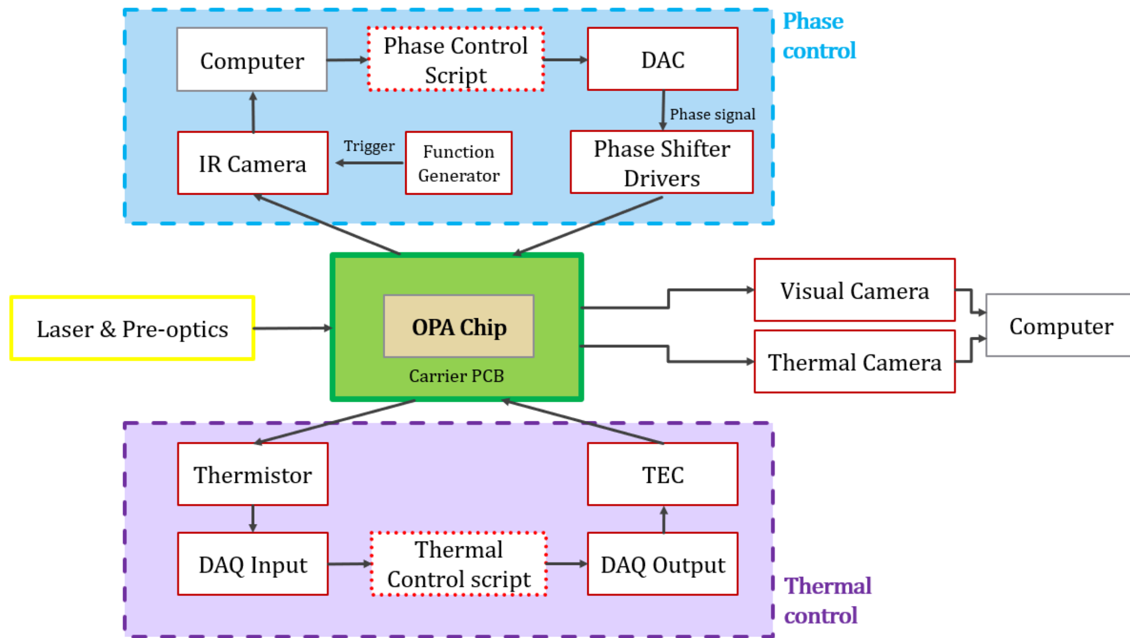

Figure 4.2: Instrument integration flow chart.

The OPA Carrier Board had been manufactured and the on-chip OPAs were integrated. Each PCB integration board measures 1.66mm in total thickness, seen in Figure 4.3.

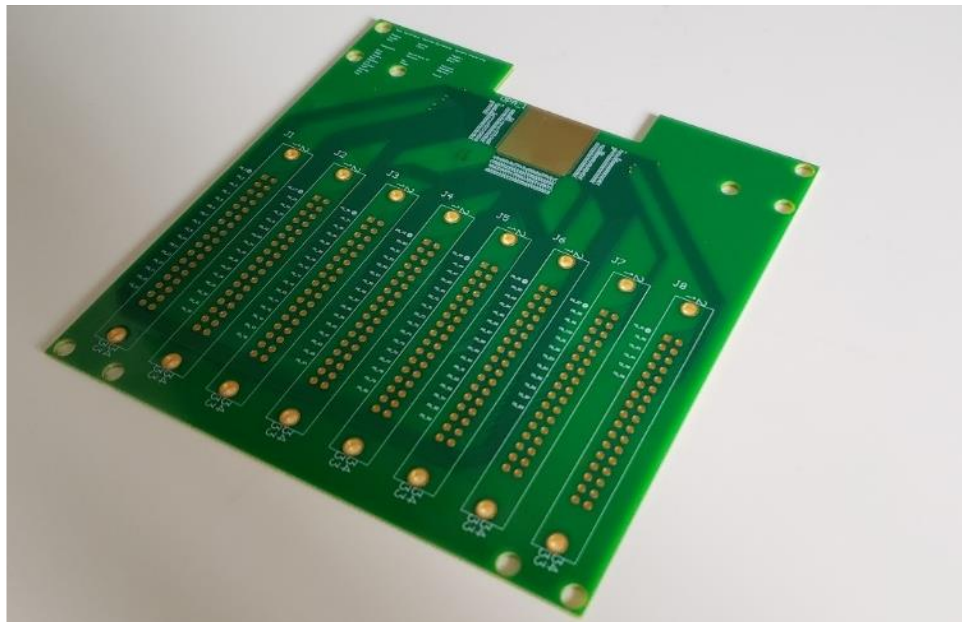

Figure 4.3: OPA Carrier board (OPA chip not present).

The board design sub-objectives are divided into two categories. The first category is the operational and testing requirements determined by the HOOPA platform layout and the architecture of the existing external power amplification control circuit. By verifying the operational capability of the elements in the system from the initial board design, we can determine how to effectively integrate them onto the board in a more complete manner for the next carrier board design. These requirements include the following:

- To interface with the pre-defined connector components to the existing external power amplification control circuit. This acts as a verification precursor to integrating the control circuit onto the board, and eventually integrating onto the chip.
- To interface with the unobstructed optical input couplers so they may be aligned right up to the edge of the chip. This determines how effectively an input coupler package can be integrated onto the board.
- To include ENEPIG coating as to facilitate the wire bonding process, as the chip in its current state is not package integrated.
- To accommodate the possible variation in size of the chip as its edges are to be polished in the manufacturing process, resulting in an unknown final dimension. The design choice to facilitate this will communicate the possible trade-offs in performance relative to a rigid chip size constraint.
- To interface with mounting architecture of existing testing platforms used by the various university teams.

The second category is the design of the material connection between the chip on the surface of the board and the external thermal control system on the underside of the board. This material connection currently involves connecting the pads on both sides of the board with as much

thermally conductive material as possible in a uniform manner. The conventional manufacturing approach taken was to maximize the volume of copper between the two pads by laying out an array of copper plugged through-holes in a hex pattern [45]. The extent to which the dimensions of this solution is tailored is at the discretion of the technical capabilities of the PCB manufacturer.

Finally, the PCB is to provide the ability to affix an external thermal control system and allow the material connection between said external thermal control system and the HOOPA chip to be as thermally conductive as possible. The design and material choices for the PCB are limited to the capabilities of present standard PCB manufacturing techniques. Ideally, given time constraints, the results obtained in the testing phases will allow for a second board design that further integrates the system level components surrounding the HOOPA chip.

4.2 Test Setup

A test setup in a laboratory setting was used to validate the reliability and accuracy of both the PCB design and the previous simulation suite in Chapter 3. Over the course of the project, there have been two laboratory setups where the hardware was run, and data was acquired. The initial setup was assembled in the Electronics Lab at Honeywell and is seen in Figure 4.4. The setup was relatively rudimentary as it did not have a viable heatsink available. The second setup was done at York University and allowed for the full hardware assembly. Given the scope and objectives of the greater OPA project previously decided by the Honeywell team, they provided and acquired much of the necessary hardware for initial optical tests and thermal tests. The OPA was mounted and aligned to the optical hardware as seen in Figure 4.5.

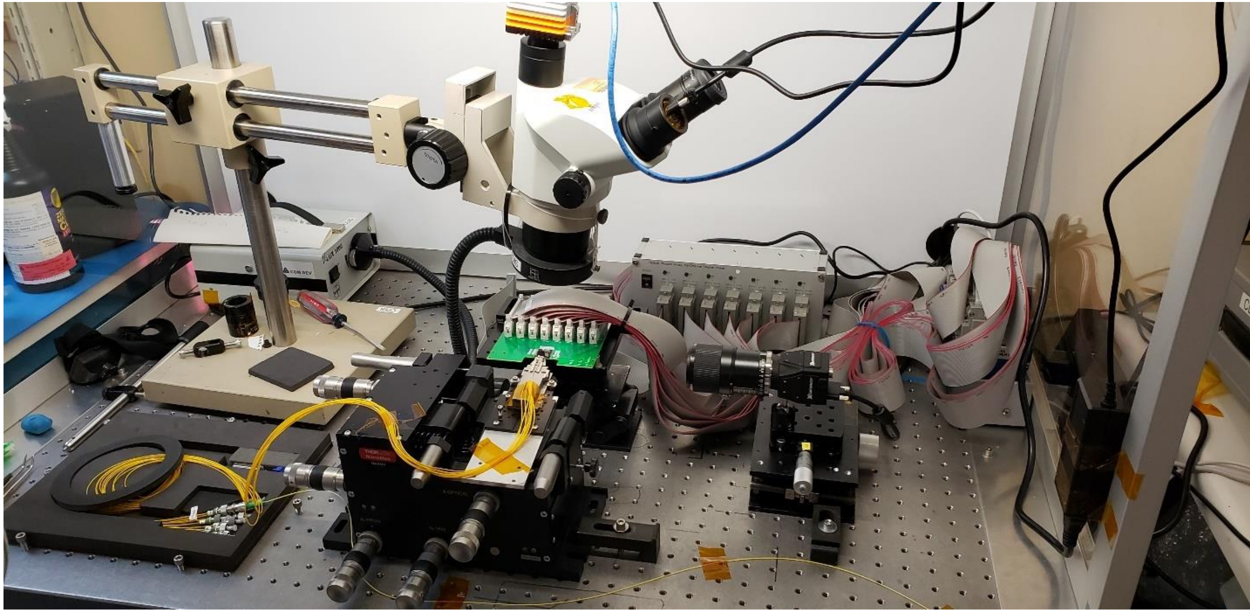

Figure 4.4: OPA Honeywell laboratory test setup.

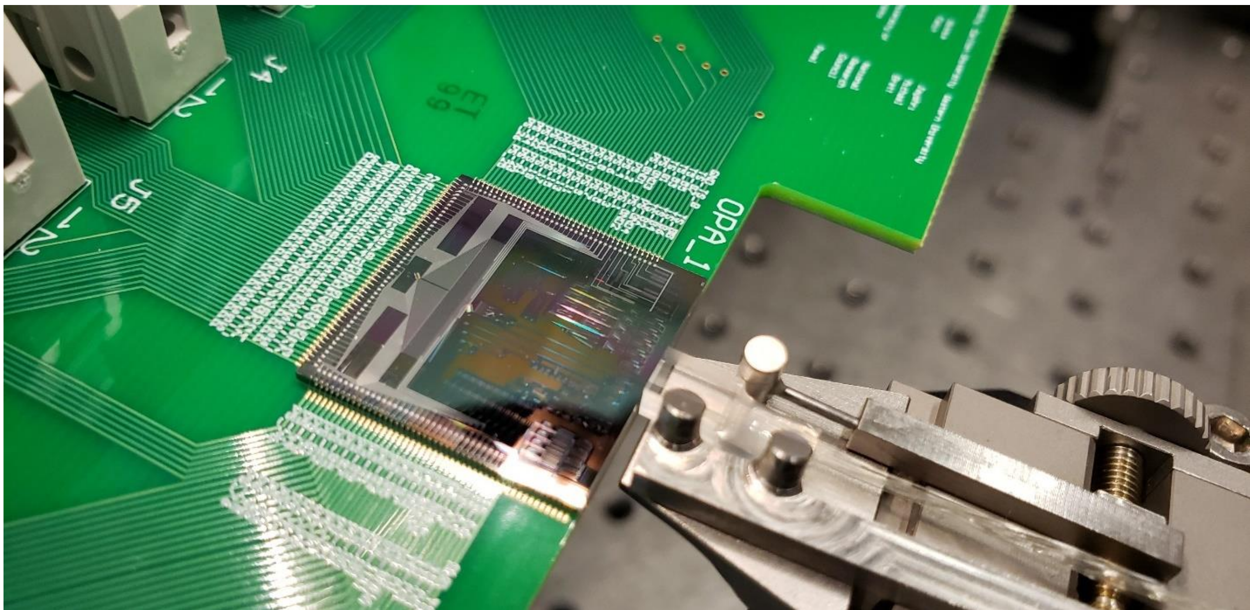

Figure 4.5: The on-ship OPA fully integrated an optically coupled.

With the aid of the orientation mounts, the tapered fiber array, which is used as the system's optical input, can be coupled mere microns from the edge of the chip. Figure 4.5 also shows the etching and deposit layers of the OPA in the reflected light. The hardware defined in the thermal control loop in Figure 4.2 is not present in these photos, as it was critical that the phase control

hardware was characterized first. The characterization of the thermal response of the system would fail if the OPA phase shifters could not be powered up. Bonding the thermal control to the PCB before being confident in the integrity of the OPA itself would have resulted in further complications. The use of an infrared camera and thermistors as data collection and sensor inputs while the OPA is in operation was the safest approach in this phase of the testing.

The OPA design facilitated many optical input and output ports, the majority of them for isolated test structures. The OPA requires only one optical input, and the 100-emitter dual ring grating structure acts as a unified singular output. The complete optical hardware setup included a tapered fiber array and signal laser generator for the input, and a lens assembly with camera mounts for output data collection and processing. The complete hardware layout for the thermal control is illustrated in Figure 4.6. The individual functions of each component are listed in Table 4.2.

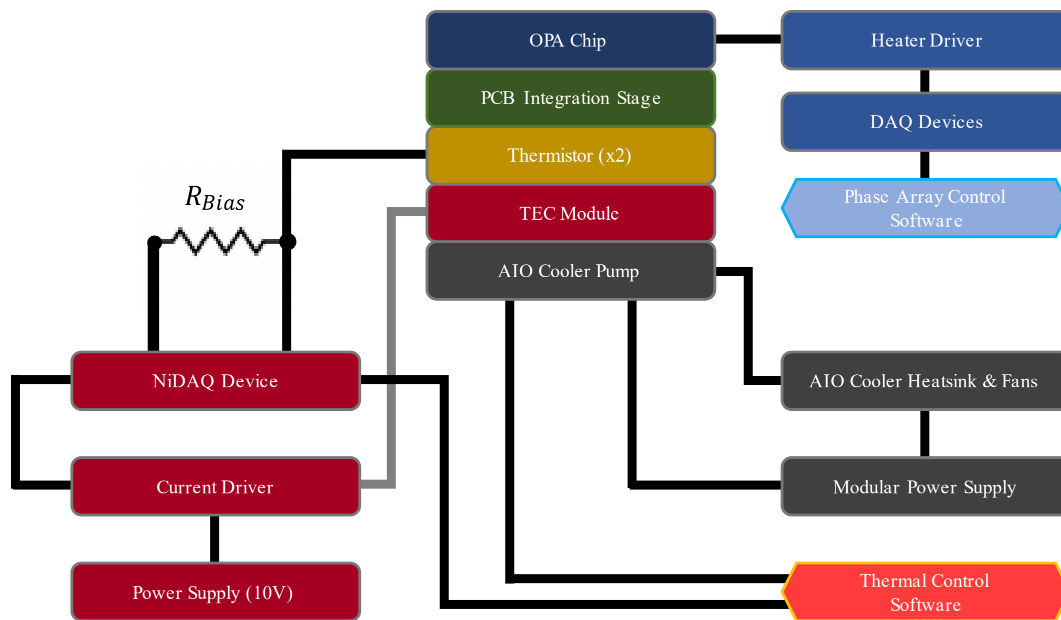

Figure 4.6: Complete hardware layout for experimental thermal tests.

Table 2: Hardware Component List

Component	Use-Case	Objectives
XYZ Alignment Stages (Thorlabs)	Hardware alignment	Precise angular alignment of tapered fiber array to OPA optical input port.
National Instruments cDAQ-9178 and 9264	OPA power and control	Controlled Input Voltage as defined by Control Scripts
Heater Circuit (Honeywell Custom Design)	OPA power and control	Regulates power output for OPA control based on voltage input.
Keysight E3631A Triple Output DC Power Supply	Power	Supply constant 10V to power the Current driver
Current Driver (Honeywell Custom Design)	Power converter.	Regulates current output for the TEC based on voltage input.
National Instruments DAQ 6212	Thermal Control	Regulates digital signals and I/O voltages to control the current driver and read the thermistors.
Laird HiTemp ET Series ET2.3-49-F1-1919-TA-RT-W6 Thermo-electric Cooler	Thermal Actuator	Generates a temperature gradient between its plates proportional to a driven current.
Arroyo 1600-10K Thermistor / Thorlabs TH10K Thermistor	Feedback Sensor	Variable resistor with respect to temperature changes.

iCUE H150i RGB PRO XT Liquid CPU Cooler	Heatsink	Desktop liquid CPU cooler utilized as an effective heatsink.
Corsair RM850 Modular Power Supply	Power	Supplies constant power to the AIO Cooler Module.
Arroyo Instruments 5240 TECSource, 4A/7V	PID Control	Optional device for real-time temperature display and TEC control.
33% Power Board (Board#4)	OPA Board	OPA Chip with 33/100 unbroken phase shifters
98% Power Board (Board#1)	OPA Board	OPA Chip with 98/100 unbroken phase shifter structures
Laptop 1	OPA power and control	Runs the MATLAB and LabView software for OPA phase heater control.
Laptop 2	Thermal Control	Runs the MATLAB/Simulink software for thermal control and Python script for AIO control.

In the first version of the fabricated device, there was significant damage to the phase shifter structures from the fabrication process. The only two OPA chips available for testing had several phase shifters it could not power. The 33% OPA had 33 out of 100 viable phase shifters and was used as the initial testing platform for verifying procedures and initial tests as previously detailed in Figure 3.7. The 98% OPA had only two broken phase shifters and was used for the full power tests.

The complete thermal hardware setup including the AIO cooler was assembled in the York labs following the initial test suite from Honeywell and is seen in Figure 4.7.

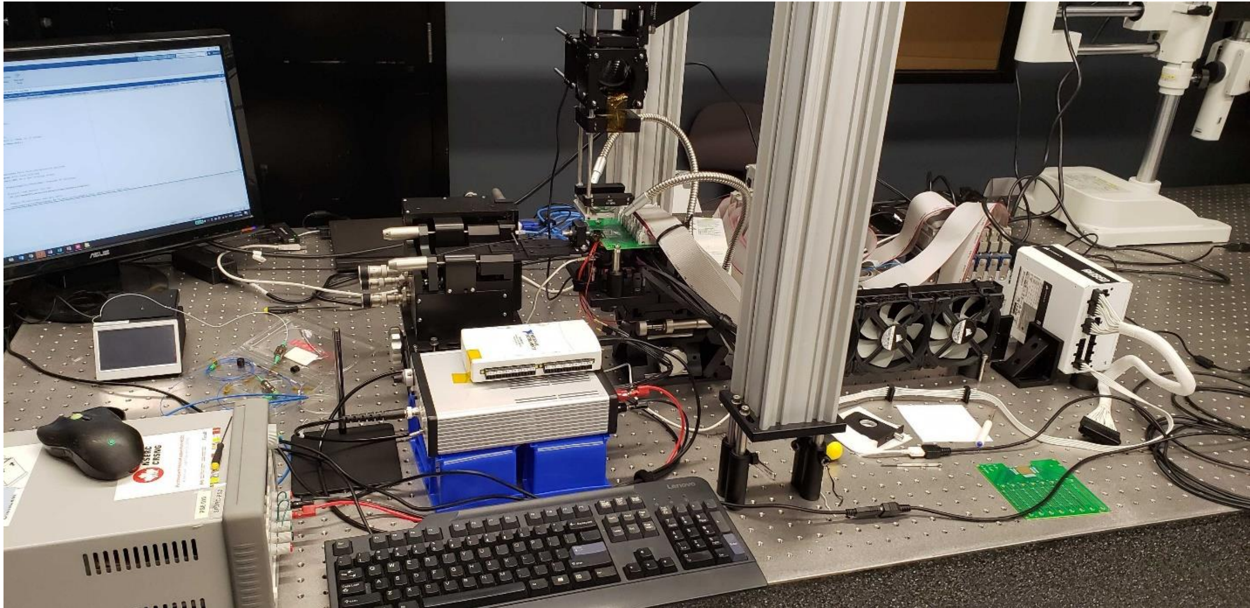

Figure 4.7: Complete thermal and optical hardware setup for experimental testing of York.

Full testing required the use of two laptops. The first was running a MATLAB-LabView data-to-analog-converter (DAC) control code for the input power to the hundred phase shifters that make up the OPA. This code was written by a team member in York University for the optical testing. This OPA control code would set the power levels and thus the thermal output of each phase shifter independently. The second laptop was running the MATLAB-Simulink thermal control code as well as a python script for the AIO cooler in Chapter 4.2.3.

4.2.1 Thermistor Setup

To function as an effective feedback sensor, two thermistors had to be bonded using highly conductive thermal epoxy between the bottom side of the PCB and the top (cold) surface of the TEC and were centered under the location of the OPA proper. The location of the thermistors therefore communicated the effective temperature boundary between these points. There were two thermistors bonded so that thermal data could be read by the NIDAQ for thermal control purposes

as well as a prebuilt temperature controller, an Arroyo TEC Source module, if available [46]. The other reason two were used was for redundancy in the testing configuration.

The thermistors' internal resistance would vary based on present temperature as discussed previously in Chapter 2.3.8. The NIDAQ 6212 only registers voltage measurements. To actively read and convert the resistance value, a voltage divider was used as per Figure 4.8.

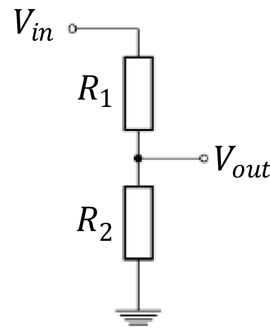

Figure 4.8: Voltage divider for thermistor (R_2) reading.

In the figure, R_2 is a bias resistor for the thermistor to be compared against, where R_1 is the thermistor. The measured voltage difference is between the 5V (Vin) input and the recorded output as defined below in Equations 4.1 and 4.2.

$$V_{out} = \frac{R_2}{R_1 + R_2} V_{in} \tag{4.1}$$

$$R_{Thermistor} = R_{Bias}\left(\frac{V_{in}}{V_{out}} - 1\right) = 10000\left(\frac{5V}{Analog\ output} - 1\right) \tag{4.2}$$

Equation 4.2 is used in conjunction with equation 2.15 to complete the relationship between active temperature and recorded voltage response and are utilized in the MATLAB function listed in Appendix B.

4.2.2 Thermo-electric Cooler Module

Operating under the Thermoelectric effect as discussed in Chapter 2.3.8, the TEC device generates a temperature difference between its cold and hot surfaces when a current is applied. The model chosen to thermally stabilize the OPA chip is a commercial off-the-shelf (COTS) Peltier device which could generate a temperature difference of over 50 degrees between its two surfaces [29]. In addition, the model was of similar length and width dimensions to that of the OPA chip. The TEC is a square 19.4mm so it could match the form factor of the OPA chip with regards to both current experimental integration and future packaging integration. The initial design documentation for the OPA photonics structures by the Honeywell team indicated that a temperature change of 49.7 degrees off ambient would result in a complete pi phase shift. The joule heating resistors that make up the phase shifters as well as the passive thermal mitigation structures on the OPA were sized to generate this temperature change. It was expected that the temperature profile would be hotter than the initial calculations implied due to unaccounted complex thermal relationships in the overall structure. However, the experimental results as seen below in section 4.2 indicate that those values were underestimated. Thankfully, the TEC model selected is rated to displace up to almost 100 degrees given sufficient current and under ideal conditions [29].

The performance of the TEC with respect to its datasheet in Figure 4.9 indicate that at the maximum available current draw of 1.5A from the current driver, 6W of power can be drawn from the cold-side and 12W of power would be dissipated from the hot side. This means that for however hot the OPA gets with respect to the setpoint, a robust heatsink fixture is required to prevent the reflow of heat back up into the OPA both during and between operations.

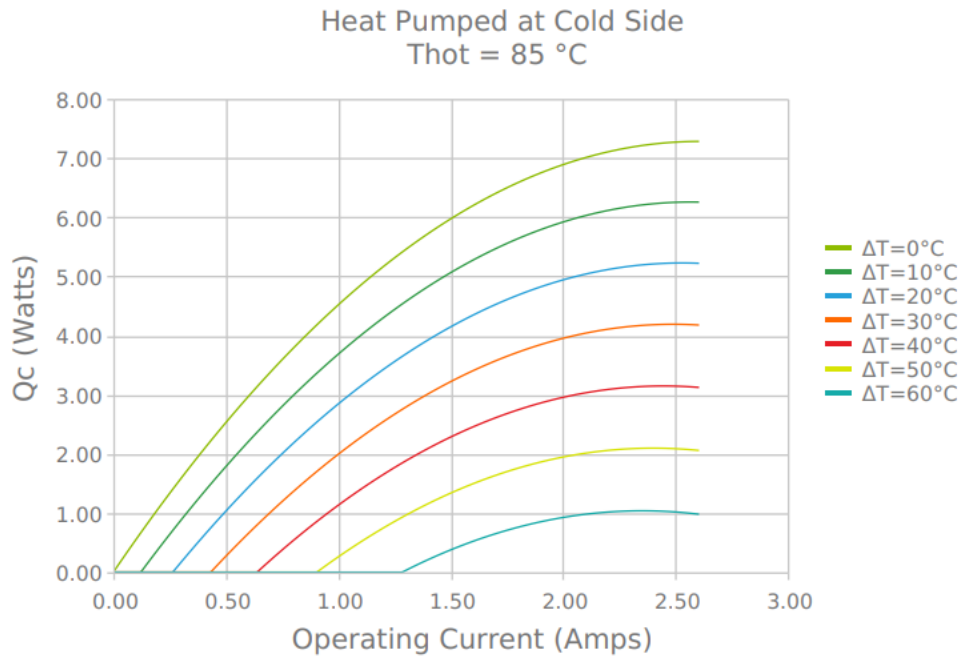

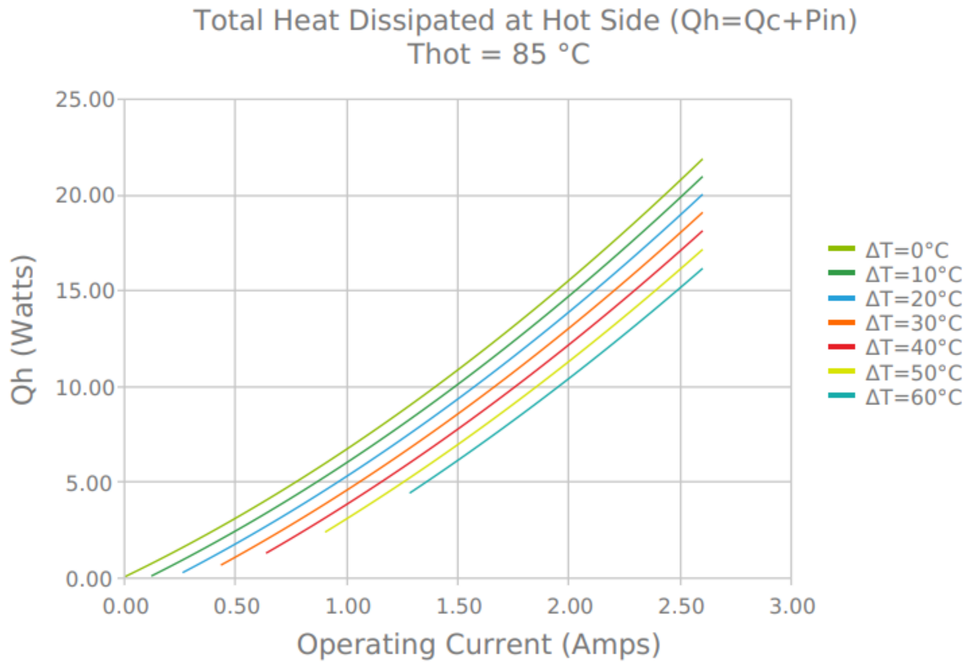

Figure 4.9: Electrical and thermal performance of TEC module according to datasheet [29].

4.2.3 Heatsink Setup

After the initial tests the hardware setup was moved to the York labs. A heatsink was required for consistent operating temperature. Due to the fragility of the surface structures of the OPA, the wire bonds to the PCB and the tapered fiber optical input, a conventional forced air convection heatsink near the OPA was not viable due to their vibrational output. The initial heatsink tests in Figure 4.10 used only natural convection. The heatsink used at the was an aluminum finned CPU heatsink 9x7x3cm in size.

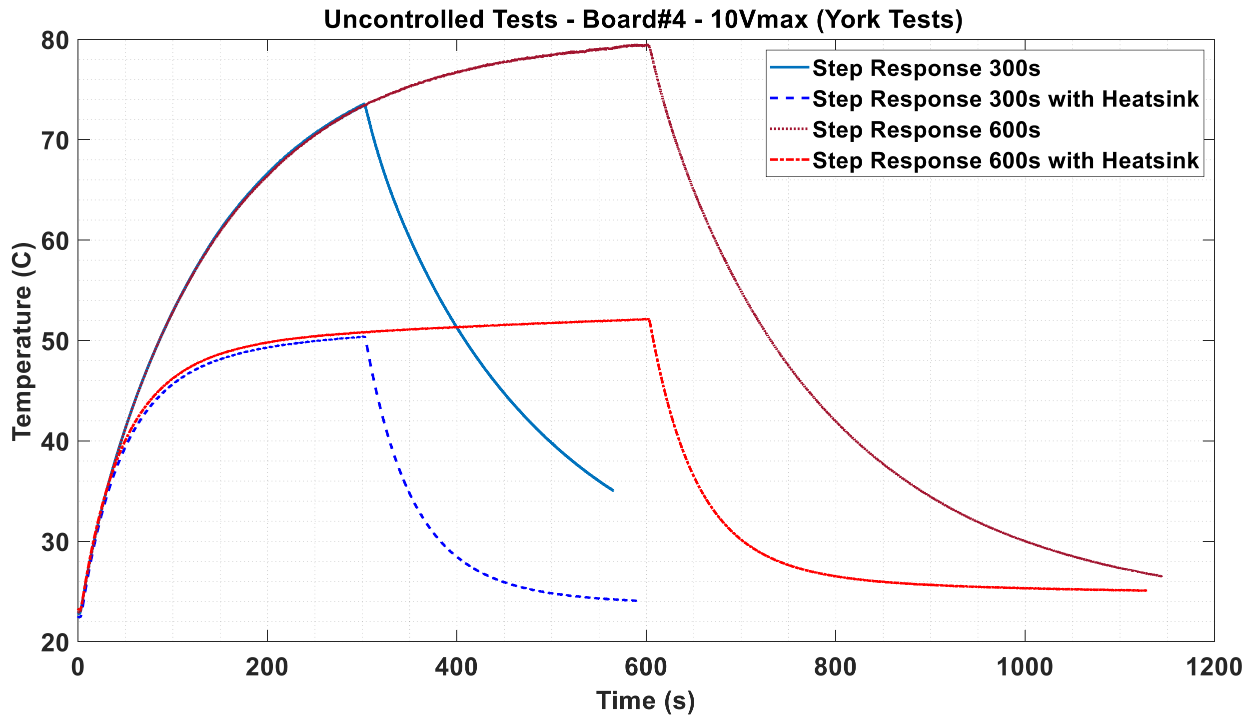

Figure 4.10: Temperature response without heatsink versus with a heatsink present.

While it was evident that the heatsink was effective, the static aluminum finned heatsink alone cannot stabilize the temperature while the OPA is under operation where the voltages through each phase shifter would be changing constantly. Additional tests proved that the heatsink could not stabilize temperature at the necessary levels on natural convection alone and would result in heat flowing back from the heatsink into the OPA. To correct this while maintaining no forced

air convection around the OPA, an all-in-one (AIO) CPU cooler was utilized. AIO Coolers use a liquid pump heatsink which transfers the heat to a nearby heatsink block that is cooled by several fans. The separation between the pump and the heatsink was enough that turbulence around the OPA was negligible. The model selected was the Corsair iCUE H150i RBG Pro XT, which featured a 397mm x 120mm x 27mm radiator heatsink with three 120mm x 120mm x 25mm fans. The system required the use of a modular power supply but could be connected and controlled by the same laptop running the MATLAB-Simulink thermal control code. An existing python script available from an open-source GitHub project was used to set the fan and pump speeds to their maximum and to remain constant throughout the entirety of use [47].

4.3 Open-Loop Control Tests, Experimental Setup, and Results

Each set of experiments were run to validate the benchmarks approximated by both the simulations in Chapter 3 and the previous theoretical calculations made by the other teams. The complete suite of experimental tests was done split between the Honeywell Electronics Labs and the Nanosatellite Laboratory at York due to lab availability constraints. The first phase of testing involved powering on the phase shifters in the OPA without any feedback thermal control hardware present to characterize the response. The objectives of the open-loop tests are as follows:

- To determine maximum temperature profiles of the OPA without any temperature control to establish that the chosen TEC hardware can cool it to a setpoint of 20 degrees.
- To determine the relationship between active phase shifters and OPA operating temperature.
- To determine the noise-floor of the thermistors with respect to active temperature reading.

The relationship between active phase shifters and OPA operating temperature allows for reasonable estimation of maximum power output of 100 phase shifters. It was deemed safer to not run any maximum power tests on all 100 phase shifters at once without any thermal control, in lieu of possible system damage under an unnecessarily large temperature gradient. The first set of temperature profile tests done at Honeywell were performed on the 33% OPA board, which was internally denoted as Board#4. Figure 4.11 depicts the measured temperature from the mounted thermistors on the underside of the PCB with no feedback control.

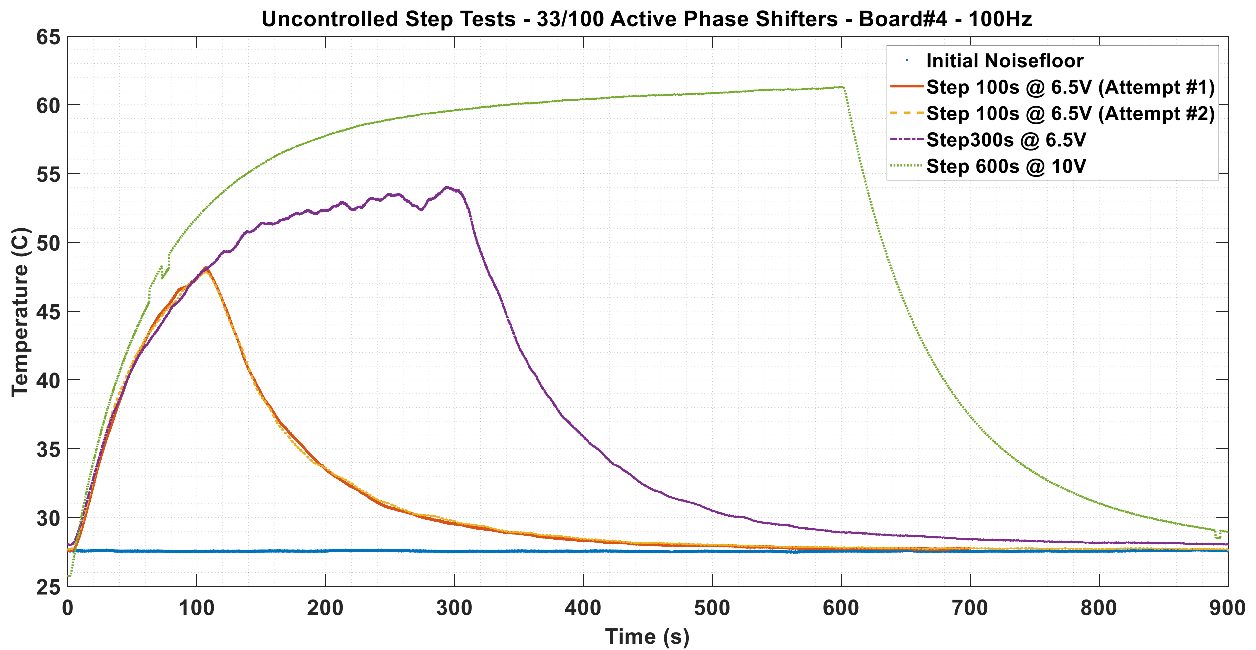

Figure 4.11: Initial thermal response step tests of 33/100 active phase shifters at 6.5V and 10V of power.

The phase shifters were powered to only 6.5V because at the time of the Honeywell tests, it was understood that was the necessary voltage to induce a complete pi phase shift by each phase shifter. The team had eventually decided that despite the 6.5V margin, the max power limit for each phase shifter would be 10V. The increase in voltage corresponded to a significant boost in temperature to the active phase shifters. The temperature difference generated under 10V for 33 active phase shifters was approximately 36 degrees after 10 minutes. Assuming a linear

relationship between active phase shifters and temperature response would put the difference at 100 active phase shifters above the limitations of the TEC, so further investigation was required. By running several step tests with increasing numbers of active phase shifters, a more accurate relationship for temperature response can be established. Since the 33 available phase shifters on the OPA were non-uniformly distributed across the array as seen previously in Figure 3.7, the incrementing groups of active phase shifters were selected to be as evenly distributed as possible, as listed in Figure 4.12.

Step Test Group	Active Phase Shifter #					
Step Response [5/33]	7, 20, 55, 75, 93					
Step Response [11/33]		8, 24, 60, 77, 94, 99				
Step Response [16/33]			9, 25, 64, 78, 95			
Step Response [22/33]				12, 18, 39, 51, 66, 74		
Step Response [27/33]					14, 42, 68, 79, 80	
Step Response [33/33]						15, 45, 72, 83, 91, 97

Figure 4.12: Incrementing active phase shifter groups.

From these groups the difference in temperature response can be seen in Figure 4.13, and the temperature relationships defined in Figure 4.14.

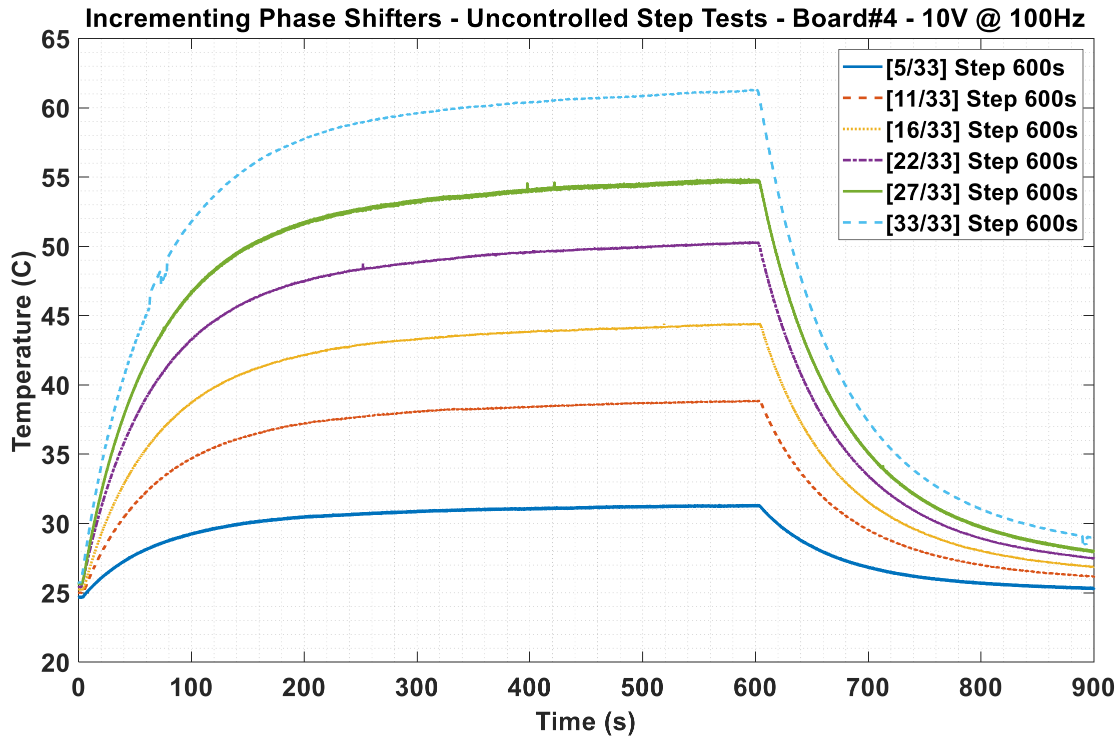

Figure 4.13: Temperature response of increasing number of active phase shifters at 10V.

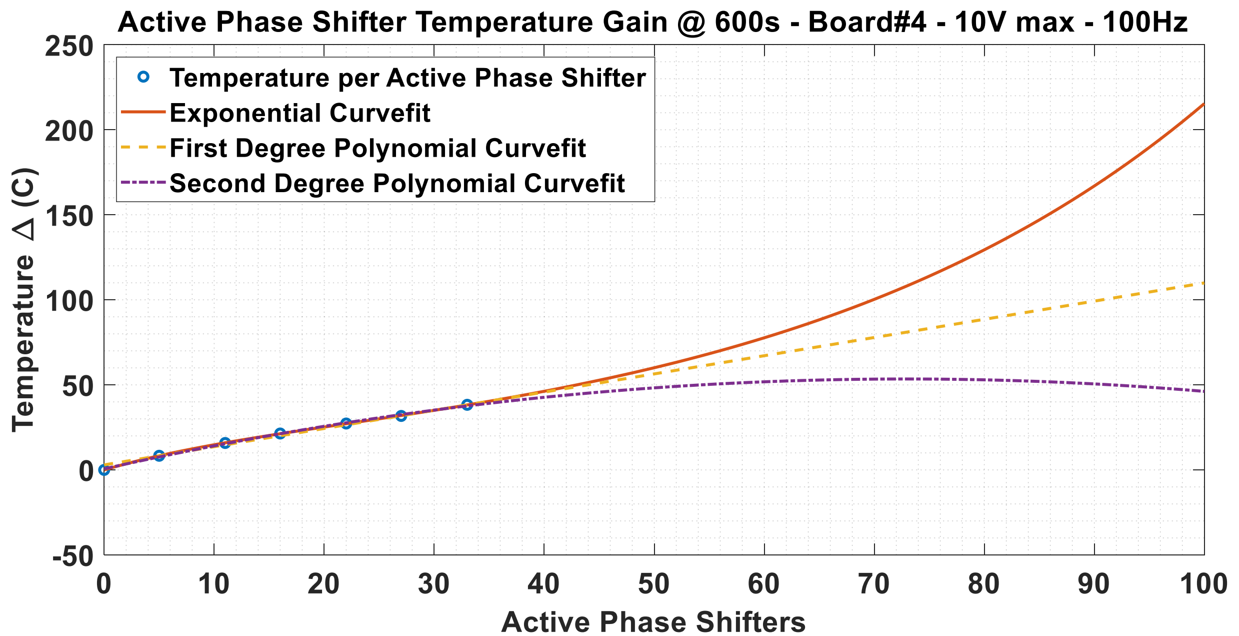

Figure 4.14: Phase shifter temperature relationships.

While the exponential fit had both better fit parameters for the coefficient of determination (R^2) and root mean squared error (RMSE), the first-degree polynomial displays a more intuitive

representation of the realistic temperature values at higher numbers of active phase shifters. This confirms that the maximum active case is beyond the regulative ability of the TEC. However, this does not disqualify the hardware due to the following factors:

- Under no circumstances during operation or testing will it be required for the OPA to operate all 100 phase shifters at 10V.
- The current driver for the TEC is limited to 1.5A of current while the TEC is rated to up to 2.5A.

The maximum edge case results in the same non-resolvable optical steering pattern that exists when all signals are phase shifted the same amount. Voltage above 6.5V results in a wrap-around effect as the phase shift has exceeded one period. This means that any resolvable operation is conducted at or under this point, where additional voltage up to 10V is effectively a buffer zone and contributes to the robustness of the system. Expected tests and operations will therefore not be expected to exceed around 70% (or 7V) of power, which is well within range of the TEC's maximum ability. This range of operation is confirmed again in Chapter 5 by long-term control tests in search of system break points.

The experimental results as seen from Figures 4.10, 4.13, and 4.14 are compared against the COMSOL simulated temperature response from Figure 3.11, and indicate that the simulated high power tests far exceeded the experimental measurements, seen in Figure 4.15.

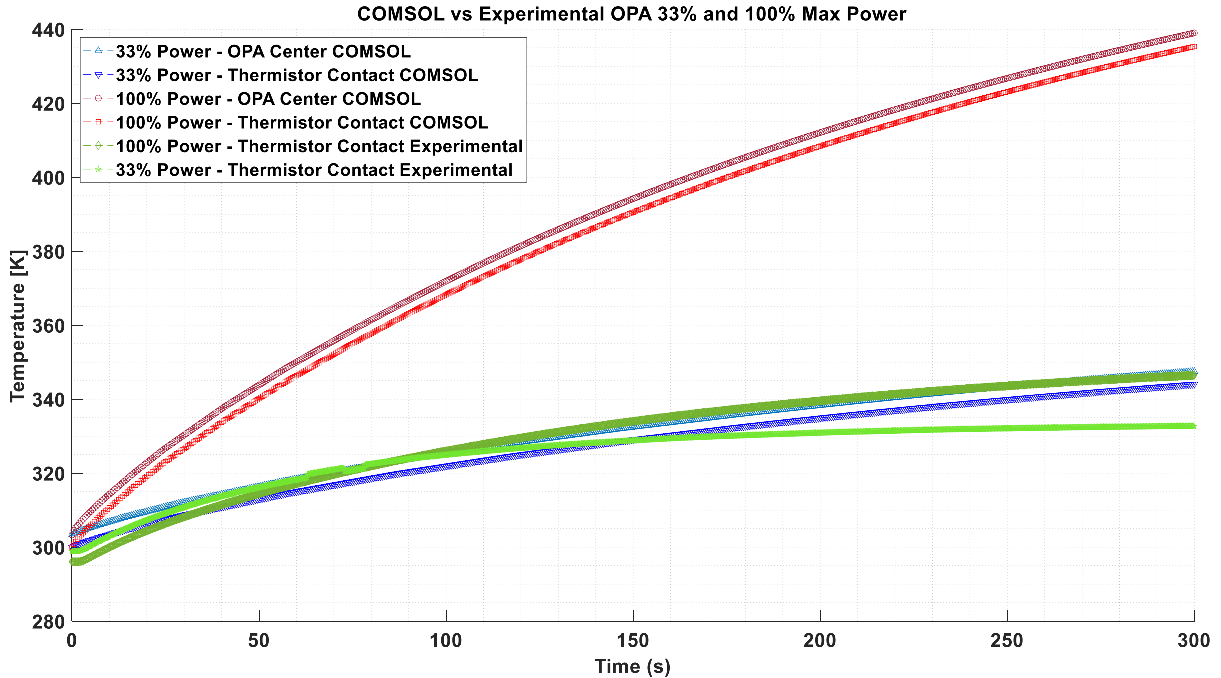

Figure 4.15: Direct comparison of temperature response between 2D COMSOL model and experimental measurements.

The slightly varied starting temperatures and the difference in ambient temperature between the simulations at 300K and the experimental tests at around 295K to 298K, still put the simulated 33% power tests within a few degrees between the 33% and 100% experimental tests. This indicates that while the initial model designs with respect to the 33% power case were accurate, the simulated OPA response at the highest power do not translate to their experimental counterparts. This is believed to be a result of several factors surrounding the limitations of the models' complexity and the inductive resistor input power approach.

The last series of tests run without any control were the noise floor measurements. The noise is a function of both the thermistor's imperfections and the method through which the NiDAQ 6212 device actively reads voltage signal measurements. Repeated observations of this phenomenon indicate that the noise is relatively consistent and contributing to approximately 0.05 degrees of variance in measurements.

Chapter 5
Closed-Loop Feedback Thermal Control

The characterization of the control software, written in MATLAB-Simulink, is divided into several categories as a response to the different generated results from the previous COMSOL Multiphysics simulations. These involve characterizing the OPA chip for optimum long-term setpoint stability and optimum settling time with respect to the magnitude of voltage drops. Each of these tests involve several sweeps of the operational benchmarks set by the TEC module to resolve the quickest settling time response as determined by both the system's power draw and the efficacy of the PID control. The ideal control setup for this system is defined to minimize settling time and steady state error when stabilizing at desired temperature levels. A NiDAQ device is used as the data acquisition hardware to support both the TEC and the temperature sensors. Most experimental testing was conducted on an OPA chip with ninety-eight out of the one hundred phase shifters intact and functional, allowing for power tests of up to a maximum of 98%. The simulated analysis of the system model was also done in MATLAB-Simulink and compared several approaches to actuator-plant modelling with respect to the experimental results in Chapter 4. These methods include attempts of input dependent gain, input dependent plants, and experimental plant averages.

5.1 Closed-Loop Control Tests, Experimental Setup, and Results

Previous successful attempts at running thermal control feedback systems using both MATLAB and Simulink have shown levels of thermal control which match expectations for settling times and overshoots [48]–[51]. The MATLAB-Simulink program designed to read and write to the NiDAQ device runs on a separate computer from the OPA phase shifter control code, as both

cannot be run on the same machine at the same time. The thermal control system was required to be completely decoupled from the phase shifter optical control code so it could be designed and operated independently. The Simulink diagram for the control code is seen in Figure 5.1 and is centered on the analog output and analog input functions for the NiDAQ device.

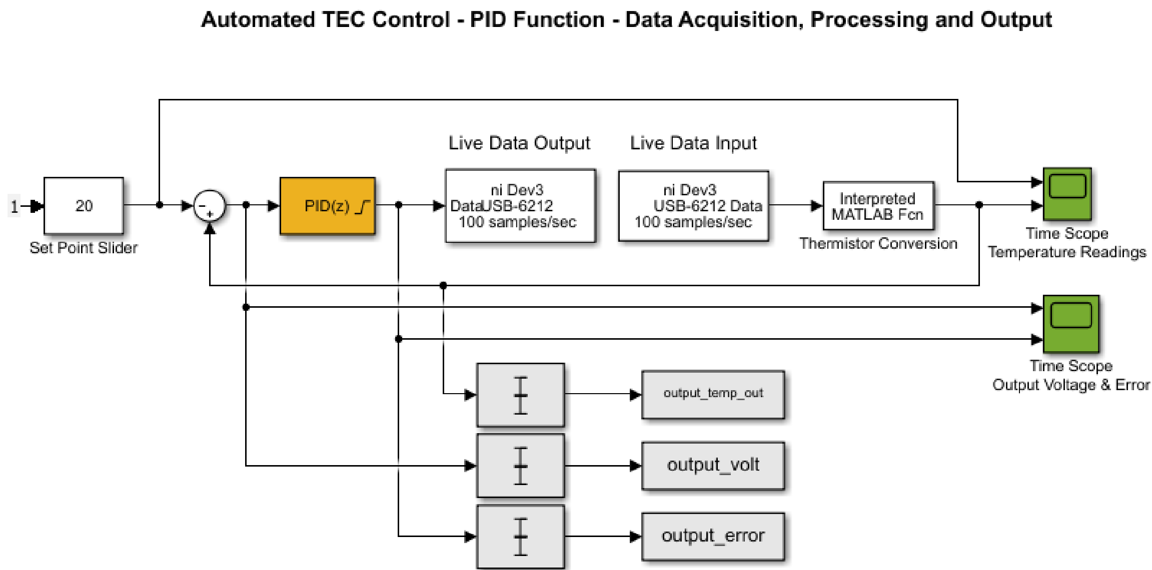

Figure 5.1: MATLAB-Simulink thermal control code diagram.

The input voltage from the thermistor voltage divider is converted to a temperature value based on the pre-established properties of the resistance-to-voltage relationship and is compared to the setpoint temperature of the system. In direct comparison to the COMSOL simulations, the ambient temperatures were less than 300K = 26.85 degrees Celsius, hovering at around 20 degrees Celsius. Initially, both setpoints were considered for control tests before greater requirements for the OPA project settled on a set 20 degrees Celsius. The error difference is then processed by the PID function block which houses the complete proportional, integral, and derivative gains and formulae. The resultant control output voltage (which is limited to 0-3V due to the current driver hardware) is then sent back to the NiDAQ to control the current driver which drives the TEC. The mean, scope, and output functions only exist to communicate visually the system's performance

in real-time as well as logging the resultant data to the MATLAB workspace for post-processing. Initial PID controller values were set using general heuristic assumptions and were refined further through the testing process with standardized methods.

5.1.1 Experimental Long-form Stability Tests

Despite the use of the incredibly robust AIO cooler, maximum power tests of 10V OPA input still resulted in temperatures beyond the setpoint as the TEC itself could not displace enough of the heat load from the OPA at the 1.5A limit. It was a requirement that the temperature control be able to keep the system at a setpoint temperature for an extended period, being on the order of hours at the very least, to account for long form optical tests. To work around this, power limits had to be set on the OPA to stay within the viable thermal control range the existing hardware could support. Given the initial PID values, several multi-hour-long experiments were run to determine the sustainable long-term stability of setpoint control at higher power levels. The times taken between initially reaching setpoint, and when the temperature exceeded the 0.1 bounds of setpoint were collected to determine the long-term viability of the system. Figure 5.2 shows how long in seconds each input power case managed to stay at setpoint temperature before exceeding it.

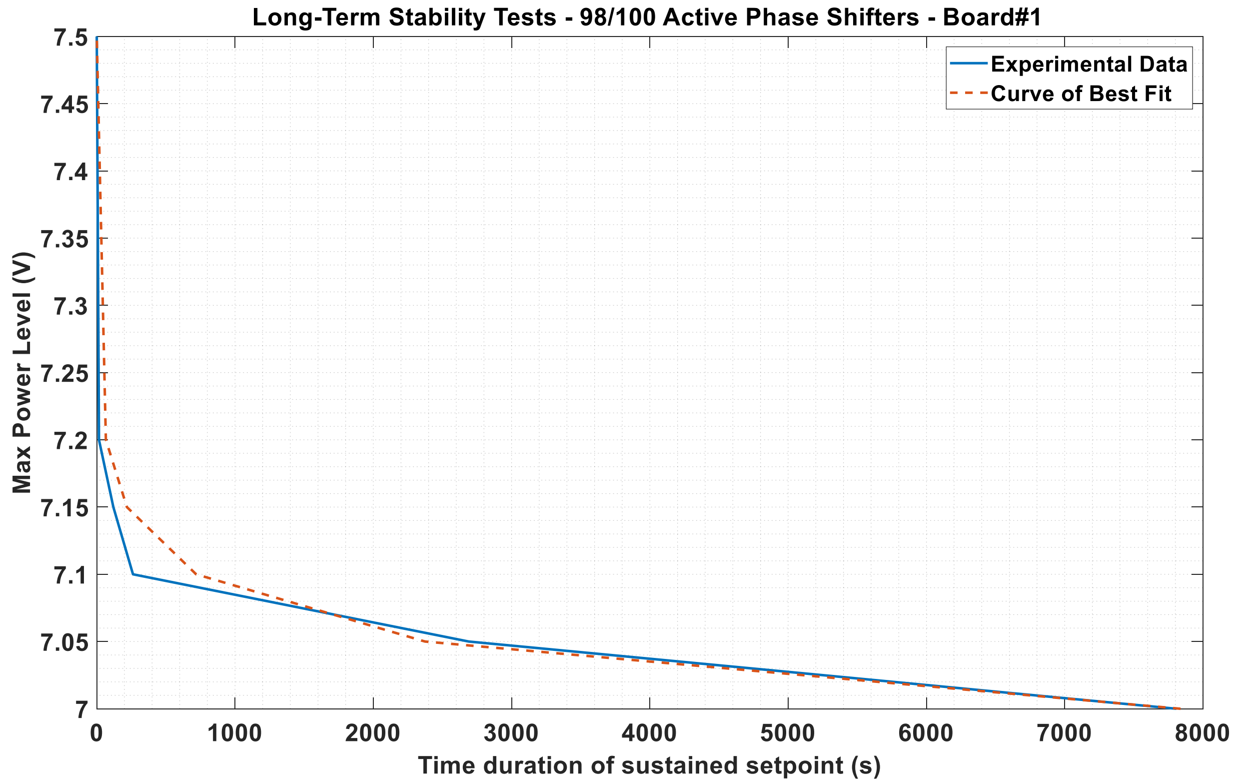

Figure 5.2: Long term setpoint stability based on maximum phase shifter power output.

The range under investigation was near the 70% power margins. An OPA power level above 72% or 7.2V caused the setpoint to be exceeded in under a few minutes. Incrementally lower power levels showed increasingly longer setpoint stability. The resultant exponential curve fit relationship defined in equation 5.1 indicates that while a 70% power test has an experimental long-term stability at setpoint of 7808 seconds, running the OPA at 69% would confer a long-term stability of almost 24 hours.

$$t_{Stable} = (3.32 * 10^{76})e^{-23.89P_{Max}} \quad \textbf{(5.1)}$$

Where t_{Stable} is the time the OPA remain stable at setpoint, and P_{Max} is the maximum power draw across all phase shifters simultaneously.

This implies that the limit of the TEC has been reached with respect to the limited 1.5A of current, and that unsustainability at and around the limit is a result of thermal saturation effects on

the OPA chip and the PCB. These tests confirm that the thermal control hardware is sufficient for baseline operational use.

5.1.2 Experimental PID Control Tests

With the maximum power benchmarks established, experimentally the PID values could be tuned using standard heuristic methods. The methods employed were the several variations of the Zeigler-Nichols approach as well as a Rule of Thumb variant [36]. Methods such as Cohen-Coon were not considered as the inherent decoupling of the optical and thermal control systems meant that there was not an accurate representation of the time delay. Each method variant considered required an ultimate gain K_u and an oscillation period T_u to quantify the proportional, integral, and derivative gains. The K_u and T_u were defined by the step response to a maximum power case (70%). The resultant PID values tested were generated from their respective formulae in the MATLAB code in Appendix C and are shown in Table 3.

Table 3: Experimentally Determined PID Tuning Variant Gains.

Zeigler-Nichols PID Tuning Variants *Ultimate Gain (Ku) = 3.00* *Oscillatory Period (Tu) = 7.49*	Proportional Gain (P)	Integral Gain (I)	Derivative Gain (D)
Proportional Control (P)	**1.500**	**--**	**--**
Proportional-Integral Control (PI)	**1.350**	**0.216**	**--**
Proportional-Derivative Control (PD)	**2.400**	**--**	**2.246**
Classic PID Control	**1.800**	**0.481**	**1.684**
Pessen Integral Rule Control	**2.100**	**0.701**	**2.358**
Some Overshoot PID Control	**1.000**	**0.267**	**2.495**

No Overshoot PID Control	**0.600**	**0.160**	**1.497**
Rule of Thumb PID Control	**6.000**	**11.229**	**2.246**

Given a 70% max power limit, a longform "staircase" step test was devised to record the responses for each group of PID values over several different forms and sizes of voltage drops. Each step was 100s and involved 10 divisions from 0.7V to 7V. The amalgamation of these tests is seen in Figure 5.3.

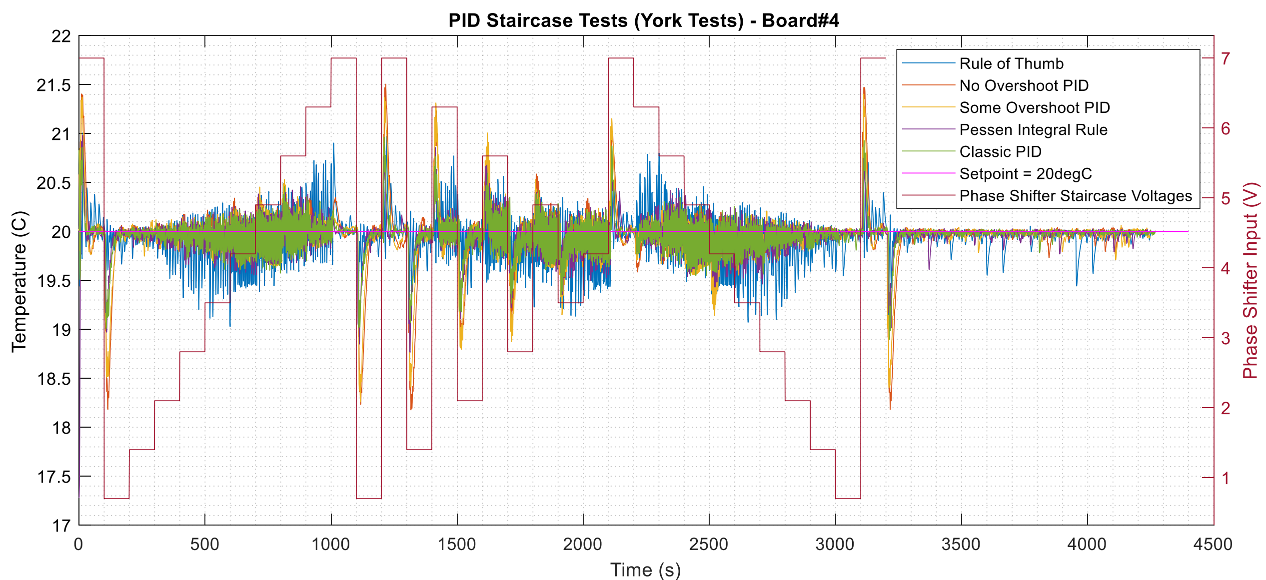

Figure 5.3: Staircase step tests for distinct groups of PID values.

Through a direct comparison of response times and overshoots of for each set of PID values, both the Classic PID approach and Pessen Integral Rule performed best, while the Some Overshoot and No Overshoot PID groups experience a longer settling time by a comparative 10 to 15 seconds depending on voltage drop. The Rule of Thumb response was the most chaotic with respect to the other groups and performed the worst. Further analysis will consider only the Classic dataset, for comparison to simulated actuator-plant control values.

5.2 Actuator-Plant Analysis

The analytical actuator-plant models for both the TEC and the OPA were not viable as discussed previously based on the hardware limitations and feedback sensor approach. The experimental benchmark data collected from the uncontrolled tests was used in tandem with the MATLAB System Identification Toolbox application to generate viable transfer functions to represent both the OPA and the TEC independently. However, the use of this tool with the step test data in Chapter 4 did not result in a consistent model across the suite power levels as seen by the step functions in Figure 5.4.

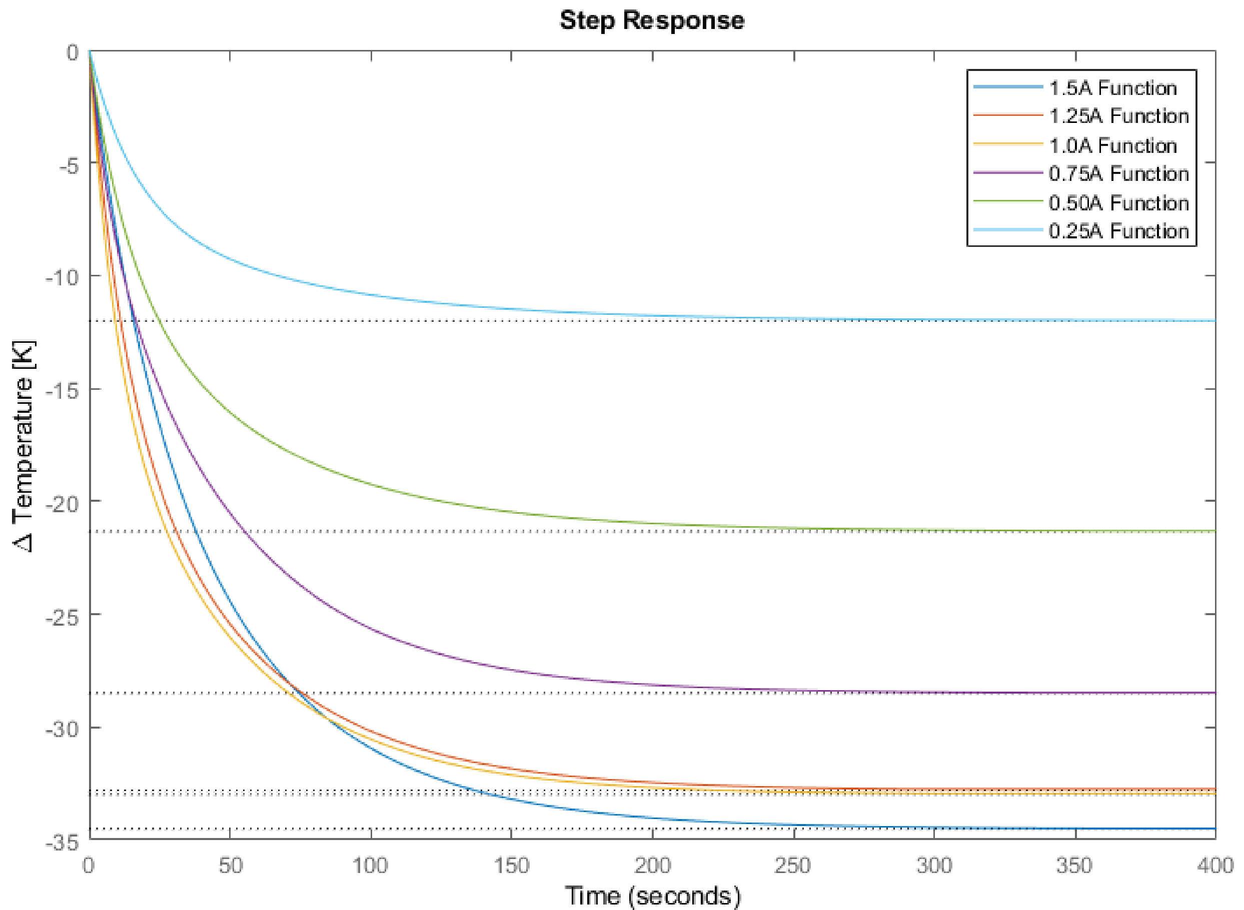

Figure 5.4: Step Response for experimentally derived transfer functions.

This implied that a simple first, second or third order transfer function would be insufficient on its own to represent the actuator-plant model on its own, and therefore several methods were explored to handle the non-linearity.

The first method was an averaging of the initial third order transfer functions generated by the System Identification toolbox. This existed as additional proof that a single function would be insufficient in comparison to the other methods. The second method involved function-scheduling, where the model was shifting between the benchmark transfer functions at each 0.25A level as a function of the present current input. The third method used a gain-scheduled approach where the present gain value was a direct function of the gains from the previous transfer functions. This method utilizes converting the transfer functions into first order with deadtime systems, requiring a gain k, a time constant τ_s, and a deadtime τ_{dead}, as per equation 5.2 and 5.3.

$$G(s) = e^{-s\tau_{dead}} * \frac{k}{\tau_s s + 1} \qquad \textbf{(5.2)}$$

$$\tau_s = \frac{k_{98\%} - \tau_d}{5} \qquad \textbf{(5.3)}$$

The deadtime for every case both simulated and experimentally was approximately one second, and as the gain would be attributed to its own input dependent function, it proved effective to use an averaged time constant value of 34.53s. The step responses for the modified transfer functions defined through equations 5.2 and 5.3 are seen in Figure 5.5 in red, where the original functions are in blue.

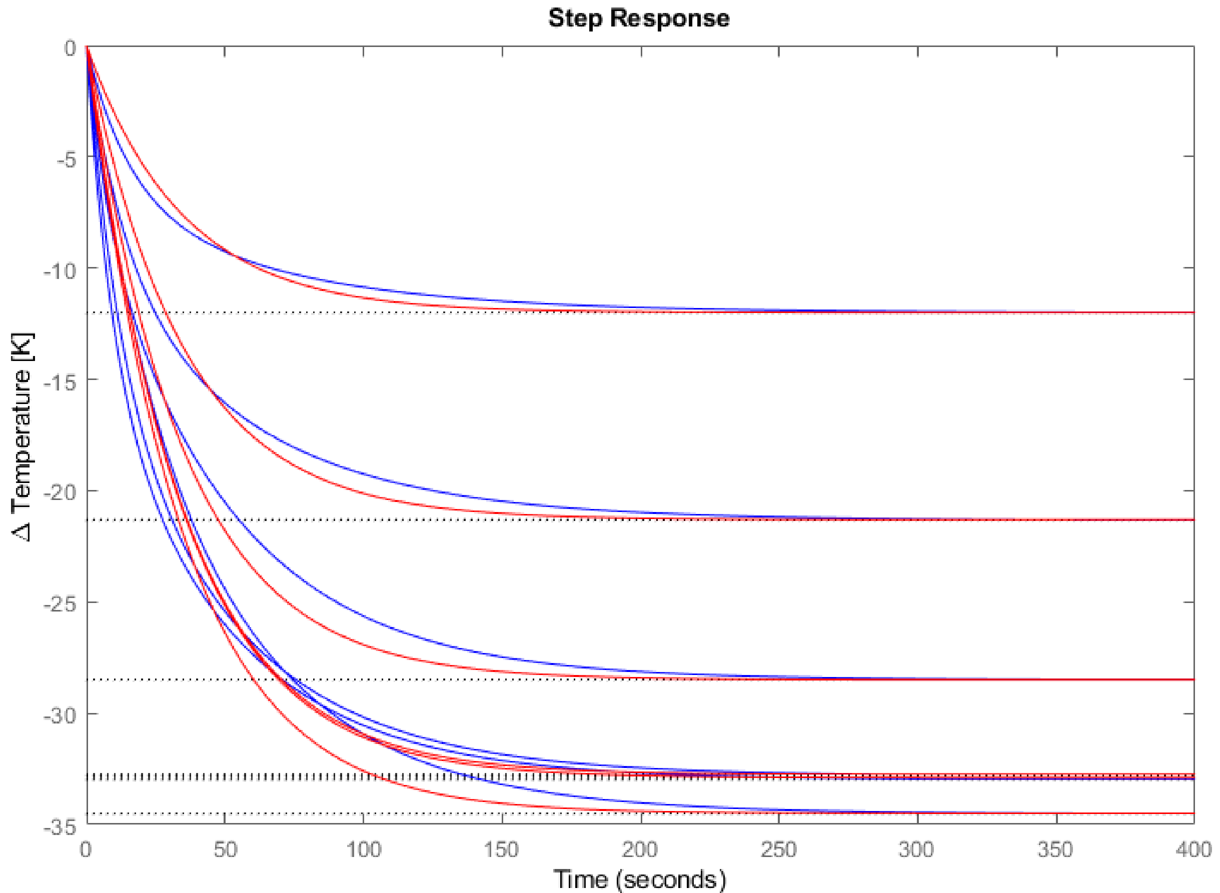

Figure 5.5: Step response for experimental transfer functions (blue) and modified transfer functions (red).

A first order polynomial function fit by the MATLAB Curve Fitting Toolbox functions as the representative relationship between the current input and the expected gain and can be imported using MATLAB functions into Simulink for PID comparison in Chapter 5.3.

For the closed loop system to be asymptotically stable, the poles must be located in the left half plane. The MATLAB function "isstable" returns true for all original and modified transfer functions, as well as all their poles having negative real parts. Therefore, the systems are closed loop stable. The stability margins from the Bode plots and Nyquist plots in Figures 5.6 and 5.7 respectively however indicate that it is closed loop unstable. Given that the previous stability criteria are fulfilled, it is valid to assume that our systems are indeed stable for the range of operation that we are expecting.

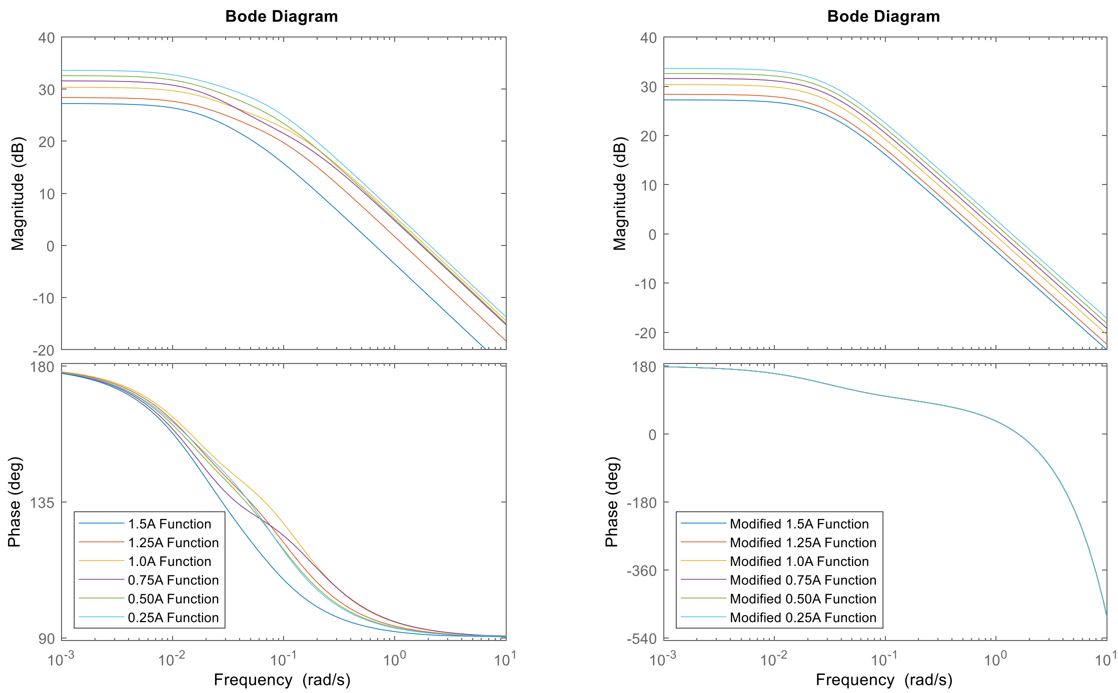

Figure 5.6: Bode plot comparison of experimental transfer functions to modified transfer functions.

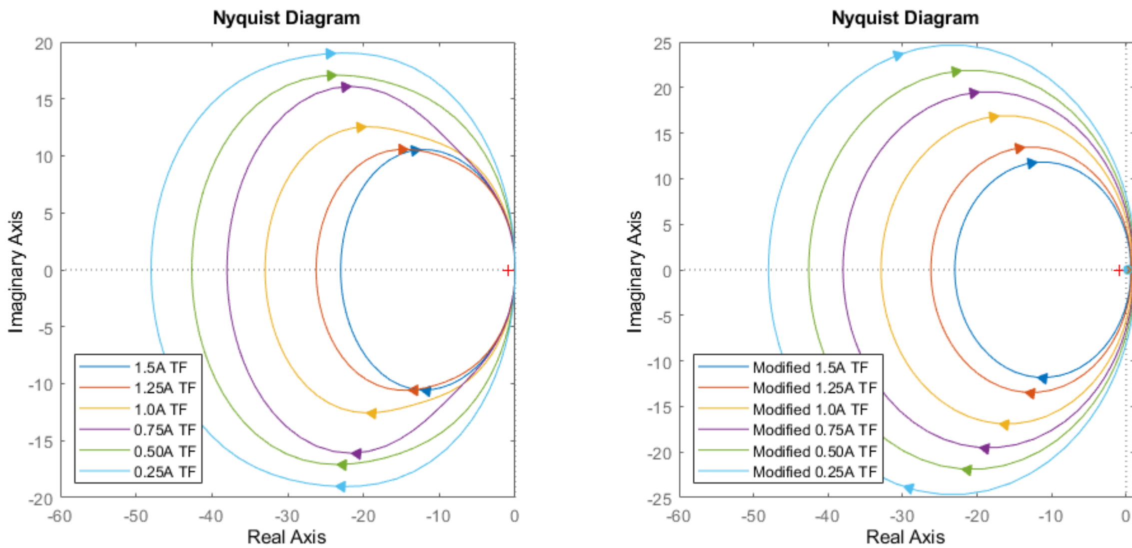

Figure 5.7: Nyquist plot comparison of experimental transfer functions to modified transfer functions.

Further investigation by converting these transfer functions to state-space form shows that the experimental functions all share a rank of 2, showing that they are controllable, while the

modified functions all share a rank of 1, also indicating that they are controllable. The observability tests indicate the ranks, mimicking the controllability tests in that the model has full rank of n.

5.3 MATLAB-Simulink Control Model Simulation

To run and compare the different actuator-plant model simulated approaches, an all-encompassing feedback loop was generated as seen in Figure 5.8.

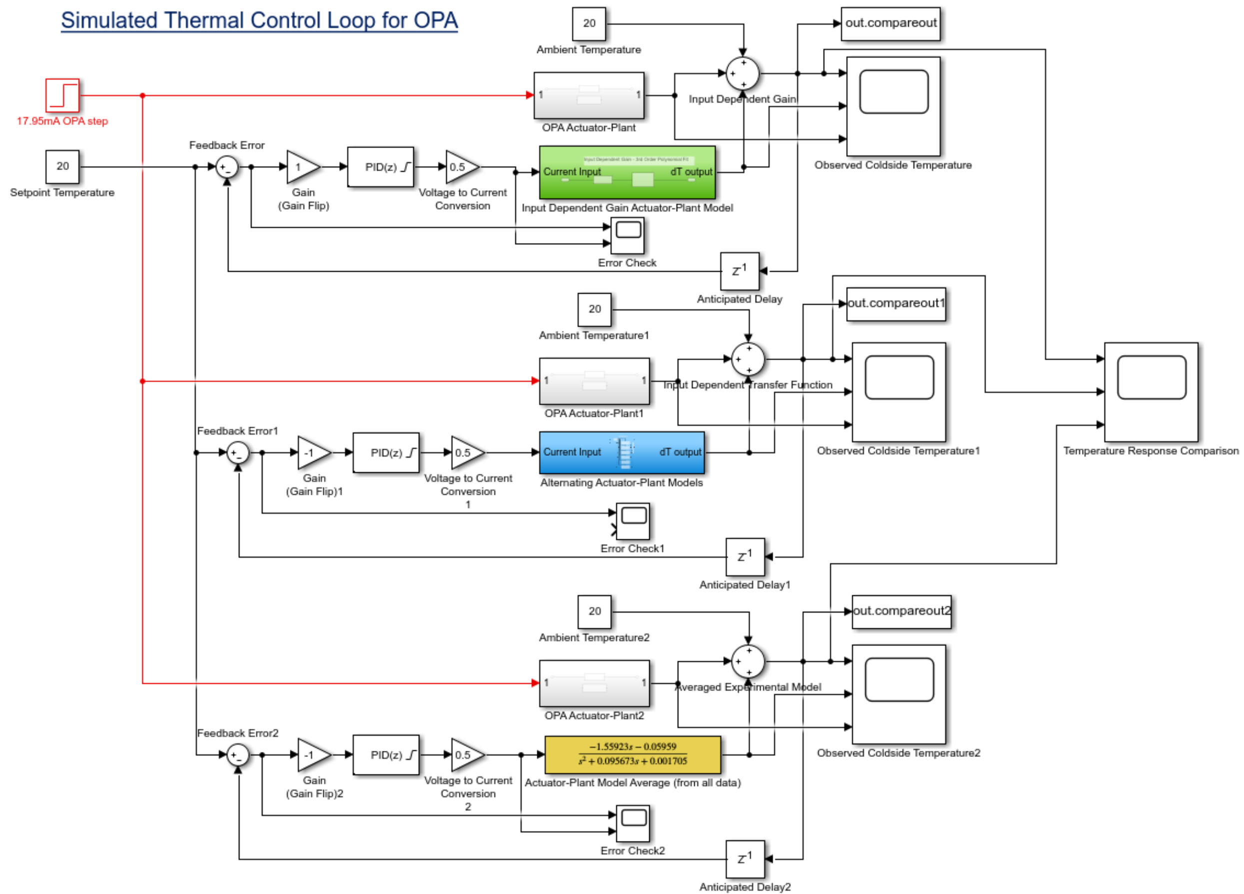

Figure 5.8: Simulink thermal control loop for actuator-plant model comparison.

The hardware loop seen in Figure 5.1 was used as a foundation where the NiDAQ input and output blocks are replaced by the simulated actuator-plant model counterparts. Each model requires a current input where the output is the change in temperature attributed to the process. To compare this directly to a constant setpoint, the resultant change in temperatures were summed to

both the known ambient temperature and the change in temperature generated by the OPA by means of a similar experimental transfer function representation. The summation dictates that the measured temperature to be compared to the setpoint temperature is the combination of how much heat the OPA is adding to the system and how much heat the TEC is removing from the system. The controller design is assumed to be controlling for the temperature difference as a function of the voltage output signals linearly corresponding to the output current. The full simulation contains three copies of the feedback loop, one for each approach. The input dependent gain approach utilizes a MATLAB function block, as referenced in Appendix D, for establishing gain and respective first order transfer function as seen in Figure 5.9.

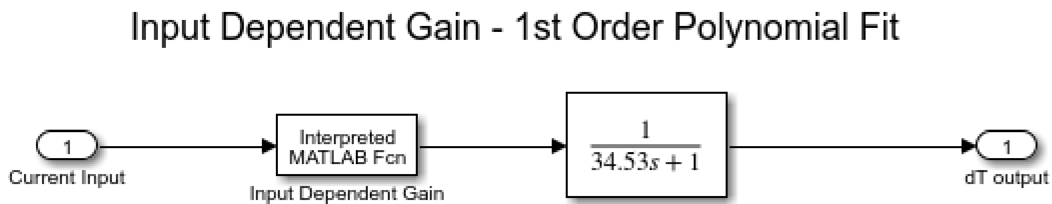

Figure 5.9: Input dependent gain actuator-plant model approach.

The input dependent transfer function approach on the other hand utilizes if statements within Simulink and are seen in Figure 5.10.

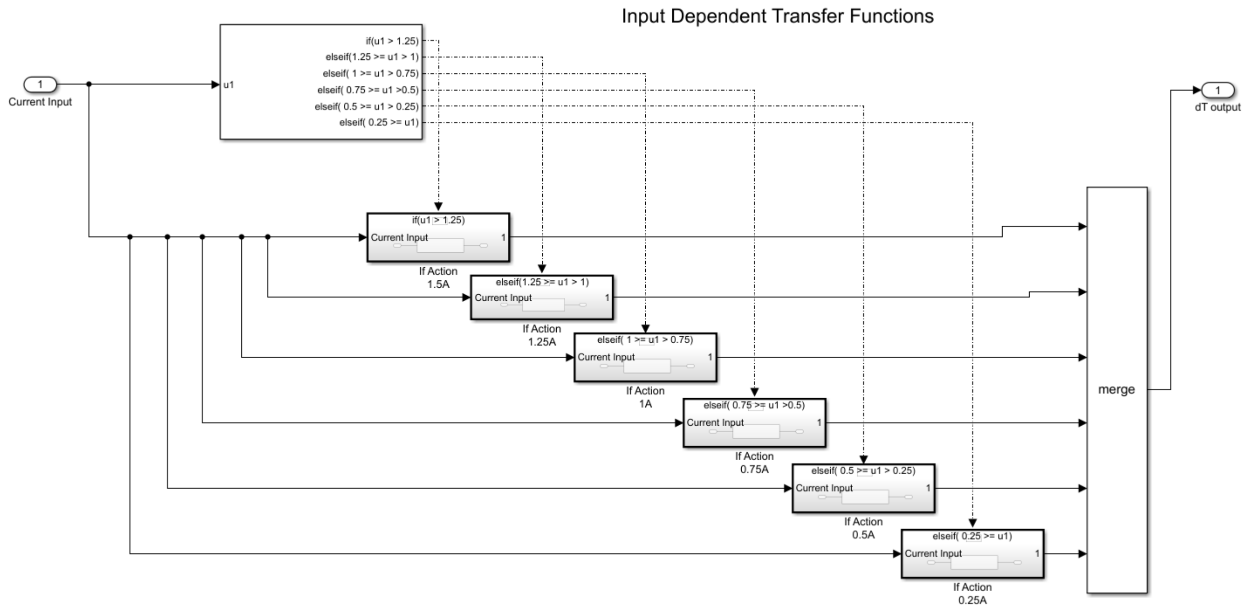

Figure 5.10: Input dependent transfer function if statement block.

This approach shifts the active transfer function based on the current input value. By running all approaches simultaneously, the responses to their independent PID values can be compared directly to any manner of step or temperature disturbances generated by the OPA. The simulation was designed in a manner where the OPA current input and transfer function could be swapped out for direct temperature values without issue.

Given the nature of the actuator-plant model designs, the PID Tuner application in MATLAB-Simulink was not sufficient for certain conditions of controller optimization. The initial controller design for each approach was set at the most effective values from the previous heuristic testing in Chapter 5.1.2. From there much experimentation was observed in setting PID values in a range around the initial values to see in which directions the responses trended. Both the input dependent gain and the averaged transfer function approaches did benefit from the MATLAB-Simulink PID Tuner application to increase speed and robustness in their controller responses. The resultant best case PID values for each approach were recorded in Table 4 and their simulated

responses are seen in Figure 5.11 where each approach was run against a maximum step temperature response from the OPA.

Table 4: Optimal simulated PID values.

Actuator Plant Method	Proportional Gain (P)	Integral Gain (I)	Derivative Gain (D)
Heuristic Classic PID	**1.800**	**0.481**	**1.684**
Input Dependent Gain	**1.944**	**0.102**	**1.863**
Input Dependent Transfer Function	**1.800**	**0.600**	**0.800**
Averaged Transfer Function	**0.585**	**0.041**	**0.550**

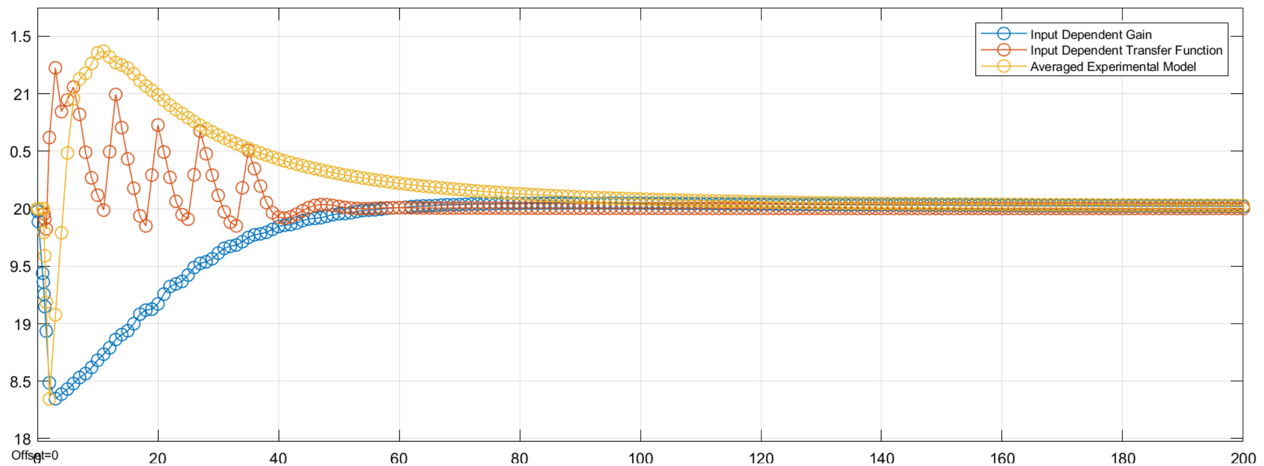

Figure 5.11: Response plots for optimized PID value simulations.

The transfer function structure of each model response shows the efficiency in which the system returns to setpoint during an initial step input. The input dependent gain approach course corrects sooner than the averaged experimental transfer model, which appears erratic after the initial step input. The input dependent transfer function approach can be seen with the jagged response, indicating the shifting of active transfer functions much like switching gears in manual transmission car. The response plots from each actuator-plant model approach show that both input

dependent methods have a settling time of around 40 seconds, while the averaged transfer function model settling time is closer to 80 seconds. This indicates that the averaged transfer function does not account for the non-linearities of the system as much as the input dependent methods, and suffers in performance as a result.

5.4 Optimized PID Response Comparison

Taking the optimized PID values from Table 4, a new set of staircase step tests was conducted. The purpose was to see the settling time and overshoot responses for each approach with respect the size of voltage drops experienced by the OPA. Each variant was run over the same series of step formations, where the complete response data is seen in Figure 5.12, with Figure 5.13 displaying a zoomed in view of the first three voltage steps.

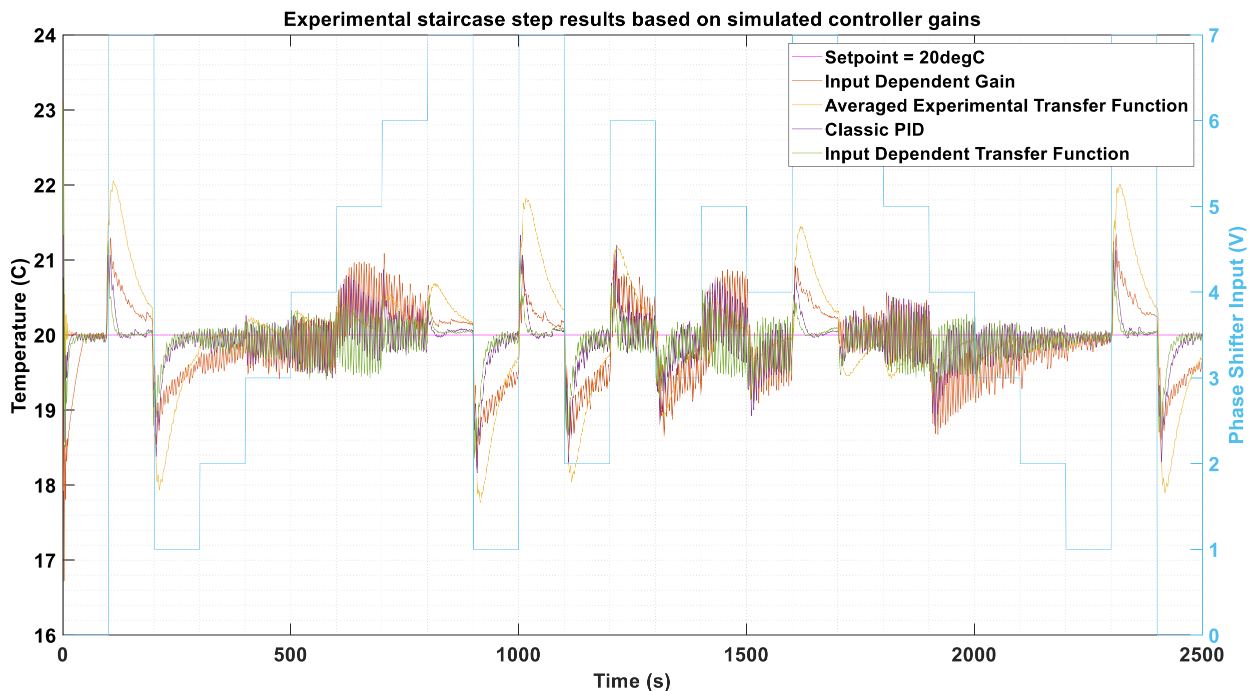

Figure 5.12: Experimental staircase step results based on the simulated controller gains.

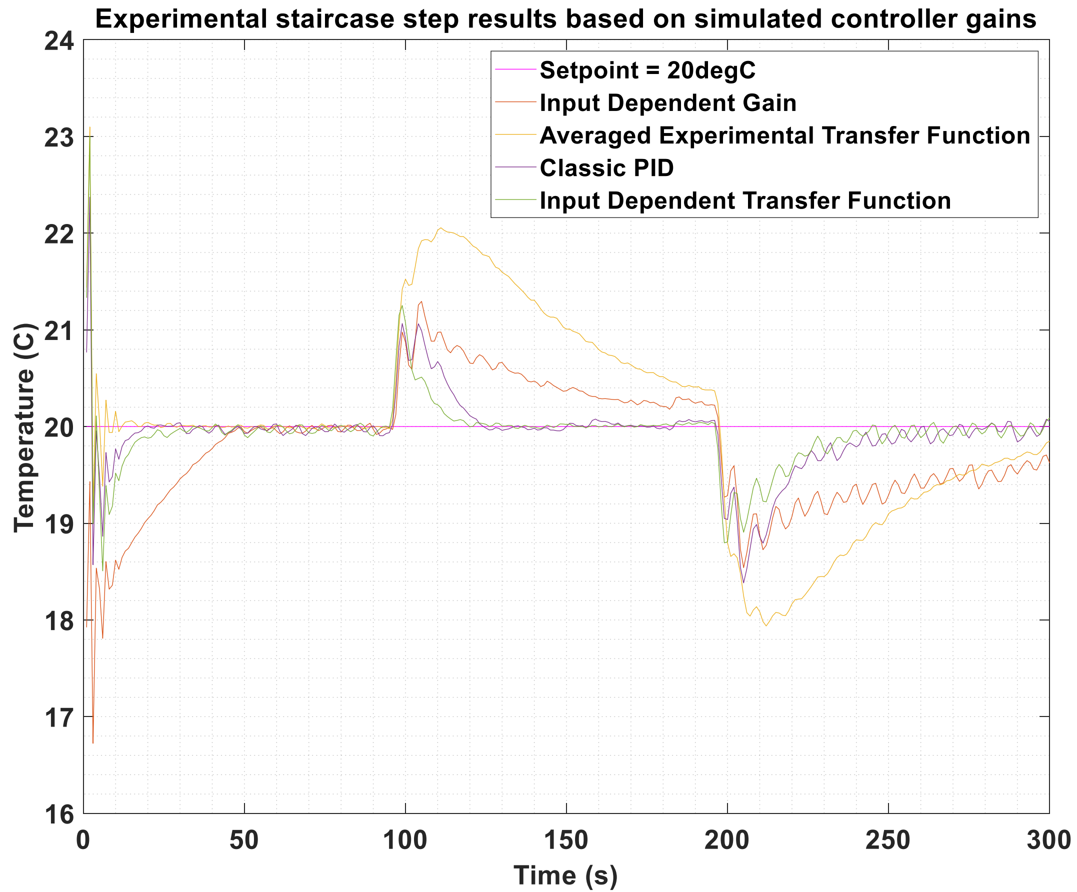

Figure 5.13: A zoomed in version of the experimental comparison tests showing the first three 100s step inputs of 0V, 7V, and 1V respectively.

From the immediate response, it appears that both the classic PID and input dependent transfer function approaches were the best performing both with the smaller overshoots and faster settling times. To analyze the response times further, these two datasets were organized in a scatter plot in Figure 5.14 corresponding to the visible settling time against the respective voltage drop or jump. A voltage drop is when the OPA goes from a higher to a lower power output and a voltage jump is the opposite.

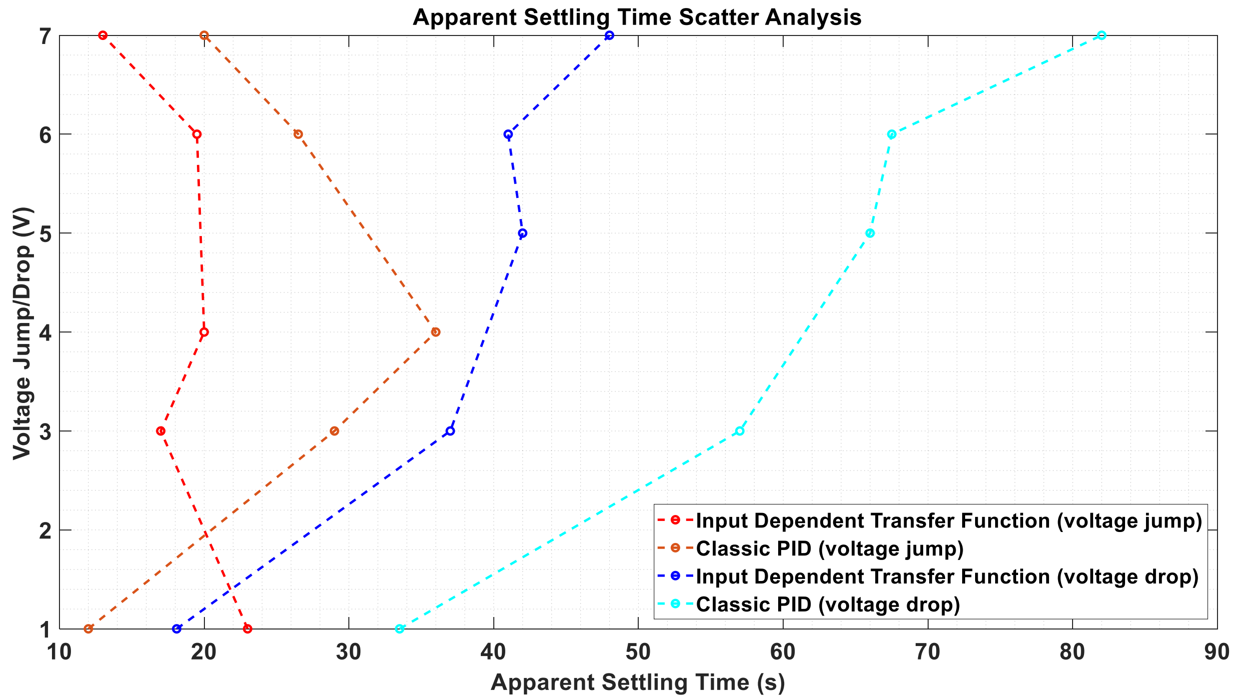

Figure 5.14: Scatter plot of observed settling times per voltage drop/jump.

From the observed responses, the current driver's inability to generate current in both directions results in responses from voltage drops to approximately double the duration of those from voltage jumps. While the TEC can respond to the voltage jumps by correcting directly, the voltage drops cause the system to wait for the TEC warm up by being inactive and allowing reflow heat. The scatter plot also indicates that from the observed responses, the PID values associated with the input dependent transfer function approach resulted in faster settling times for both voltage drops and jumps in comparison to that of the classic PID values. Therefore, this system's PID values for optimized controller response are P = 1.8, I = 0.6, and D = 0.8. These values correspond to an average settling time response of 18.5 seconds for voltage jumps, and 27.5 seconds for voltage drops.

Chapter 6
Final Remarks

The OPA project continues with the support of the participating university teams and Honeywell. The hardware and software designs completed in this thesis are adopted by the teams for their ongoing optical tests and second generation OPA device. This project was limited by the available hardware in the testing phase and thus all results are characterized with respect to those limitations. Future work will involve redesigning the hardware layout to be applicable as a stand-alone module for testing environment and eventually in space applications.

6.1 Contribution

The thermal control system setup is currently being replicated at Carleton University as a backbone to their optical tests. Beyond this, the research covered in this report aims to act as a foundation for continued improvements to the efficiency of an external thermal control on a microphotonics platform through the design of the material medium between them, and through the impact of a characterized PID controller. Additionally, simulation work on the OPA further provides insight into the efficiency of passive internal thermal control techniques.

Early predictions indicate that the limiting factor of the thermal uniformity between the chip and the TEC module will be the maximum diameter of manufacturable through-hole vias on the PCB. Further investigation into new geometries depends on manufacturing capabilities available, however novel in-house techniques might yield more favorable results.

The impact of this work is that the design of the medium between the OPA and any external thermal control would translate into package design rules that could greatly improve the thermal environment for components in and beyond the field of microphotonics. By increasing thermal

control, the thermal gradient between components shrinks and/or becomes more quantifiable; this translates into better calibration against signal noise and crosstalk, ultimately resulting in a better signal output.

To summarize, the contributions of this research are:

- Thermal crosstalk relationship of the OPA through the simulated response of COMSOL Multiphysics models.
- Hardware integration design for a solid state thermal actuator and commercial off-the-shelf (COTS) components for experimental testing of an OPA.
- Chip level thermal control providing experimental and simulated values for the minimized settling of this version of an OPA and for all future iterations of an OPA of these dimensions/form factor.

6.2 Future Research and Design

Past the scope of this project, this research aims to positively guide future designs for microphotonics platforms. This research will lead to a more unified approach to the design of optical communication devices, using underlying technologies as the backbone of efficient thermal control and operation. By developing and comparing methods of thermal control, future risks of component failure can be reduced in-situ. The testing of these platforms in various atmospheric and vacuum conditions will further demonstrate that the given approach to thermal control is viable in terms of cost, mass, and performance.

Beyond the current project, there are several areas of further research that are under consideration for OPA development. Further steady-state models will focus on expanding the size of the phase shifter array and comparing the thermal crosstalk of several patterns of active and inactive phase shifters. While the goal is to simulate all one hundred in the array, the complexity

of the model might be too intensive to run on conventional hardware within a reasonable amount of time. While the resolution of the model can be scaled down, sacrificing accuracy in the process, the entire array may not be necessary if results can be extrapolated from analysis of the smaller array sets.

The Honeywell team have, with the benefit of these simulations and the simulations of other teams, made the executive decision to continue the second iteration of the on-chip OPA with the same design of the phase shifters and the structures surrounding them. As a result, the focus of the future models will not involve the investigation of different passive structures.

With the second iteration of the on-chip OPA scheduled to arrive at the Honeywell facility labs in the following financial quarter of 2022, there have already been multiple improvements made to the OPA Carrier PCB through lessons learned from the full test setup on the first iteration. The most immediate issue to rectify is the space between the OPA and the eight full sized thirty-four pin connectors. The amount of space between them was assumed to be enough, given the distance the cameras and microscopes would be from the chip surface; however, with the new introduction of mid-stage lenses for the purpose of resolving both the near-field and far-field patterns of the OPA, the distance given in the previous design proved non-optimal.

With respect to the thermal control loop, further literature review is warranted with respect to PCB integrated thermocouple or temperature sensor designs to eventually replace the obtrusive use of standard sized thermistor. The generous space underneath the PCB was intended to compensate for any hardware changes that may be included or excluded from the testing phase. Additionally, research is being done into the viability of prebuilt butterfly packaging to replace the PCB interface. The butterfly packaging has the possibility of being hermetically sealed whereas

the PCB does not and may include its own version of a built in TEC module. Further characterization of efficiency profiles would be required should this be the case.

Furthermore, a more compact hardware setup with regards to driving sufficient power is being investigated as a direct replacement for the power supply and current driver modules.

6.3 Summary

Results of the work done upon the design and characterization of the first iteration (V1) OPA have demonstrated that thermal control is both beneficial and necessary to the effective operation of the device. The COMSOL time dependent simulations show the rates of temperature increase that are countered by the thermal control. The steady-state simulations present a proportional relationship to the minimized thermal crosstalk that can be accounted for by the optical control. The thermal control design accounts for up to 1.5A of input current and up to 70% of OPA operational capacity and can be easily tuned and refit to accommodate new architecture and limits. The feedback PID control system approach to modelling results in minimized overshoot to within one degree and with an average settling time of 18.5 and 27.5 seconds for voltage jumps and drops respectively and can hold setpoint temperatures for several hours with an accuracy of 0.2 degrees.

References

[1] F. Zamkotsian, "Optical MEMS for space: Design, characterization, and applications," *Optical MEMS, Nanophotonics, and Their Applications,* G.Zhou and C. Lee, Ed. Boca Raton, NY, USA: CRC Press, 2009.

[2] C. V. Poulton et al., "Long-Range LiDAR and Free-Space Data Communication with High-Performance Optical Phased Arrays," IEEE J. Sel. Top. Quantum Electron., vol. 25, no. 5, 2019, doi: 10.1109/JSTQE.2019.2908555.

[3] C. P. Ho, Z. Zhao, Q. Li, S. Takagi, and M. Takenaka, "Tunable Grating Coupler by Thermal Actuation and Thermo-Optic Effect," IEEE Photonics Technol. Lett., vol. 30, no. 17, pp. 1503–1506, 2018, doi: 10.1109/LPT.2018.2857469.

[4] Gross, Andrew John. "Low Power, Integrated, Thermoelectric Micro-Coolers for Microsystems Applications." ProQuest Dissertations Publishing, 2010. Print.

[5] Tritt, Terry M. "Thermoelectric Phenomena, Materials, and Applications." Annual review of materials research 41.1 (2011): 433–448. Web.

[6] C. V. Poulton *et al.*, "Coherent solid-state LIDAR with silicon photonic optical phased arrays," *Opt. Lett.*, vol. 42, no. 20, p. 4091, 2017, doi: 10.1364/ol.42.004091.

[7] J. Kim *et al.*, "1100 × 1100 port MEMS-based optical crossconnect with 4-dB maximum loss," *IEEE Photonics Technol. Lett.*, vol. 15, no. 11, pp. 1537–1539, 2003, doi: 10.1109/LPT.2003.818653.

[8] S. Sabouri and K. Jamshidi, "Design Considerations of Silicon Nitride Optical Phased Array for Visible Light Communications," *IEEE J. Sel. Top. Quantum Electron.*, vol. 24, no. 6, 2018, doi: 10.1109/JSTQE.2018.2836991.

[9] H. Nguyen, J. G. D. Su, H. Toshiyoshi, and M. C. Wu, "Device transplant of optical MEMS

for out of plane beam steering," *Proc. IEEE Micro Electro Mech. Syst.*, no. August 2017, pp. 325–328, 2001, doi: 10.1109/memsys.2001.906544.

[10] A. Tuantranont, V. M. Bright, J. Zhang, W. Zhang, J. A. Neff, and Y. C. Lee, "Optical beam steering using MEMS-controllable microlens array," *Sensors Actuators, A Phys.*, vol. 90, no. 3, pp. 363–372, 2001, doi: 10.1016/s0924-4247(01)00609-4.

[11] F. Filhol, E. Defaÿ, C. Divoux, C. Zinck, and M. T. Delaye, "Resonant micro-mirror excited by a thin-film piezoelectric actuator for fast optical beam scanning," *Sensors Actuators, A Phys.*, vol. 123–124, pp. 483–489, 2005, doi: 10.1016/j.sna.2005.04.029.

[12] J. Kim, M. N. Miskiewicz, S. Serati, and M. J. Escuti, "Nonmechanical Laser Beam Steering Based on Polymer Polarization Gratings: Design Optimization and Demonstration," *J. Light. Technol.*, vol. 33, no. 10, pp. 2068–2077, 2015, doi: 10.1109/JLT.2015.2392694.

[13] Y. Wang and M. Wu, "Optical micro-electrical-mechanical phased array," *Optical MEMS, Nanophotonics, and Their Applications,* G.Zhou and C. Lee, Ed. Boca Raton, NY, USA: CRC Press, 2009.

[14] W. Xu, L. Lu, L. Zhou, and J. Chen, "Reconfiguring the 16 × 16 silicon optical switch for optical beam steering application," *MWP 2017 - 2017 Int. Top. Meet. Microw. Photonics*, vol. 2017-Decem, pp. 1–4, 2017, doi: 10.1109/MWP.2017.8168790.

[15] W. Bogaerts, M. Fiers, and P. Dumon, "Design Challenges in Silicon Photonics," *IEEE J. Sel. Top. Quantum Electron.*, vol. 20, no. 4, pp. 1–8, 2014, doi: 10.1109/JSTQE.2013.2295882.

[16] Image by Chetvorno, distributed under a CC0 license. Available: https://commons.wikimedia.org/wiki/File:Phased_array_animation_with_arrow_10frames_371x400px_100ms.gif

[17] J. K. Doylend, M. J. R. Heck, J. T. Bovington, J. D. Peters, L. A. Coldren, and J. E. Bowers, "Two-dimensional free-space beam steering with an optical phased array on silicon-on-insulator," *Opt. Express*, vol. 19, no. 22, p. 21595, 2011, doi: 10.1364/oe.19.021595.

[18] C. Mekhiel and X. Fernando, "Monolithic silicon-on-insulator optical beam steering with phase locking heterodyne feedback," *IEEE Int. Symp. Pers. Indoor Mob. Radio Commun. PIMRC*, vol. 2017-Octob, pp. 1–5, 2018, doi: 10.1109/PIMRC.2017.8292184.

[19] S. Chung, H. Abediasl, and H. Hashemi, "A Monolithically Integrated Large-Scale Optical Phased Array in Silicon-on-Insulator CMOS," IEEE J. Solid-State Circuits, vol. 53, no. 1, pp. 275–296, 2018, doi: 10.1109/JSSC.2017.2757009.

[20] J. H. Lienhard, IV, J. H. and Lienhard, V, *A Heat Transfer Textbook*, 5th ed. Phlogiston Press, 2020.

[21] Y.A. Cengel and A. J. Ghajar, *Heat and Mass Transfer: Fundamentals & Applications*, 5th ed. New York, NY, USA: McGrawHill, 2015.

[22] F.P. Incropera, D.P. Dewitt, T.L. Bergman, and A.S. Lavine, *Fundamentals of Heat and Mass Transfer*, 6th ed. Hoboken, NJ, USA: John Wiley & Sons, 2007.

[23] L.M Jiji, *Heat Conduction*, 3rd ed. Berlin, Germany: Springer, 2009.

[24] C. J. M. Lasance, "Ten years of boundary-condition- Independent compact thermal modeling of electronic parts: A review," Heat Transf. Eng., vol. 29, no. 2, pp. 149–168, 2008, doi: 10.1080/01457630701673188.

[25] A. K. Sharma and N. Sridhara, "Degradation of thermal control materials under a simulated radiative space environment," Adv. Sp. Res., vol. 50, no. 10, pp. 1411–1424, 2012, doi: 10.1016/j.asr.2012.07.010.

[26] P. A. K. Yepez, U. Scholz, J. N. Caspers, and A. Zimmermann, "Novel Measures for

Thermal Management of Silicon Photonic Optical Phased Arrays," *IEEE Photonics J.*, vol. 11, no. 4, 2019, doi: 10.1109/JPHOT.2019.2925138.

[27] M. S. Santhanakrishnan *et al.*, "CMOS-compatible measures for thermal management of phase-sensitive silicon photonic systems," *Photonics*, vol. 7, no. 1, pp. 1–4, 2020, doi: 10.3390/photonics7010006.

[28] Y. Wang *et al.*, "Improved performance of optical phased arrays assisted by transparent graphene nanoheaters and air trenches," *RSC Adv.*, vol. 8, no. 15, pp. 8442–8449, 2018, doi: 10.1039/c7ra13154b.

[29] Laird Thermal Systems, "HiTemp ET Series Thermoelectric Cooler," HiTemp ET Series ET2.3-49-F1-1919-TA-RT-W6, Apr. 24, 2020. [Online]. Available: https://lairdthermal.com/products/thermoelectric-cooler-modules/peltier-hitemp-et-series/ET2.3-49-F1-1919-TA-RT-W6/pdf/

[30] Ivaylo Belovski, Liliya Staneva, Anatoliy Aleksandrov, and Pavlik Rahnev, "Mathematical Model of Thermoelectric Peltier Module," J. Commun. Comput., vol. 14, no. 2, pp. 60–64, 2017, doi: 10.17265/1548-7709/2017.02.002.

[31] G. A. Mannella, V. La Carrubba, and V. Brucato, "Peltier cells as temperature control elements: Experimental characterization and modeling," Appl. Therm. Eng., vol. 63, no. 1, pp. 234–245, 2014, doi: 10.1016/j.applthermaleng.2013.10.069.

[32] B. J. Huang and C. L. Duang, "System dynamic model and temperature control of a thermoelectric cooler," Int. J. Refrig., vol. 23, no. 3, pp. 197–207, 2000, doi: 10.1016/S0140-7007(99)00045-6.

[33] A. M. N. Lima, G. S. Deep, L. A. L. De Almeida, H. Neff, and M. Fontana, "A gain-scheduling PID-like controller for peltier-based thermal hysteresis characterization

platform," Conf. Rec. - IEEE Instrum. Meas. Technol. Conf., vol. 2, no. February, pp. 919–924, 2001, doi: 10.1109/IMTC.2001.928213.

[34] S. Shaojing and Qinqin, "Temperature control of thermoelectric cooler based on adaptive NN-PID," Proc. - Int. Conf. Electr. Control Eng. ICECE 2010, pp. 2245–2248, 2010, doi: 10.1109/iCECE.2010.553.

[35] Arroyo Instruments, "P/N 1600-10K Thermistor," P/N 530-1016 Rev D, 2012. [Online]. Available:https://www.arroyoinstruments.com/wp-content/uploads/2021/02/ArroyoThermistorInstructions.pdf

[36] J.G. Zeigler and N.B. Nichols, *Optimum Settings for Automatic Controllers*, Rochester, N.Y. First published "Transactions of the A. S. M. E.", November 1942

[37] Y. K. Singh, J. Kumar, K. K. Pandey, K. Rohit, and A. Bhargav, "Temperature Control System and its Control using PID Controller," Int. J. Eng. Res. Technol., vol. 4, no. 02, pp. 4–6, 2016.

[38] B. Stute, V. Krupp, and E. Von Lieres, "Performance of iterative equation solvers for mass transfer problems in three-dimensional sphere packings in COMSOL," Simul. Model. Pract. Theory, vol. 33, pp. 115–131, 2013, doi: 10.1016/j.simpat.2012.10.004.

[39] E. J. F. Dickinson, H. Ekström, and E. Fontes, "COMSOL Multiphysics®: Finite element software for electrochemical analysis. A mini-review," Electrochem. commun., vol. 40, pp. 71–74, 2014, doi: 10.1016/j.elecom.2013.12.020.

[40] M. Arik, C. A. Becker, S. E. Weaver, and J. Petroski, "Thermal management of LEDs: package to system," Third Int. Conf. Solid State Light., vol. 5187, no. January, p. 64, 2004, doi: 10.1117/12.512731.

[41] A. G. Fedorov and R. Viskanta, "Three-dimensional conjugate heat transfer in the

microchannel heat sink for electronic packaging," Int. J. Heat Mass Transf., vol. 43, no. 3, pp. 399–415, 2000, doi: 10.1016/S0017-9310(99)00151-9.

[42] A. Helmy, (2021) Progress and research update for Honeywell, 13 May.

[43] D. S. Gautam, F. Musavi, D. Wager, and M. Edington, "A comparison of thermal vias patterns used for thermal management in power converter," 2013 IEEE Energy Convers. Congr. Expo. ECCE 2013, pp. 2214–2218, 2013, doi: 10.1109/ECCE.2013.6646981.

[44] R. S. Li, "Optimization of thermal via design parameters based on an analytical thermal resistance model," Thermomechanical Phenom. Electron. Syst. -Proceedings Intersoc. Conf., pp. 475–480, 1998, doi: 10.1109/itherm.1998.689605.

[45] Y. Shen, H. Wang, F. Blaabjerg, H. Zhao, and T. Long, "Thermal modeling and design optimization of PCB vias and pads," IEEE Trans. Power Electron., vol. 35, no. 1, pp. 882–900, 2020, doi: 10.1109/TPEL.2019.2915029.

[46] *5240 Series TECSource Temperature Controller,* 520-1013, Rev. A, Arroyo Instruments, 2022. [Online]. Available: https://www.arroyoinstruments.com/wp-content/uploads/2021/04/5240-Series-TECSource-Datasheet.pdf

[47] J. Malaco, M. Asch, et al, "Cross-platform CLI and Python drivers for AIO liquid coolers and other devices," liquidctl v1.9.1. Apr 5, 2022, Github, [Online]. Available: https://github.com/liquidctl/liquidctl

[48] H. L. Tsai and J. M. Lin, "Model building and simulation of thermoelectric module using Matlab/Simulink," J. Electron. Mater., vol. 39, no. 9, pp. 2105–2111, 2010, doi: 10.1007/s11664-009-0994-x.

[49] H. Lu, "Peltier Temperature Controller A Design Project Report MEng Field Advisor: Bruce Land MEng Outside Field Advisor: Bruce Johnson," 2013.

[50] E. Picco, “Temperature control system development in microfluidic environment for biological purposes,” no. July 2020, 2020, [Online]. Available: http://webthesis.biblio.polito.it/id/eprint/15370.

[51] J. Ventura, T. H. Moita, and M. B. Dos Santos, “Characterization of temperature sensors using Peltier cells,” 2016 IEEE 21st Int. Mix. Test. Work. IMSTW 2016, pp. 1–9, 2016, doi: 10.1109/IMS3TW.2016.7524220.

Appendices

Appendix A: MATLAB Code: HomogeneousMaterialCalculator.m

```
% Nicholas Zonta - 212141636
clear;
clc;

%% Homogeneous Material Percentage Calculator

% This script takes the material property values of individual materials
% and generates the property values for representative homogeneous
% materials respective of defined material percentages.

mat_term = ["Density", "Thermal Conductivity", "Heat Capacity", "Electrical
Conductivity", "Relative Permittivity", "Youngs Modulus", "Poissons Ratio"];
siO2 = [2648 12 700 1e-12 11.7 170e9 0.28]; %Silicon Dioxide
siN = [3100 20 700 0 9.7 250e9 0.23]; %Silicon Nitride
amoS = []; %Amorphous Silicon
air = [1.208 0.02572 1006 5e-15 1 0 0]; %Ambient Natural Air
alum = [2700 238 900 3.774e7 1 70e9 0.33];%Aluminum
copp = []; %Copper
fr4 = []; %PCB FR4 Insulator

% Total Percentage of Material is as follows:
% [89% SiO2, 10% SiN, and 1% Aluminum]
metamaterial = (0.89.*siO2) + (0.10.*siN) + (0.01.*alum);

fprintf(mat_term(1));
disp(metamaterial(1));
fprintf(mat_term(2));
disp(metamaterial(2));
fprintf(mat_term(3));
disp(metamaterial(3));
fprintf(mat_term(4));
disp(metamaterial(4));
fprintf(mat_term(5));
disp(metamaterial(5));
fprintf(mat_term(6));
disp(metamaterial(6));
fprintf(mat_term(7));
disp(metamaterial(7));
```

Appendix B: MATLAB Code: ThermistorConverter2.m

```
function [T] = ThermistorConverter2(Vsense)
%   This code is for the new TH10K Thorlabs thermistors. The previous
%   version was for the Arroyo 10K thermistors used previously for
%   measurements taken on the 33% board. V1 is commented out below.
%{
Rbias = 8250; %8.25kOhms
Vin = 5; %Volts
R = Rbias.*((Vin./Vsense)-1);
% Steinhart-Hart Equation
A = 1.12924E-03;
B = 2.34108E-04;
C = 0.87755E-07;
lnR = log(R);
denomT = A+B.*(lnR)+C.*((lnR).^3);
T = (1./denomT)-273.15;
%}

% Converting from Voltage to Temperature
Rbias = 8250;                 %8.25kOhms
Vin = 5;                      %Volts
R = Rbias.*((Vin./Vsense)-1); %Resistance across the Thermistor

if (R > 32770)                % Resistance Variables
    A = 3.3570420E-03;
    B = 2.5214848E-04;
    C = 3.3743283E-06;
    D = -6.4957311E-08;
elseif (R >= 3599) && (R<32770)
    A = 3.3540170E-03;
    B = 2.5617244E-04;
    C = 2.1400943E-06;
    D = -7.2405219E-08;
elseif (R >= 681.6) && (R<3599)
    A = 3.3530481E-03;
    B = 2.5420230E-04;
    C = 1.1431163E-06;
    D = -6.9383563E-08;
else
    A = 3.3536166E-03;
    B = 2.5377200E-04;
    C = 8.5433271E-07;
    D = -8.7912262E-08;
end
% Temperature Formula
lnR = log(R./10000);
denomT = A+B.*(lnR)+C.*((lnR).^2)+D.*((lnR).^3);
T = (1./denomT)-273.15;
end
```

Appendix C: MATLAB Code: ZeiglerNicholsAutoCalculator.m

```
%% ZeiglerNichols PID Value Calculator
% This code takes in the Ku and Tu values found experimentally and converts
% them to valid Kp Ki and Kd values (PID values)
Ku = 3;
Tu = 7.486;
fprintf('Ultimate Gain (Ku)\n <<< Ku = %.5f >>>\n', Ku);
fprintf('Oscillation Period (Tu)\n <<< Tu = %.5f >>>\n', Tu);

% Proportional Control
P = 0.5*Ku;
fprintf('Proportional Control (P)\n::: P = %.5f\n', P);
% Proportional-Integral Control
P = 0.45*Ku;
I = (0.54*Ku)/Tu;
fprintf('Proportional-Integral Control (PI)\n::: P = %.5f  I = %.5f\n', P,
I);
% Proportional-Derivative Control
P = 0.8*Ku;
D = 0.10*Ku*Tu;
fprintf('Proportional-Derivative Control (PD)\n::: P = %.5f  D = %.5f\n', P,
D);
% Classic PID Control
P = 0.60*Ku;
I = (1.20*Ku)/Tu;
D = 0.075*Ku*Tu;
fprintf('Classic PID Control\n::: P = %.5f  I = %.5f  D = %.5f\n', P, I, D);
% Pessen Integral Rule Control
P = 0.70*Ku;
I = (1.75*Ku)/Tu;
D = 0.105*Ku*Tu;
fprintf('Pessen Integral Rule Control\n::: P = %.5f  I = %.5f  D = %.5f\n',
P, I, D);
% Some Overshoot PID Control
P = (1/3)*Ku;
I = ((2/3)*Ku)/Tu;
D = (1/9)*Ku*Tu;
fprintf('Some Overshoot PID Control\n::: P = %.5f  I = %.5f  D = %.5f\n', P,
I, D);

% No Overshoot PID Control
P = 0.20*Ku;
I = (0.40*Ku)/Tu;
D = (2/30)*Ku*Tu;
fprintf('No Overshoot PID Control\n::: P = %.5f  I = %.5f  D = %.5f\n', P, I,
D);

% Rule of Thumb PID Control
P = 2*Ku;
I = 1.5*Tu;
D = I/5;
fprintf('Rule of Thumb PID Control\n::: P = %.5f  I = %.5f  D = %.5f\n', P,
I, D);
```

Appendix D: MATLAB Code: InputDependentGain.m

```
function [k] = InputDependentGain(u_in)
%INPUT DEPENDENT GAIN Summary of this function goes here
%   This is the Matlab approach workaround to the input dependent gain
%   problem.
%   Takes in input value, generates a new gain value so that Simulink
%   can complete the transfer function.

%{
% This is the old version using a power function.
% Previously time constant was 65.273s
a = -461;
b = -0.02596;
c = 517;
if u_in <= 0.013
    T = ((u_in).*0)+1;
else
    T = a.*((u_in).^b)+c;
end
%}
p1 = 20.49;
p2 = -53.05;
k = p1.*u_in + p2;
end
```